The Catalytic and Mechanical Properties of Lithium Battery Electrodes

Thesis by

Chen Xu

In Partial Fulfillment of the Requirements for the degree of

Doctor of Philosophy

CALIFORNIA INSTITUTE OF TECHNOLOGY

Pasadena, California

2017

(Defended August 16, 2016)

Chen Xu
ORCID: 0000-0002-9427-0161

PUBLISHED CONTENT AND CONTRIBUTIONS

Chen Xu, Betar M. Gallant, Philip U. Wunderlich, T. Lohmann, and J.R. Greer. *Three-Dimensional Au Microlattices as Positive Electrodes for Li–O2 Batteries*. ACS Nano 9(6), 5876-5883 (2015)

doi: 10.1021/acsnano.5b00443

C.X. participated in the conception of the project, design of the experiments, and assembly of the cells. C.X. conducted spectroscopic and microscopic experiments, analyzed the data, and participated in the writing of the manuscript.

Chen Xu, Zeeshan Ahmad, Venkatasubramanian Viswanathan, Asghar Aryanfar and Julia R. Greer. *The Enhanced Strength and Temperature Dependence of Li at Small Length Scales and its Implications for Li Metal Anodes.* (arXiv ID 1606.05826, under review)

C.X. participated in the conception of the project, and design of the experiments. C.X. fabricated the micro-mechanical testing samples, conducted mechanical characterizations, analyzed the data, and participated in writing the manuscript.

Chen Xu, Jingwei Shi, Junyu Yang and Julia R. Greer. *A 3-Dimensional Microlattice Electrode with Perovskite Catalysts as the Positive Electrode for Li-O_2 Batteries*. (In preparation)

C.X. participated in the conception of the project, design of the experiments, and the fabrication of the electrodes. C.X. assembled the cells, conducted battery performance, spectroscopic and microscopic characterization, analyzed the data, and participated in writing the manuscript.

Acknowledgement

First and foremost, I would like to thank my advisor Julia R. Greer. Through her mentorship I learned how to be an independent researcher, and the importance of self-motivation and optimism when met with obstacles. Through her support, I've had opportunities to do interesting science, to interact and collaborate with people from different institutes, and to go to numerous conferences and present our work. Through theses experiences I have learned the importance of communicating effectively and to how present in a scholarly manner.

I would like to thank Dr, Timm Lohmann and Dr. Jake Christensen for being my mentors at Bosch Research and Technology Center, Palo Alto. I would like to thank Philip Wunderlich for being a great collaborator, and putting up with me at times. I would also like to thank Dr. Sondra Hellstrom for many useful discussions, and providing guidance for building an oxygen delivery system.

I an indebted to Prof. Betar M. Gallant for providing much valuable guidance in my first project, imparting what I can only describe as "wisdom" in the Li-air field. I am extremely grateful to Prof. George Rossman, for allowing me free access to the FTIR and Raman equipment, without which 2 out of my 3 projects would not have been possible. I would also like to thank Dr. Chi Ma for EBSD assistance and many useful discussions; our training sessions have always been productive and enjoyable.

I would like to thank Prof. Venkatasubramanian Viswanathan and Zeeshan Ahmad for being great collaborators, providing us with theoretical calculations, the numerous correspondences, and the writing of our paper. I would to thank Dr. Asghar Aryanfar for many useful discussions, and allowing me access to various equipment in the Hoffmann lab. I would also like to thank Jingwei Shi for being a great collaborator/mentee, with whom I have had immense pleasure working with.

I would like to extend my sincere gratitude to Prof. Brent Fultz, for being a wonderful option representative and a source of support throughout my time at Caltech. I would like to thank all of my lab mates for making my time at Caltech extremely enjoyable. I'd like to especially thank Ottman and Alessandro for helping out with things, when I needed something "quick and dirty", or trying a particular technique that I am not trained in.

And finally, my family. My gratitude goes to my father Dr. Furong Xu, who has been my greatest inspiration since as far as I can remember, dating back to those hot summer nights in Beijing when you explained black holes and special relativity. Also to my mother Hong Hao, a pillar of support throughout my life and my council when I needed it the most. And last but not least, my sincerest gratitude towards Wen Zhou, my girlfriend of 10 years, for being the joy of my life and sticking by me through thick and thin.

Abstract

The mass adoption of electric vehicles warrants higher energy densities at lower costs. Novel chemistries such as Li-S or Li-air, high energy density anodes such as lithium (Li) metal are some of the ways to address the aforementioned issue. However, many scientific challenges must be overcome in order to achieve the successful commercialization of these batteries. For Li-air, poor cyclability and low coulumbic efficiency are key obstacles. The search for cathode materials that exhibit high capacity, low discharge/charge overpotential and chemical stability over many cycles is a major area of interest in the field. On the anode side, the application of Li metal is stumped by uncontrollable dendrite growth during the charging, and existing methods such as pulsed charging, physical suppression, and additives in the electrolyte have only had alleviating effects.

The first part of this thesis investigates the suitability of various materials as Li-air cathodes. We fabricated 3-dimensional architected electrodes using a variety of materials including Au, Ni, Ti, $LaCoO_3$ (LCO), $LaNiO_3$ (LNO), and $LaNi_{0.5}Co_{0.5}O_3$ (LNCO). Their performances in capacity, overpotential, and cyclability were assessed using galvanostatic battery testing methods. The reaction products were investigated using spectroscopic techniques such as FTIR and Raman. Our experiments corroborated recent findings that even trace moisture contamination can dramatically influence discharge product composition and morphology. Furthermore, Ni nanoparticles may serve as a carbon substitute in investigating the properties of non-conductive catalysts under specific potential windows. By incorporation the perovskites into a Ni based conductive mesh, we found the oxygen reduction reaction capability of the three materials to be ranked as LCO>LNCO>LNO, and the chemical stability ranked as LCO>LNO>LNCO. The instability of DMSO due to chemical reactions with discharge products is observed and discussed in the context of the solution-mediated mechanism of Li_2O_2 growth. The second part of the thesis investigates the nano-mechanical properties of Li (bcc), as a function of size, temperature, and crystal grain orientation. At room temperature the power law exponent of the strength vs. size log-log plot is -0.68, while at 90°C this value is increased to -1.00. A factor of 3 decrease in the yield strength at 90°C is observed, and the

morphology of deformation was found to transition from localized slip planes to homogeneous barreling. Our collaborators at Carnegie Mellon University calculated the elastic constants of Li from 78 K to 440 K (melting temperature of Li is 453 K), and is found to be within reasonable agreement with existing experimental data where applicable (78 -300 K). We proceeded to calculate the elastic and shear moduli of single crystal Li as a function of temperature and orientation. We found that due to the extreme anisotropy of Li, there is a factor of ~4 difference between the strongest and weakest orientation of both the elastic and shear moduli. Our findings are discussed in the context of Li anodes, where we highlight the importance of taking into consideration the size-effect and anisotropy when designing solid electrolytes, or modeling dendrite growth behavior.

Table of Contents

List of Figures

Chapter 1

Introduction

The detrimental environmental impact of fossil fuel consumption, coupled with its depletion as a natural resource, has spurred the research of clean energy storage for the many decades. While alternative power generation sources such as wind, solar, geothermal, or nuclear may prove effective as large grid-scale power supplies, their portability proves troublesome for applications requiring compactness and mobility, specifically, transportation. Currently, 26% of fossil fuel usage in the US is directly related to transportation.[1] Electric Vehicles (EV) are the most promising clean alternative to traditional gasoline-fueled cars. Lithium-ion batteries have found commercial success in a wide-range of mobile electronic devices such as phones, laptops, and remote sensors. However, the current state-of-the-art Li-ion battery has far less practical specific energy (200 Wh kg^{-1}) than gasoline (1700 Wh kg^{-1}), [2,3] causing most EV's driving range per charge (100 miles)[4] to fall far shorter than those of gasoline cars (380 miles per refill).[3] That and the high cost of battery manufacturing have prevented the mass adoption of EVs. The aforementioned 100-mile per charge is based on assuming a 200 kg battery pack as the main power supply within the EV. Increasing the battery pack size, along with developing advanced battery management systems, will increase the driving range of EVs, as demonstrated by the Tesla model S (540 kg battery pack, 265 miles per charge).[5] However, the high cost of the batteries, mostly arising from raw materials, makes current EV prohibitively expensive for mass

adoption. The need for higher energy density at decreased cost has driven researchers to investigate alternative chemistries in the secondary battery domain.

1.1 Lithium-ion Batteries

Li-ion cells typically consist of three components: a positive electrode, a separator, and a negative electrode. The positive electrode is typically made of a transition metal oxide, e.g. $LiCoO_2$, or phosphate, e.g. $LiFePO_4$. The negative electrode is most commonly made of graphite (C_6). The separator in between is imbued with an organic electrolyte such as lithium hexafluorophosphate ($LiPF_6$) in ethylene carbonate (EC). During discharge, the positive electrode is reduced, and Li^+ ions leave the negative electrode, traverse the separator, and insert themselves into the positive electrode via a process known as intercalation. Electrons travel through the external circuit, powering devices. The charging process is the reverse of the aforementioned procedure, where Li^+ ions travel in the opposite direction and intercalate into the graphite layers. The voltage of a cell is determined by the difference between the insertion/removal potential of the positive and negative electrode. This value is usually between 3 – 4.2V vs. Li/Li^+ for the positive electrode, and 0 – 1.5 V vs. Li/Li^+ for the negative electrode.[6] The energy density of the cell is correlated to the theoretical energy density of the two electrode materials. Typical values are given in Figure 1. We see that in Li-ion cells, the energy density of the positive electrode (100 – 300 Ah kg^{-1}) is usually lower than that of the negative electrode (300 – 1000 Ah kg^{-1}), and is therefore the limiting factor of the overall energy density. Packaging further reduces the energy density of the cell. The energy density of an electrode material is strongly correlated to the atomic ratio

between Li and the intercalation compound at the fully lithiated state; the high molecular weight of the transition metal oxide or phosphates is the reason why the positive electrode has a low energy density. That is why Li metal is considered the "holy grail" for negative electrodes (3860 Ah kg^{-1}),[7] as it carries no extra weight due to the intercalation compound. Li metal is currently not considered a feasible anode material due to many challenges, as will be described in detail later on.

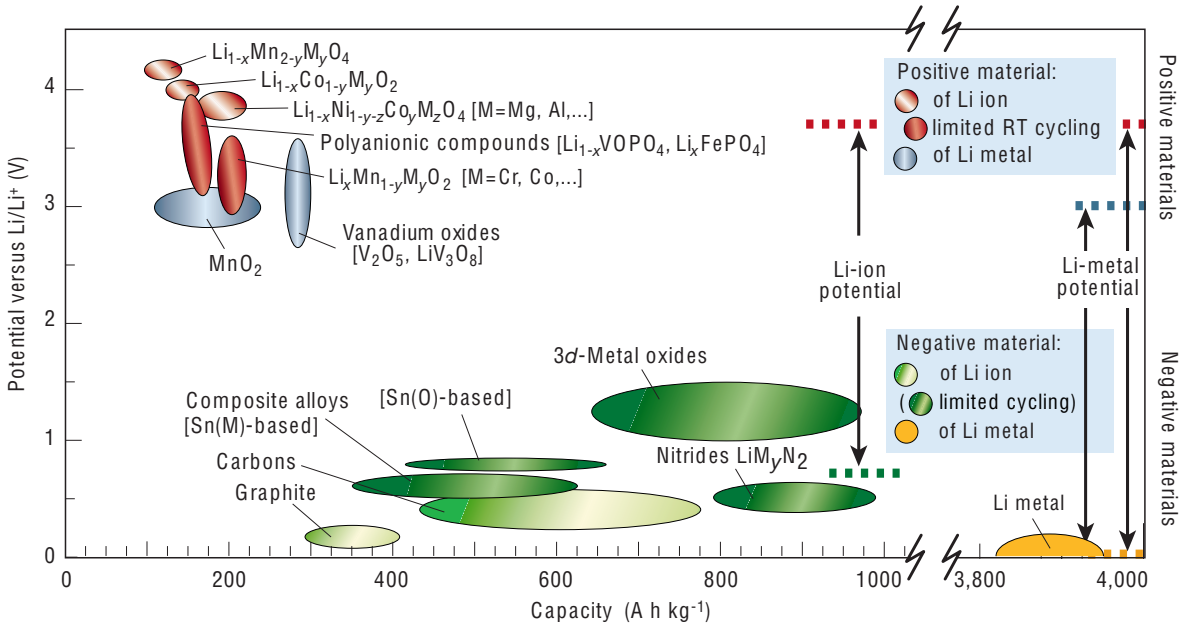

Figure 1. Voltage vs. Capacity of electrode materials in Li-ion batteries. Reproduced from J.-M. Tarascon & M. Armand, *Nature* **414**, 359-367 (2001)

1.2 Li –O_2 Batteries

1.2.1 Motivation for Developing Li-O_2 Technology

In order to tackle the challenges facing current Li-ion batteries, alternative battery chemistries such as Li-S and Li-O_2 are being pursued.[4] Li-S has been investigated since the 1940s but many challenges remain.[4] Li-O_2 is a much younger technology first demonstrated in 1996 by Abraham et al.,[8] and which saw many advances in the past decade.[9–13] Li-O_2 batteries have received considerable attention due to their high energy density. The high energy density is due to the omission of the heavy intercalation positive electrode material, as well as the fact that the discharge product, Li_2O_2, is formed with two electrons/Li^+, compared to only one in $LiCoO_2$ or $LiFePO_4$. An often quoted high energy density value of 11,586 Wh kg^{-1} is based on the mass of a Li anode alone; the value becomes 3505 Wh kg^{-1} when the weight of O_2 is considered.[4] Further considering cell packaging and other factors that may reduce energy density, a rough estimate for a commercial Li-O_2 cell may have an energy density of 500 -900 Wh kg^{-1},[4] which is still 2 -3 times greater than the current Li-ion technology and may deliver an EV that exceeds the driving range of 340 miles using only a 200 kg battery pack.[3,4] While inspirational, we note that this estimate makes a major assumption that the required O_2 can be obtained from the atmosphere. This requires a membrane that has an extremely low permeability towards all contents of the atmosphere except O_2, which is a huge technological challenge in itself.

The Li-O_2 cell typically contains a negative electrode (commonly Li metal, but can be graphite), an organic electrolyte, and a porous positive electrode connected to an O_2 source. During discharge, the Li^+ ion reaches the positive electrode and reacts with O_2 to form

Li_2O_2 on the surface of the porous positive electrode. The consensus on the mechanism of the O_2 reduction on discharge is[4]:

$$O_2 + e^- \rightarrow O_2^- \quad (1)$$

$$O_2^- + Li^+ \rightarrow LiO_2 \quad (2)$$

$$2LiO_2 \rightarrow Li_2O_2 + O_2 \quad (3)$$

As one can see the positive electrode does not actively participate in any reactions, and merely serves as a conductive medium for electrons and reaction sites on which the discharge product grows. In most studies ultrapure O_2 is often externally supplied, although the ultimate goal towards commercialization is for the cells to extract O_2 from the atmosphere, hence the other common name of the technology, "Li-Air" batteries.

1.2.2 Electrolyte Instability

In order to offer rechargeability to batteries, the electrolyte must be able to sustain reversible chemistry. In the context of Li-O_2 batteries, the electrolyte must be stable in the presence of O_2, its reduced species, and the discharge products (LiO_2 and Li_2O_2). In order to offer high power density to batteries, in other words the ability to be discharged at high current rates, the electrolyte must exhibit sufficient Li^+ conductivity and O_2 solubility.[4] Organic carbonate electrolytes have been widely used up to around 2011, due to their widespread use in Li-ion applications; however studies has since then shown that there is little to no formation of Li_2O_2 even during the first discharge in these cells.[14–17] A key tool for investigating the discharge products is Fourier transform infrared (FTIR) analysis,

where Mizuno et al. first showed that Li_2CO_3 and lithium alkyl carbonates were the main discharge products of a cell incorporating carbonate based electrolytes.[14] Freunberger et al. used FTIR to identify the reaction products to be Li_2CO_3, HCO_2Li, CH_3CO_2Li and $C_3H_6(OCO_2Li)_2$, while mass spectroscopy (MS) on the evolved gases during charging showed formation of CO_2 and H_2O.[17]

Ethers are now commonly used as electrolytes since the instability of carbonate electrolyte has been established.[2,10,18–21] Specifically, dimethoxyethane (DME) was shown to mainly produce Li_2O_2 upon the first discharge, as confirmed by Raman Spectroscopy and a 2.05 e^-/O_2 ratio on discharge by differential electron mass spectroscopy (DEMS). DEMS identify and also quantify the gas consumed during battery operation, relating the value to the number of charge passed. Combining the reaction Eq. (1-3), we see that two electrons are involved for every O_2 that is reduced, and therefore the ideal e^-/O_2 would be 2. Other ethers such as tetraethyleneglycoldimethyl ether (TEGDME) have also been found to produce primarily Li_2O_2 during the first discharge. However ethers have been found to be less stable during the charging process, as large deviations from the 2 e^-/O_2 ratio is observed at charging potentials of >4.1V is observed in cells with DME.[22] Side reaction products may be oxidized during charging in the first few cycles, leaving the surface of the electrode devoid of detectable discharge products; however as the cycle numbers increase they quickly accumulate and becomes less easy to oxidize, and thus can be detected by FTIR after charging.[19] The accumulated insulating side reaction products passivates the surface of the electrode, preventing further O_2 reduction in subsequent cycles, causing the capacity to fade dramatically.

Dimethyl sulfoxide (DMSO) has garnered much attention recently due to promising results showing high capacities and enhanced stabilities of up to 100s of reversible cycles.[9,10] However recent studies have called into question the stability of DMSO in the presence of Li_2O_2, where a time-dependent chemical process is observed to gradually convert Li_2O_2 into LiOH and form dimethyl sulfone ($DMSO_2$) over time.[23,24] Other classes of electrolyte solvent such as nitriles,[25,26] amides,[27,28] ionic liquids,[29,30] and even molten salt[13] have been investigated, with no conclusive data indicating a stable electrolyte that meets the requirement for prolonged Li-O_2 battery cycling.

1.2.3 Positive Electrode Instability

The capacity fade of batteries over cycling stems from not only the degradation of the electrolyte, but of the positive electrode too. The most common positive electrode material is carbon (C). Depending on the process, high surface area carbon (50 $m^2 g^{-1}$ to 3000 $m^2 g^{-1}$) can be manufactured. The ease of manufacturing, combined with low cost and density, makes it extremely suitable for the investigation of fundamental mechanisms as well as demonstration of the high specific capacity expected in Li-O_2 cells. 1st discharge capacities are usually in the range of 1000s of mAh g^{-1} at rates of 100s mA g^{-1}.[21,31,32] Large capacities of up to 15000 mAh g^{-1} have been demonstrated with a graphene electrode.[33] Based on these promising results, catalysts were further introduced into the carbon-based electrodes to enhance oxygen reduction reaction (ORR) and oxygen evolution reaction (OER). Noble metals[32,34–36] and metal oxides[37–39] have been shown to enhance the ORR and OER properties of the original carbon electrode. However, C is found to be unstable in the

extremely oxidizing environment of Li-O_2 systems. Specifically, the C surface reacts with Li_2O_2 to form Li_2CO_3.[40–42] C is found to be unstable above a charging potential of as low as 3.5 V (in the presence of Li_2O_2) in DMSO and TEGDME electrolytes;[42] oxidation of Li_2CO_3 on charging to ~ 4 V is incomplete,[42] which leads to Li_2CO_3 accumulation that decreases the exchange current density at the C- Li_2O_2 by 10 -100 fold,[40] and prevents further ORR in subsequent cycles.

Many groups have since moved towards carbon-free electrodes, with candidates such as nanoporous Au (NPG),[9] TiC,[10] Co_3O_4 on Ni,[43] Ru on Ni,[44] $NiCo_2O_4$ on Ni,[45] and Au on Ni.[46] Various degrees of enhanced oxidation resistance is observed, most notably in NPG[9] and TiC.[10] However, new issues arise, such as the higher density of the materials leading to a lower gravimetric specific capacity, e.g. NPG has a capacity of only 300 mAh g^{-1} at a current density of 500 mA g^{-1}.[9] The low conductivity of the metal oxides requires a conductive framework, which in many cases is Ni. The stability of Ni is debated.[47,48] And finally, the cost of the material as well as the complexity of fabricating surface area electrodes is much higher than the C. However, these issues, with maybe the exception of possible instabilities arising from a Ni framework, are secondary compared to the promise of better stability comparing to C. As previously mentioned, irreversibility remain the main challenge to the advancement of Li-O_2 as a technology, and existing studies already indicate an inevitable move away from C based electrodes.

1.2.4 The Impact of Moisture, and the Formation Mechanism of Li_2O_2

There is a need to highlight a recent advancement in the fundamental understanding of how Li_2O_2 is formed. This advancement is achieved by the independent work of many groups, and partially inspired by investigations on the influence of trace moisture in Li-O_2 cells. Moisture may arise from trace water in the electrolyte solvent (Anhydrous grade is defined as H_2O < 30ppm by Sigma Aldrich), insufficient drying of cell parts or electrode material before cell assembly, air contamination in the oxygen delivery pipeline (reason why many groups use ultrapure stainless steel pipes), and leakage of the cell. In 2012, Meini et al. investigated the influence of water content in the electrolyte on the performance of Li-O_2 cells.[49] Water content of <4 ppm to 1000 ppm was investigated, as well as the behavior of an intentionally "leaky" cell. The "leaky" cell exhibited a 10-fold increase in capacity compared to airtight cells discharged at the same condition (2200 mAh $g^{-1}_{carbon,leaky}$ vs. 200 mAh $g^{-1}_{carbon,aritight}$), using DME as the electrolyte solvent. The water concentration was reported to be 1.6 vol % by the authors at the time of testing. Incidentally, the 2200 mAh $g^{-1}_{carbon,leaky}$ value is comparable to the value 2800 mAh g^{-1}_{carbon} from a "water vapor" cell, where ultrapure dry O_2 was connected to a liquid water reservoir before been pumped into the cell. The discharge plateau in the water vapor cell also exhibited a 50 mV higher discharge plateau than an airtight cell, at 2.71 V. This effect was proposed as being related to the irreversible reaction of LiOH formation, which happens at an elevated potential of 3.35 V versus 2.96 V in Li_2O_2 formation:

$$4Li + 2H_2O + O_2 \rightarrow 4LiOH, \qquad E_{OCV} = 3.35V \tag{4}$$

Cho et al. further investigated the effect of atmospheric water contamination in 2014, where 6 cells were connected in sequence by a silicone tube, and shared a common oxygen source.[50] The effect of moisture contamination was shown to increase from the cell closest to the oxygen source (and therefore was supplied the driest oxygen) to the cell farthest from the source (subject to the most atmospheric contamination from the pipelines). A 139% increase in discharge capacity was observed.[50]

Aetukuri et al. further investigated the moisture vs. capacity relation, exposing the role that moisture plays in determining the Li_2O_2 morphology.[12] A report of a wide range of Li_2O_2 morphology exists in literature, ranging from toroidal shaped,[31,51–55] small particles,[41,56] and platelets,[57,58] to thin films.[59] The formation of toroids usually leads to large capacities, as these relatively large structures allow for more discharge product per surface area. Many works prior to 2014 have shown that the morphology depends mainly on discharge rate, where slow discharges, e.g. 10mA g^{-1}_{carbon}, often lead to toroidal discharge products with diameters of hundreds of nm.[52,53] As the rate is increased, the size of the toroid decrease, as does the crystallinity, until it becomes an amorphous thin film of below 10nm in thickness.[59] However Aetukuri et al. showed that in ether electrolytes (such as DME), having a H_2O content of above below 30 ppm will not allow for toroid formation, no matter how low the current; as the water content is increased, from the nominal anhydrous (30 ppm) to 4000 ppm, the size of the toroids increases under the same discharge rate, as does the crystallinity of the discharge product as identified by X-ray Diffraction (XRD).[12] The

discharge capacity of the cells is found to be strongly correlated to the toroid size. Interestingly, while the direct reaction product between Li_2O_2 and H_2O is LiOH, no LiOH was found by XRD, Raman, or FTIR in the study. Through a combination of DEMS, Linear Scanning Voltammetry (LSV) and chemical titration, the authors proposed a solution-mediated process where partially solvated intermediate discharge products (LiO_2) redeposit onto a growing particle, leaving the original electrode surface free to form more LiO_2. Finally, the LiO_2 disproportionate to form Li_2O_2. A reproduced schematic is given in Figure 2.

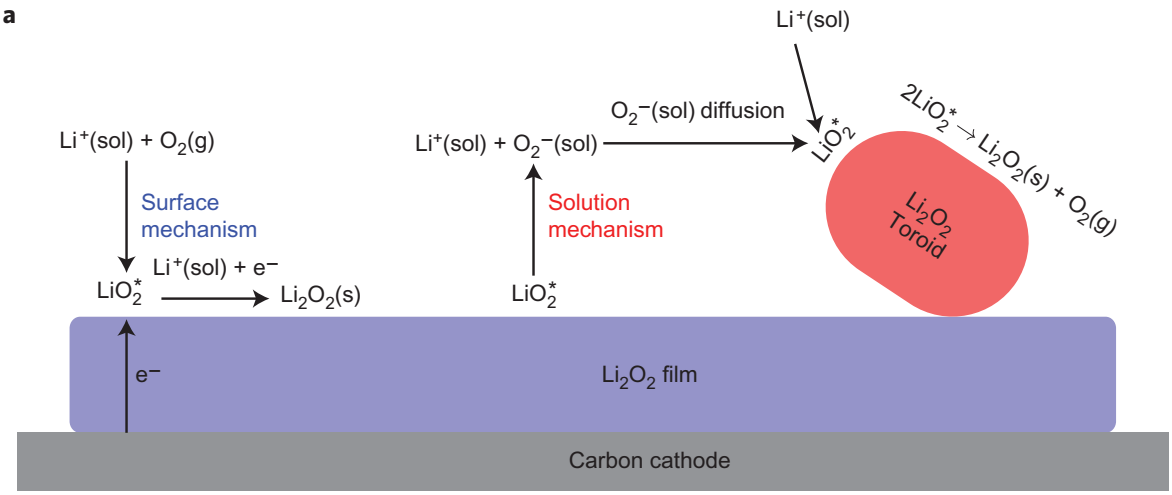

Figure 2. Proposed mechanisms for solution mediated Li_2O_2 growth. Reproduced from Aetukuri, N. B. *et al.* Solvating additives drive solution-mediated electrochemistry and enhance toroid growth in non-aqueous Li–O_2 batteries. *Nat. Chem.* **7,** 50–56 (2014).

The stability of the Li^+ and O_2^- ions in solution is dependent on the Gutman donor number (DN) and acceptor number (AN), respectively. The higher the numbers, the more LiO_2 are dissolved in solution. H_2O has an AN of ~55, while anhydrous DME has an AN of ~10. Therefore the addition of H_2O greatly enhances the ability of the electrolyte to enhance the solution-mediated growth. While the addtion of H_2O may greatly increase the discharge capacity of the Li-O_2 cell, it inevitably gives rise to many detrimental effects, such as degradation of the Li anode. However utilizing other organic solvents with inherently high DN or AN may prove to be a promising pathway for enhancing the performance of Li-O_2 batteries. Johnson et al. further confirmed the solution-mediated pathway using rotating ring-ring disc electrode (RRDE) and surface-enhanced Raman spectroscopy (SERS) in high DN solvents, e.g. DMSO, while in low DN solvents the surface pathway dominates, e.g. DME.[11]

Chapter 2

The Microlattice Electrode as a Medium for Investigating Cathode Materials

Adapted from:

Xu, C.; Gallant, B. M.; Wunderlich, P. U.; Lohmann, T.; Greer, J. R. *Three-Dimensional Au Microlattices as Positive Electrodes for Li-O_2 Batteries*. *ACS Nano* **2015**, *9*, 5876–5883.

As previously mentioned, material stability is major concern in the long-term cycling performance of Li-O_2 batteries, while the search of materials with high ORR and OER capabilities remain an integral part of the advancement of the technology. High surface area carbon is found to be prone to oxidation at high potential of 3.5 V in the presence of Li_2O_2, leading to severe capacity fading after only a few cycles.[42] The many carbon-free electrodes mentioned in the introduction section show promise, yet it is difficult to compare between different materials due to their drastically different morphology. For example, NPG[9] takes the morphology of a metallic foam with nano-sized pores, while the TiC electrode[10] consists of TiC nanoparticles held together by PTFE binder cast on a stainless steel mesh. The different morphology gives rise to different volumetric specific surface areas, while the different density of the materials contributes to different gravimetric specific surface areas. Most existing studies chose to normalize capacity by weight of the

positive electrode; this is in part due to tradition inherited from the Li-ion community, and also the convenience of weighing material comparing to measuring surface area. However while it is logical to normalize the capacity by weight in the Li-ion field due to the fact that the entire positive electrode is expected to participate in the reaction, this is not true for Li-O_2 chemistry. As the previous chapter described, LiO_2 is always formed at the surface of the electrode regardless of whether it is later solvated back into solution. The bulk of the electrode, i.e. any material that is not in contact with the electrolyte, does not participate in the reaction; Li^+ ions will not diffuse into the electrode material. Therefore the knowledge of the surface area, or more accurately, the electrochemically active surface area (ECSA), is important in decoupling the material contribution versus the surface area contribution of ORR and OER. An electrode made of a relatively weak material for ORR may show large total capacities due to its high surface area; glassy carbon electrodes show an extremely low total capacity despite carbon being a great ORR material. ECSA is surface area that may participate in ORR/OER in a Li-O_2 cell. Currently the most common method of measuring surface area is the Brunauer–Emmett–Teller (BET) method, where the surface area is calculated by fitting N_2 adsorption curves. However gas adsorption is different to electrolyte wetting in many ways. For example, N_2 adsorption is only effective in the 0.3 to 300nm pore size range, with larger pores overlooked.[60] The electrolyte wetting process relies on capillary forces and is expected to be much more effective at covering the surface of a porous material. For example, considering the calculation of the height *h* of a meniscus within a cylindrical tube, we have the equation

$$h = \frac{2\gamma cos\theta}{\rho g r} \quad (5)$$

where γ is the liquid-air surface tension (force/unit length), θ is the contact angle, ρ is the density of liquid, g is local acceleration due to gravity, and r is radius of tube. Intuitively, h and r assumes an inverse relation, while a liquid with a higher value of surface tension has a larger capillary action. For water with a γ value of 73 mN m^{-1} at 20 °C, a 0.4 mm diameter tube will allow a meniscus height of 70 mm.[61] Common electrolyte solvents have comparable surface tension values, such as DMSO (44 mN m^{-1}),[62] DME (25 mN m^{-1}),[63] TEGDME (30 mN m^{-1}),[64] dimethyl acetamide (DMA, 37 mN m^{-1}), etc, and therefore should be able to effectively wet the surface of electrodes with hundred micron pore sizes. For many existing carbon-based electrodes, the BET is reasonably accurate because the main surface area contribution comes from pores within the 0.3 - 300 nm range. However for electrodes with a pore size distribution that mainly falls outside this range, the measured value will be much smaller than the real value. The reason why it may be beneficial for electrodes to have larger pore sizes will be discussed shortly.

The physical inhomogeneity of the positive electrode at the nanoscale may also affect the ECSA value, or the current distribution during discharge/charge. Electrodes consisting of nanoparticles usually require an organic binder to provide mechanical stability to the electrode, as well as provide electrical connectivity; it is plausible that uneven dispersion of the binder may lead to non-ideal electrical connectivity between the particles, leaving certain populations of the particles unable to participate in ORR/OER. Again the surface area contribution by the electrically disconnected particles will still be measured by BET,

which further adds to the overestimation of the surface area by this method. In Li-ion batteries, uneven distribution of discharge or charge current, leading to sequential instead of simultaneous (de)lithiation of particles, are observed in positive electrode materials such as $LiFePO_4$.[65–70] This phenomenon may be detrimental to the long-term health of batteries, since a high concentration of current on individual particles may expedite their degradation. A similar phenomenon in Li-O_2 is "pore-clogging". Higher current density, e.g. closer to the current collector due to higher O_2 concentration and in close proximity to the electron source, may lead to Li_2O_2 growing faster in this region, subsequently clogging up channels that allow the rest of the electrode access to O_2. Again, this leads to underutilization of electrode material, as well as premature termination of discharge, or in the case of build up of irreversible side reaction product, premature cell death. It is often cited as the reason why electrodes with extremely high surface area (therefore small pores, and more susceptible to clogging), e.g. activated carbon (~3000 $m^2\ g^{-1}$), exhibits much lower discharge capacity than Super P (~ 60 $m^2\ g^{-1}$, large pores).[3,71] Studies have shown the growth of >100 nm toroids growing only on the surface of the electrode, on the side facing the O_2 source.[32]

The ideal electrode would be made of a material with favorable ORR/OER properties, taking a morphology that has superb interconnectivity (without the use of binders), and, balances high surface area and large enough pore size to accommodate large discharge products. Micron-scale architected materials, with their precise control over geometry, high surface area, structural robustness, and flexibility of constituent material, show promise in overcoming the aforementioned challenges with traditional electrodes. The nanolattice,

with a minimum unit cell size of ~3 μm, can be made of a variety of materials, ranging from Au to Al_2O_3.[72,73] The nanolattices are fabricated using a 3D printing technique called two-photon lithography, and subsequently coated by a material of choice via sputtering,[72] atomic layer deposition (ALD)[73] or electrodeposition.[74] A detailed description of the fabrication of the naolattices is described elsewhere.[72,73] The coating techniques combined allows us to essentially fabricate the structures out of any material, while keeping the geometry, and therefore the surface area, the same. This will allow us to decouple the geometric and material influence on the battery performance, and focus on each aspect independently. An example of a nanolattice is shown in Figure 3. However due to the current speed limitation of the technique, only small structures with dimensions less than 100 μm can be made. Incorporation of such an electrode into a typical Li-O_2 pouch cell would require overcoming of additional challenges, and lies outside the scope of our interest. Therefore, we have chosen to use a similar system, appropriately called the "microlattice", where the unit cells are 2 orders of magnitude larger. These structures can be fabricated using the same wide range of materials, and may exhibit the same level of mechanical robustness and good electrical conductivity as the nanolattice. The most substantial advantage the microlattice has over the nanolattice is that they are fabricated via a scalable method known as self-propagating waveguide cross-linking, developed by HRL.[75–77] The biggest downside of the microlattice is that due to the large unit cell size, the specific surface area, volumetrically and gravimetrically, is roughly 2 orders of magnitude lower than the nanolattice. Therefore the specific capacity is expected to be decrease accordingly. We fully acknowledge that the microlattice structure is not optimized for

superior battery performance; however it does offer unprecedented advantage in investigating material catalytic properties in the Li-O_2 chemistry.

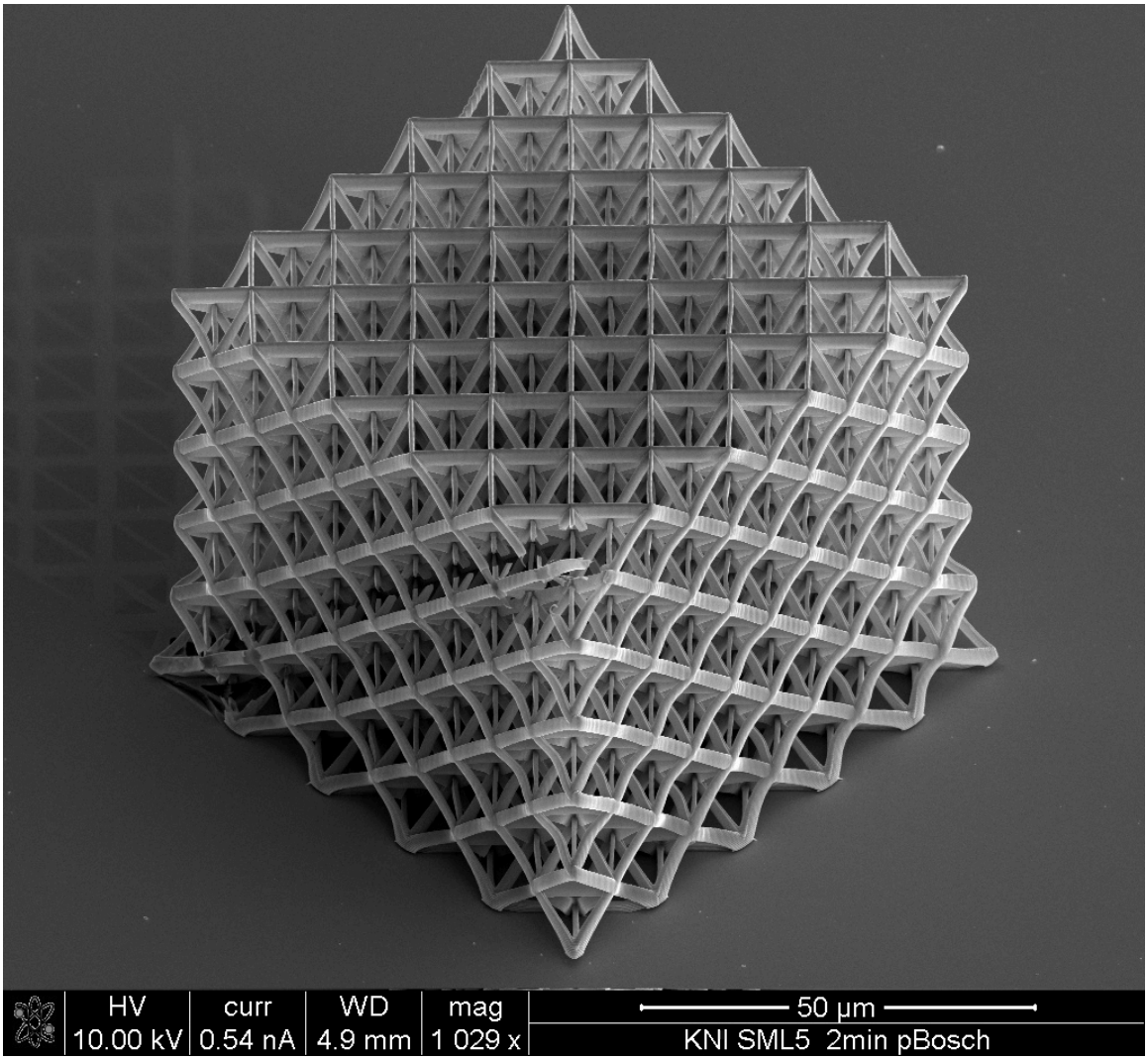

Figure 3. SEM of a polymer nanolattice with octet unit cell. Adapted from http://www.jrgreer.caltech.edu/images /nanotruss_mg_octet_40%20min_003.jpg

2.1 Fabrication of the Hollow Au Microlattice

We chose Au because of its oxidation resistance and demonstrated superior performance in Li-O_2 chemistry.[9] The first step takes place in HRL and is done by our collaborators, where a thiol-ene liquid photomonomer is exposed to collimated ultraviolet (UV) light through a patterned mask, shown in Figure 4. Within the photomonomer, self-propagating photopolymer waveguides originate at each aperture in the direction of the UV collimated beam and polymerize, forming an interconnected solid structure.[75] The octahedral geometry of the unit cell originates directly from this exposure method and is thus intrinsically linked to the fabrication method. The minimum feature size of 100 μm for the diameter of the individual beams is imposed by the UV light diffraction limit within the thiolene based photomonomer.

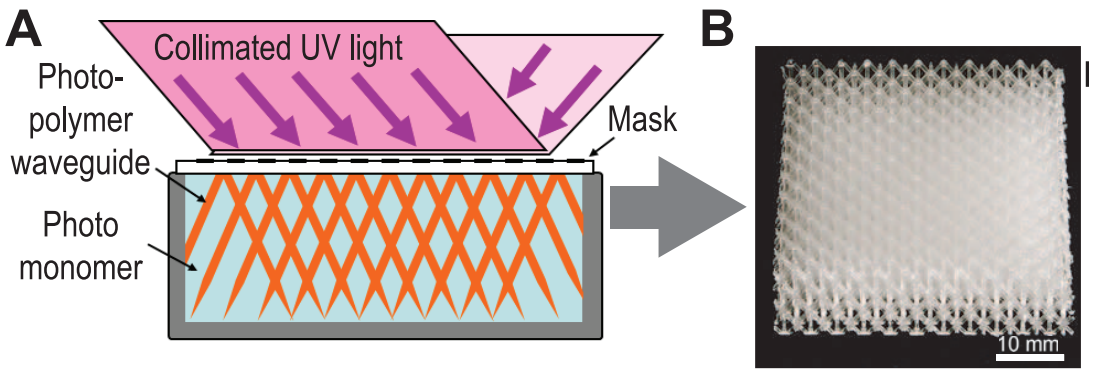

Figure 4. The fabrication of a polymer microlattice, used as a sacrificial scaffold for the eventual hollow, Au microlattice electrode.

The subsequent steps are shown in Figure 5. We sputter 100 nm of Au onto the polymer scaffold as a seed layer for electrodeposition. The sputtering is done under an Ar atmosphere (AJA International ATC Orion sputterer, DC current source, 56 W) with a gas flow rate of 10 sccm, maintaining a working pressure of 3 mTorr. This recipe is used to produce conformal coatings on nanolattices.[72] To ultimately obtain a sufficiently stiff hollow structure that can survive handling and maintain its integrity throughout cell testing, an additional ~5 μm of Au (TSG-250, Transene) was electrodeposited onto the initial 100 nm-thick sputtered layer of Au. The plating temperature was maintained at 60 °C, and the solution was stirred with a magnetic stir bar to maintain optimum flux to the surface. The current density was maintained at ~1mA cm^2. The surface area of the polymer scaffold, which is used to normalize the deposition current, was estimated by modeling the microlattice in computer aided design (CAD) software, with the unit cell dimensions used as input parameters. Following electrodeposition, the coated microlattices were cut into discs roughly 3 mm in height and 17 mm in diameter. The incisions made during this process exposed the polymer within the interior of the truss to the etching solution (1.5MNaOH, in 1:1 v/v methanol and DI water) used to dissolve the polymer. Etching was performed for 24 h at 40 °C,[76] after which the sample was thoroughly cleaned in DI water. The resulting structure, shown in Figure 5.(b-d), is a 3-dimensional octahedral network comprosed of hollow, 5 μm-thick Au tubes. SEM images in Figure 5.(c) reveal that the pore size was roughly 300 μm, the diameter of the individual tubes was 150 μm, and the coating was relatively uniform, with a thickness of 5 μm.

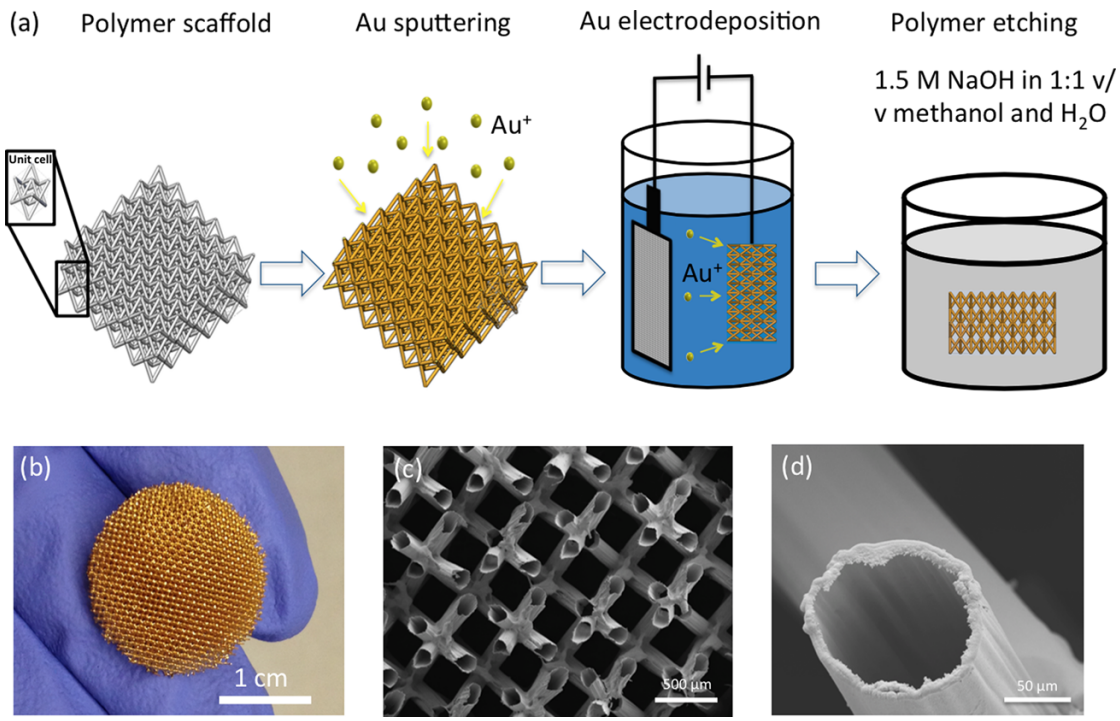

Figure 5. (a) Schematic of the step-by-step fabrication process of hollow Au microlattices. (b) Optical image of Au microlattice cathode, with a diameter of 17mmand a height of 3 mm. (c) A top down SEM image of a Au microlattice, with exposed and hollowed out beams in the field of view. (d) SEM image of an individual beam showing the hollow interior.

2.2 Determination of the ECSA

One of the advantages of the microlattice electrode, compared with traditional carbon nanoparticle electrodes, is the ability to first design the unit cell size, then predict the

surface area, and finally measure the surface area electrochemically. We utilize the reversible redox reaction of the Au surface in acidic solution to measure the ECSA. Microlattice electrodes were tested in a three-electrode beaker cell, with a Ag/AgCl reference electrode and Pt mesh counter electrode. CVs were conducted in the potential range of 0.4 to 1.4 V vs Ag/AgCl in 0.5MH2SO4 at a scan rate of 50mV s^{-1}. The first~15 initial cycles were used to stabilize the CV curves, after which the CV for surface area measurement was performed. A typical voltamogramm is shown in Figure 2.4(a). The anodic peaks at 1.15 and 1.3 V vs Ag/AgCl correspond to the formation of Au surface oxides, and the cathodic peak at 0.9 V arises from corresponding reduction.[78] Using charge integration under the reduction peak while subtracting contributions from double layer capacitance, the total surface area was obtained by dividing the integrated value by the charge per surface area of Au (400 μ C cm^{-2}), as adapted from literature.[78,79] The experimentally measured value of ~140 cm^2 g^{-1} is only 15% higher than that predicted by CAD software. The slightly higher surface area measured electrochemically likely stems from the roughness of the Au surface caused by the polycrystalline microstructure, as well as the initial roughness of the polymer. Figure 6.(b) shows SEM image of the pristine Au microlattice surface with crystallites up to 500 nm.

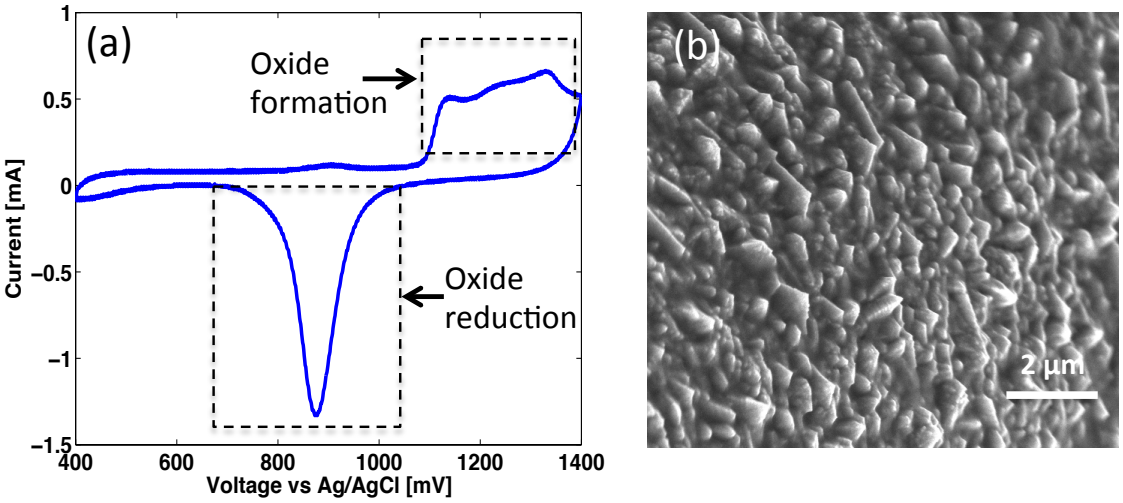

Figure 6. Cyclic voltammogram of as-fabricated Au microlattice and SEM of the surface of the sample. (a) CV of hollow Au microlattice in 0.5 M H_2SO_4 with a scan rate of 50 mV s^{-1}; (b) SEM image of rough polycrystalline Au surface obtained via electroplating.

The XRD spectrum shown in Figure 7. confirms the polycrystalline nature of the deposited gold. Such a low specific surface area of 140 cm^2 g^{-1} arises from the 5 µm-thick Au coating, which is necessary to retain suitable mechanical stiffness and strength.

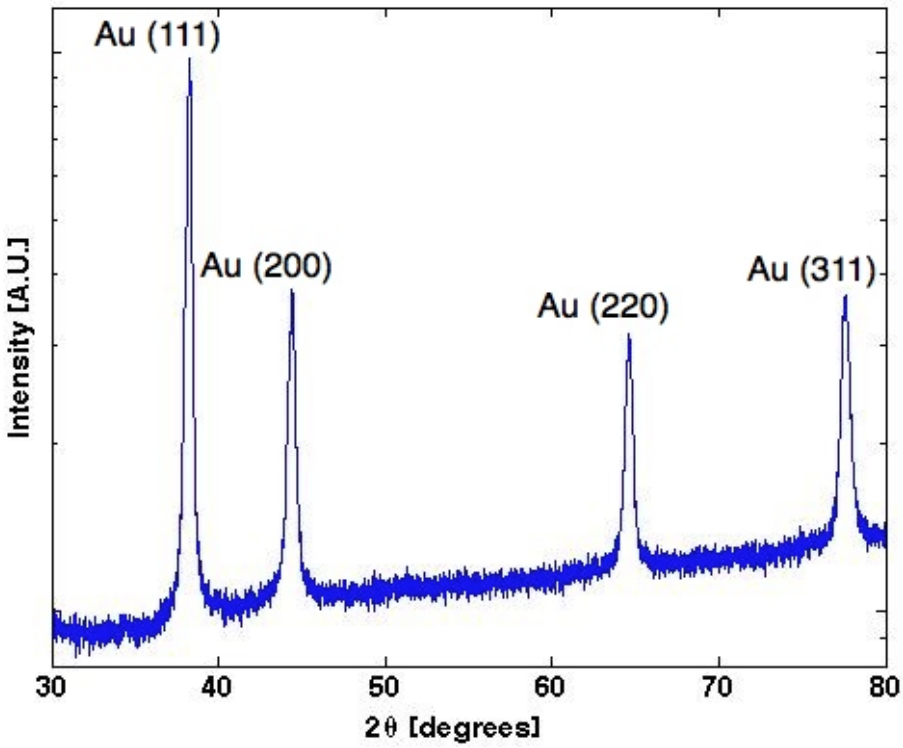

Figure 7. XRD pattern of pristine Au microlattice.

2.3 Cell Assembly and Electrochemical Measurements

Cell assembly and electrochemical testing were partially performed at Bosch Research and Technology Center (RTC) at Palo Alto, CA, and partially performed at Caltech. Electrodes were held at 120 °C under a vacuum for 12 h in an oven/antechamber connected to an Ar glovebox (MBraun, H_2O < 0.1 ppm, O_2 < 0.1 ppm), before being transferred directly into the glovebox without exposure to the ambient atmosphere. The electrochemical cells were commercially available El-cells (EL-CELL GmbH, Germany). Assembled Li_2O_2 cells comprised a Li metal anode, electrolyte- impregnated separator (0.5 M LiTFSI in DME

contained in binder-free borosilicate glass, 260 μm thick), and microlattice cathode. DME (anhydrous, water content 10-30 ppm, Sigma- Aldrich) was dried for several days over freshly activated molecular sieves in the Ar glovebox. After assembly, the sealed cells were transferred out of the glovebox to be connected to an O_2 channel (Teflon) and purged. The gas connection and purging process were carefully controlled to minimize atmospheric contamination by blanketing the cell ports with dry O_2 and maintaining a positive pressure of O2 within the cell during purging, with an ultimate cell pressure maintained at 25 psi. Cells were then subjected to a rest step at open circuit in O_2 for 10 h to stabilize open circuit voltage (OCV) before discharge (the typical OCV was ~3.0 V vs Li). Electrochemical testing was performed using an Arbin BT2000 battery test setup. After testing, cells were opened and dissembled in an Ar glovebox, washed in DME, and vacuum-dried at room temperature for a minimum of 30 min in the antechamber of the glovebox.

2.4 Results and Discussion

The choice of using DME instead of using DMSO was due to the abundance of studies using DME. DME has been shown to give the highest yield of Li_2O_2 (~90%) comparing to a variety of electrolyte solvents, including DMSO (~80%).[22] The galvanostatic discharge behavior of Au microlattices is shown in Figure 8. A discharge voltage plateau is observed at 2.6 V at 0.07 μA $cm^{-2}{}_{true}$, which decreased to 2.5 V as the rate increased to 0.21 μA cm^{-2}

$_{true}$. A sharp decrease in voltage occurs toward the end of the discharge, immediately followed by a more gradual slope until the potential reaches 2 V. Further tests are needed to probe the origin of this sloping profile, which could potentially result from ohmic limitations through the deposited films. In previous reports on nanoporous Au in DMSO, Peng et al.[9] observed a discharge voltage around 2.5 V, with a capacity of 0.6 μAh cm^{-2} $_{ECSA}$ at the discharge rate of 1.0 μA cm^{-2}$_{true}$. The highest rate of 0.21 μA cm^{-2} $_{true}$ used in this work is lower than that reported in Peng et al., and yielded a slightly higher capacity of 1.0 μAh cm^{-2} $_{ECSA}$; the lowest rate of 0.07 μA cm^{-2} $_{true}$ yielded a discharge capacity of 7.0 μAh cm^{-2} $_{true}$. It is important to note that due to the high DN number of DMSO and therefore the propensity to facilitate the solution-mediated growth of Li_2O_2, cells operating with DMSO electrolyte are expected to outperform those with DME in terms of discharge capacity and rate capability. Johnson et al. found a ~5 fold increase in discharge capacity at the same discharge rate on a flat Au electrode, when the electrolyte was switched from DME to DMSO.[11] The fact that we are achieving comparable capacity at comparable rates as the NPG electrode indicates that we are forming a reasonable amount of discharge product per surface area, and that our microlattice electrode, despite the morphological difference to traditional nanoporous electrodes, is behaving as a Li-O_2 cathode should.

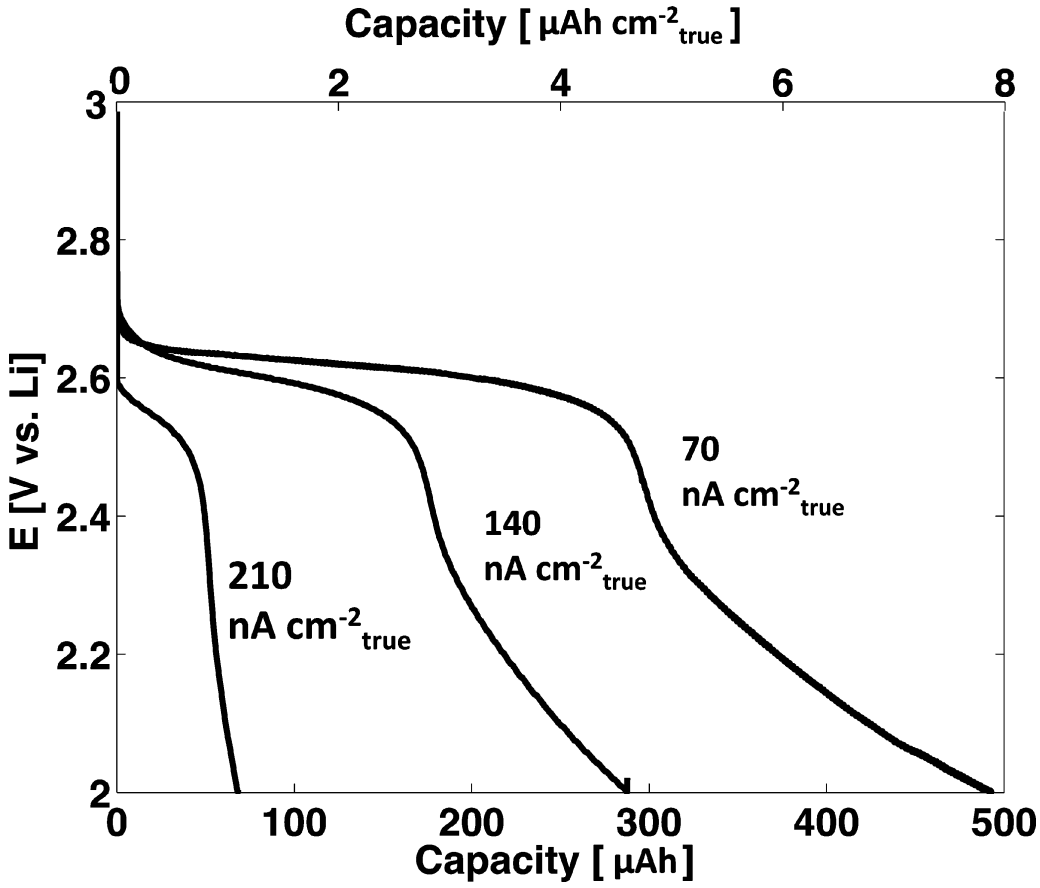

Figure 8. First discharge of Au microlattice positive electrodes over a range of true surface area-normalized currents.

SEM images of the microlattice electrode after first discharge are shown in Figure 9.(a) and reveal that the sample retained its shape integrity during testing, which can be attributed to the favorable mechanical properties of microlattices. Figure 9.(b,c) shows SEM images of the surface of a microlattice discharged at 0.07 µA cm^{-2}_{true}, which is populated with densely spaced toroidal-shaped particles averaging 500 nm in diameter. The size and

morphology of these particles are consistent with the Li_2O_2 particles found on carbon-based cathodes with[32] and without[80,81] catalysts, and on TiC[10] over a range of electrolytes including DME and DMSO. No prior literature has reported the observation of toroidal Li_2O_2 particles on pure Au surfaces with no carbon present. These findings suggest that the electrochemical and chemical processes that lead to the formation of toroids, and their subsequent growth, are not limited to carbon. The electrodes discharged at a higher rate of 0.21 $\mu A\ cm^{-2}_{true}$ (Figure 10.) did not contain toroidal particles, consistent with prior reports on carbon electrodes[52,54,81] in which toroidal particles were observed only at relatively low, near thermodynamic, currents. As mentioned in Chapter 1, trace amounts of H_2O may dramatically influence the morphology of the discharge product. We use anhydrous DME (H_2O<30ppm) dried over molecular sieves for the electrolyte solvent; the glovebox is complete with moisture and O_2 sensor, and keeps the H_2O and O_2 levels below 0.1 ppm. We have thus identified that the most likely source of moisture contamination is the Teflon oxygen delivery line. In subsequent studies, this aspect of our experiment is improved upon by using ultrapure stainless steel gas delivery lines, as will be discussed in the next chapter.

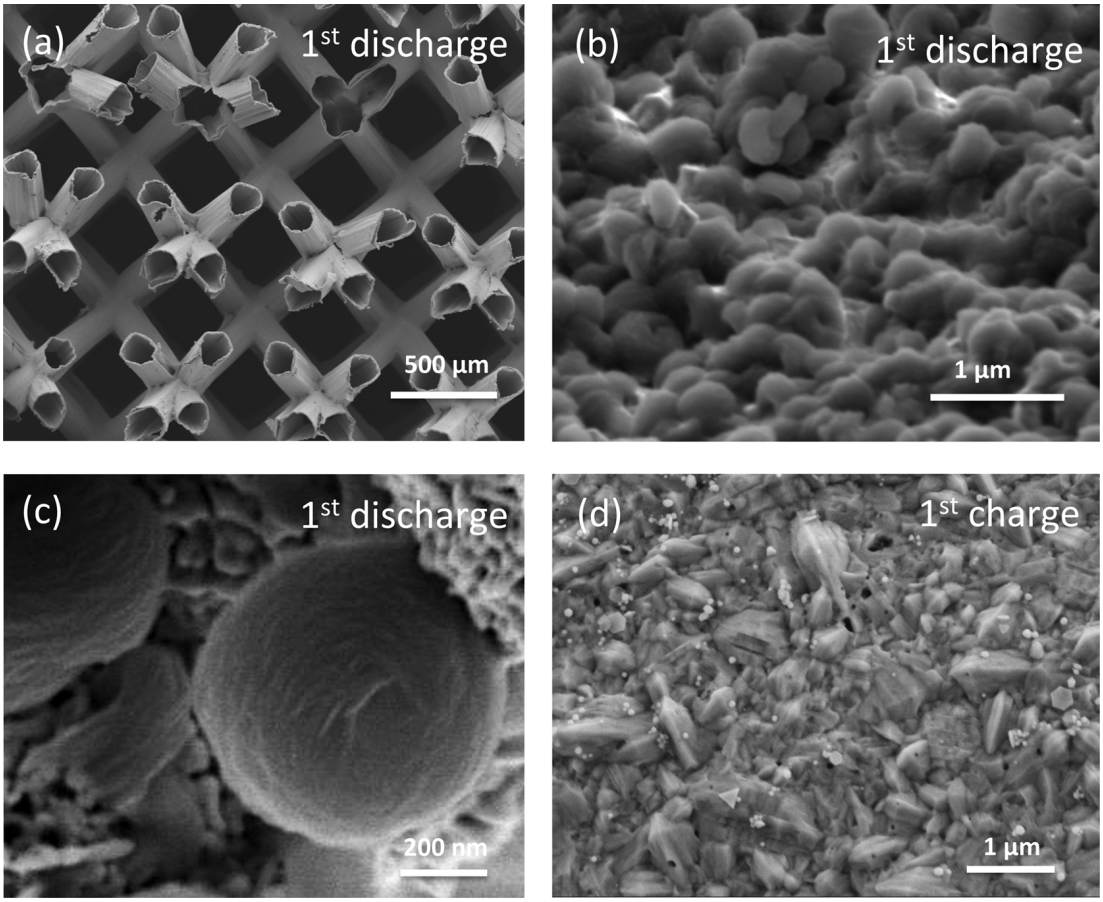

Figure 9. SEM images of (a-c) the surface of a microlattice after the first discharge at 0.07 µA cm^{-2}_{true}, with different magnifications and (d) the surface of a microlattice after the first charge at 0.07 µA cm^{-2}_{true}.

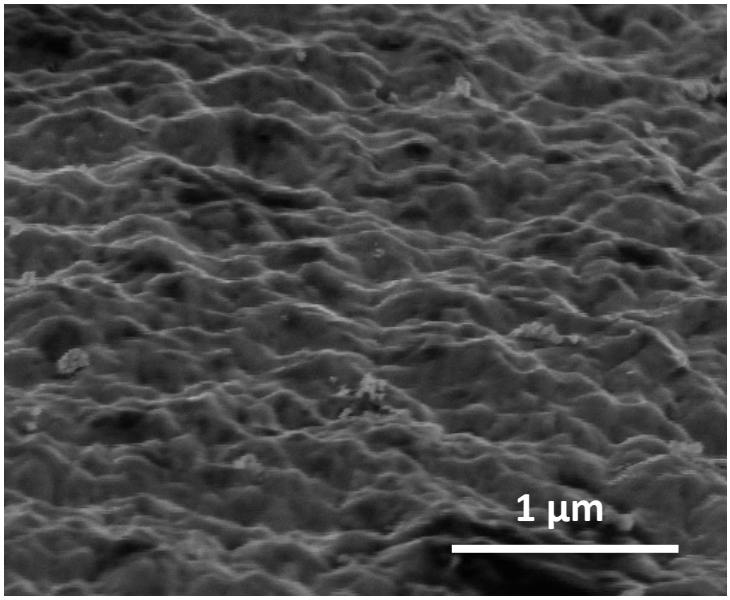

Figure 10. SEM image of the surface of a Au microlattice electrode discharged at 0.21 µA cm^{-2}_{true}. No noticeable formation of "toroids".

Figure 11. (a,b) shows the first galvanostatic cycle at 0.1 µA cm^{-2}_{true} and the first three cycles at 0.14 µA cm^{-2}_{true}, respectively, for two different truss electrodes tested with a lower cutoff voltage of 2 V and an upper cutoff voltage of 4.1 V vs Li. During charging the potential quickly rose to 3.9 V, after which it dropped down to 3.75 V at 40% of the total charge capacity (Figure 11.(a)). The voltage then rose gradually to 4.1 V. Following the first charge, SEM images (Figure 9. (d)) revealed the regeneration of a clean microlattice surface, with the nearly complete removal of toroidal particles. Some particles under 100 nm in diameter, most likely LiTFSI salt, remained whose total amount was insufficient to

generate signals in FTIR or EDS. With cycling, however, both the discharge and charge capacities increased considerably, as shown in Figure 11.(b). For example, the discharge capacities increased with each cycle, from 288 μ Ah in the first cycle to 399 μ Ah in the second and 888 μ Ah in the third, while the discharge potential also rose, from the original 2.60 to 2.75 V during the third discharge. The increase in capacity during cycling was observed previously in studies using ether solvents[82] and glyme solvents.[83] The authors of both studies concluded that the higher measured capacity was a result of solvent oxidation caused by high charging potential; their capacity measured after the first discharge was 3 times higher than that of cells with fresh electrolyte. This may very well be taking place in our cell. However if our hypothesis that moisture contamination also occurs via the oxygen delivery line is also true, then a gradual increase in the solution-mediated Li_2O_2 growth process may also be taking place, effectively increasing the capacity by cycle. The increased discharge potential can be explained by the higher reversible potential for LiOH formation (3.35 V vs. Li).[49]

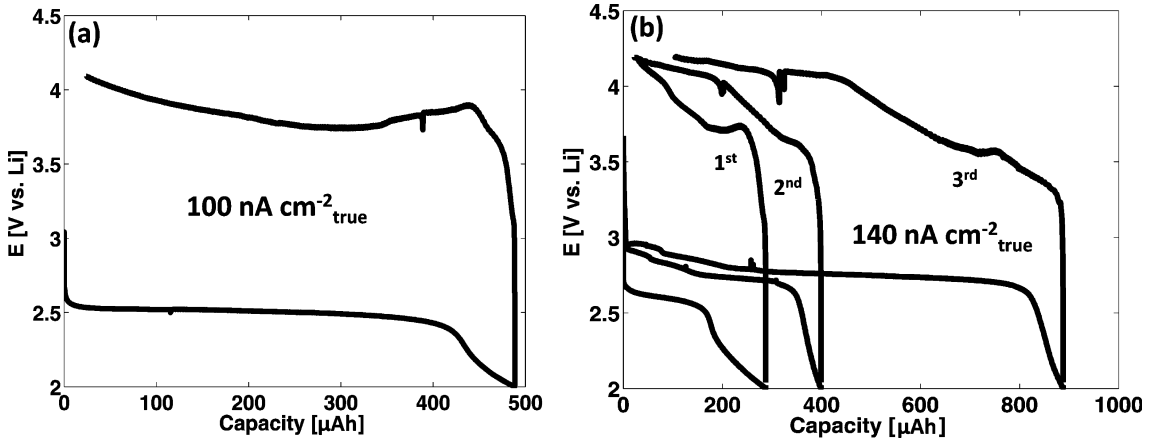

Figure 11. Electrochemical data of (a) first cycle at 0.1 cm^{-2}_{true} and (b) first 3 cycles at 0.14 μA cm^{-2}_{true}.

FTIR spectroscopy were used to investigate the composition of the reaction products and revealed significant chemical changes as a function of cycle number. Figure 12. shows the IR spectra for electrodes after the first discharge and charge, and fourth discharge and charge, along with the powder reference spectra for Li_2CO_3, HCO_2Li, CH_3CO_2Li and LiOH. Li_2O_2 is found to be the predominant discharge product as indicated by the broad peak at 500 cm^{-1}, accompanied by several peaks centered at 1400 and 860 cm^{-1}, which suggests the presence of a small amount of Li_2CO_3. The Raman spectra given in Figure 13. supports this claim, where a peak at 790 cm^{-1} indicates the presence of Li_2O_2; a lack of peak attributed to Li_2CO_3 may be due to the small amount of carbonate present, and also the relative Raman inactivity of the C-O bond. [84,85] The formation of Li_2CO_3 after the first discharge, along with HCO_2Li or CH_3CO_2Li as indicated by the IR peaks at 1600 cm^{-1}, agrees with observations by Peng et al.[9] using DMSO and NPG: peaks associated with

Li_2CO_3, HCO_2Li and CH_3CO_2Li were observed after the first discharge, with their amounts composing less than 1% of the total discharge product. These authors also found that the side reaction products were consistently oxidized during charge, a finding reproduced in this work where the IR data showed no peaks associated with any of the above-mentioned products after the first and fourth charge. We observed substantial accumulation of Li_2CO_3, HCO_2Li, and CH_3CO_2Li after the fourth discharge. This is more apparent in the Raman spectra, with the increase of peak intensity at 1090 cm^{-1}. LiOH was also detected within the electrode after cycling, as indicated by the FTIR peak at 3675 cm^{-1}.

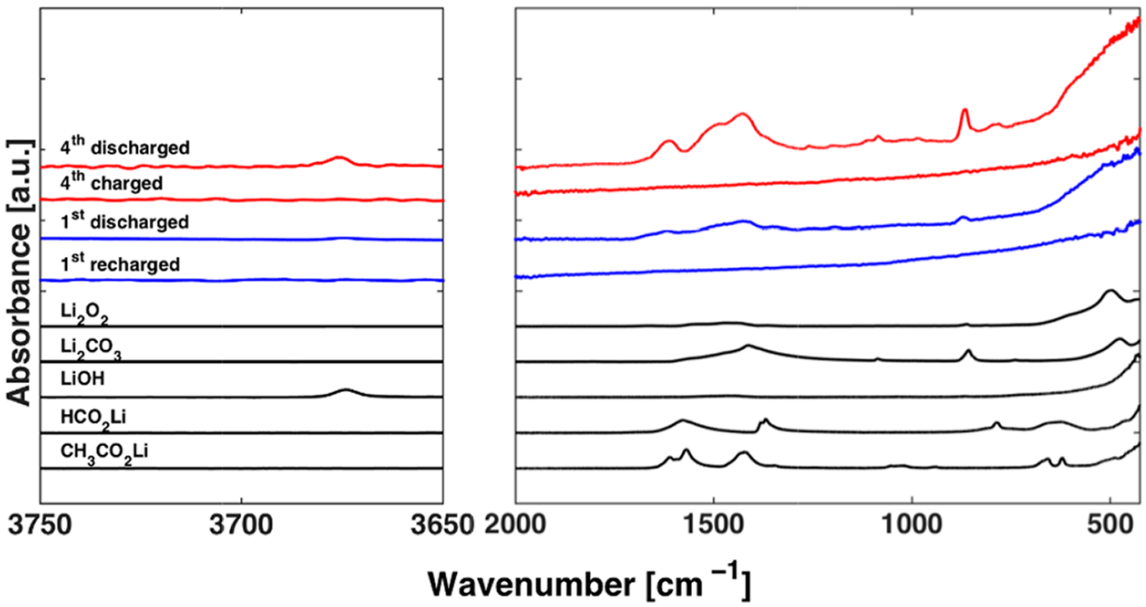

Figure 12. FTIR spectra of discharged, charged, and cycled microlattice electrode.

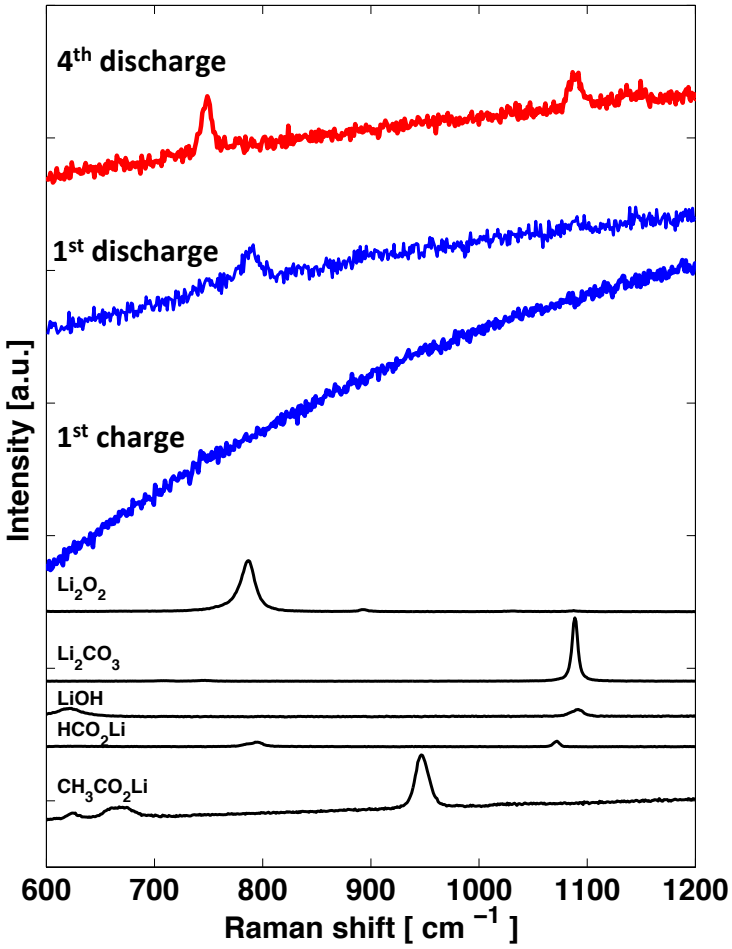

Figure 13. Raman spectra of a microlattices after the 1st charge, 1st discharge, and after 3 cycles ending with a 4th discharge. References obtained from commercially available powders from Sigma Aldrich.

An interesting featured observed in the Raman spectra showed a peak at 750 cm^{-1}, which does not coincide with the previously observed peak for Li_2O_2 at 790 cm^{-1}, nor does it align with expected side reaction products such as LiOH, HCO_2Li and CH_3CO_2Li. One

possibility is that the 750 cm^{-1} peak belongs to Li_2O_2, where the O – O bond strength is different from that of the Li_2O_2 formed on the 1st cycle. Varying positions for the O-O stretch in Li_2O_2 formed during discharge have been reported in literature, with values between 745 cm^{-1} and 808 cm^{-1}.[86–89] The origins of this peak shift remain elusive; several factors that can potentially affect the bonding strength have been proposed, for example the crystallinity of Li_2O_2 , which can lead to peak broadening or peak disappearance,[90,91] or hydration of Li_2O_2, which can lead to a blue shift of up to 70 7 cm^{-1} .[89,92] It is likely that in this work this shift is caused by the local contamination on Li_2O_2 surfaces from LiOH or other species.

SEM images of cycled microlattice electrodes reveal a corresponding change in discharge product morphology with cycling. Figure 14. (a,b) shows the surface of the microlattice following the fourth discharge, at different magnifications. Clusters of "platelets" with cluster diameters between 5-10 μm were observed. Such Li_2O_2 "platelet cluster" morphologies have been observed before on NPG discharged in LiTFSI in DMSO as electrolyte,[57] and as freely distributed "platelets" on R-MnO_2 nanowires discharged in $LiCF_3SO_3$ with TEGDME as electrolyte.[93] The closest resemblance to our structures comes from discharge products formed on a 3-dimensional $NiCo_2O_4$ nanowire array/carbon cloth cathode (carbon cloth acting as a template for the growth of the nanowire array)[94] discharged in LiTFSI with DME as electrolyte. The authors of the study described their observations as "porous ball" shaped discharge products, with diameters ranging from hundreds of nanometers to a several microns. Selected area electron diffraction (SAED) of those particles confirmed that the products consisted of nanocrystalline Li_2O_2. The

spectroscopy results in this work indicate that these structures represent a combination of Li_2O_2, Li_2CO_3, HCO_2Li, and CH_3CO_2Li. Figure 14. (c) shows the surface after the fourth charge. We find a surface devoid of discharge products with the morphologies shown in Figure 14. (a,b).

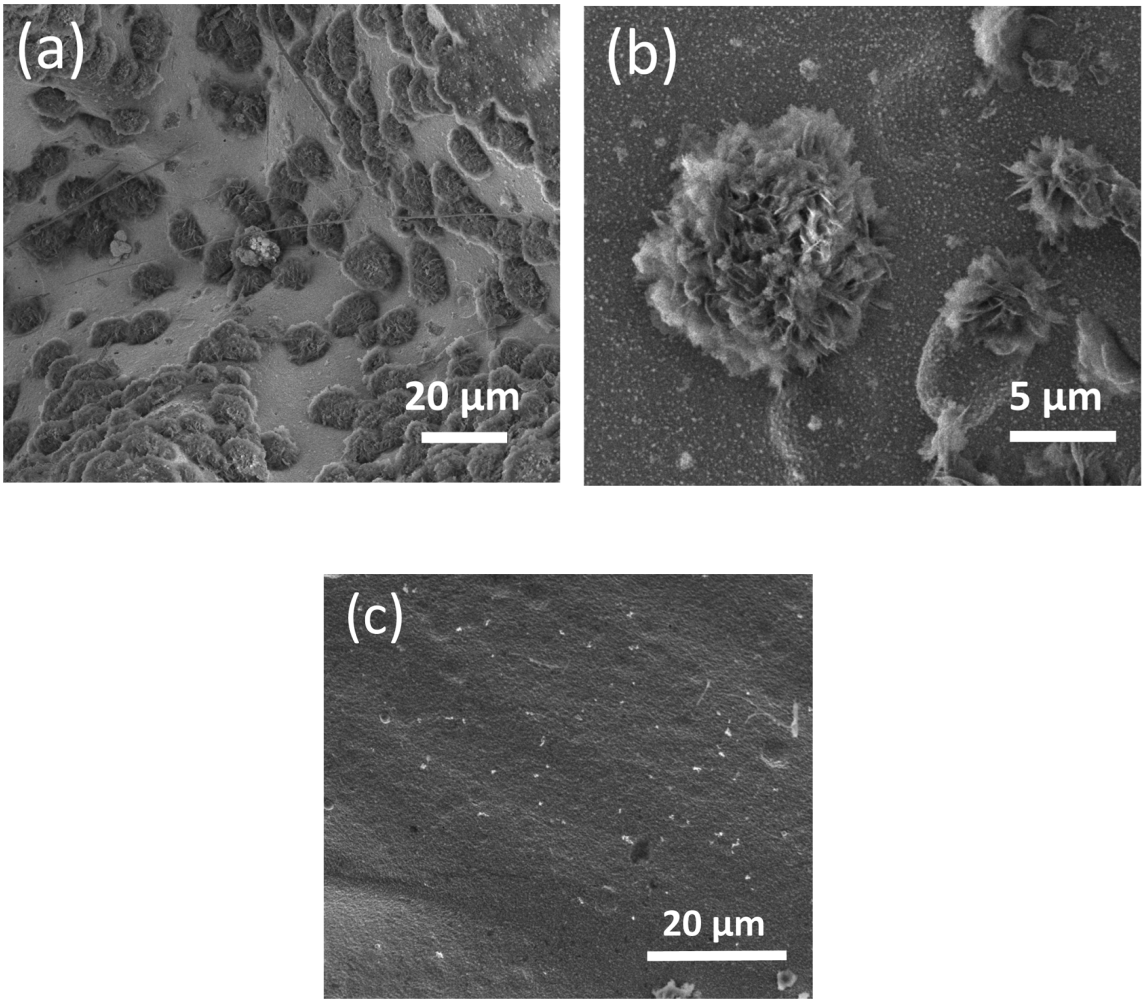

Figure 14.SEM images of a microlattice after (a,b) fourth discharge and (c) fourth charge.

2.5 Conclusions

We demonstrated the feasibility of using a 3-D architected microlattice as a positive electrode for Li-O_2 batteries. Using Au as the electrode material and DME as the electrolyte solvent, we observed the formation of toroidal-shaped Li_2O_2 as the predominant product after first discharge, their complete removal upon charge, and the accumulation of Li_2CO_3, HCO_2Li, and CH_3CO_2Li after multiple cycles. These findings demonstrate that 3-dimensional architected materials provide a useful test-bed when serving as electrodes for studying fundamental electrochemistry and discharge product morphology. Optimization of the geometry, unit cell size, and the electrode surface material used in the microlattices, is beyond the scope of this work. In general, optimally structured metamaterials for Li-O_2 electrodes will likely reflect a balance between several design constraints. These include the need for large pore volumes for mass transport (O_2 and possible discharge intermediate diffusion) and accommodation of discharge product, as well as maximum total electrode surface areas to sustain high-rate discharge or charge reactions with minimal overpotentials. The ability to decouple the microscale pore structure from the selection of surface composition and area, for example, through manipulation of the coating process and surface roughness, therefore represents a new direction in electrode design for metal-air systems. Future work studying Li-O_2 chemistry on different material surfaces while preserving the electrode geometry and mechanical integrity will provide insight on optimizing the chemical stability and catalytic activity of electrode materials toward ORR/OER.

Chapter 3

A Perovskite/Ni Microlattice Electrode for Li-O_2 Batteries

Adapted from:

Xu, C.; Shi, J.; Yang J.; Greer, J. R. *Three-Dimensional Perovskite/Nickel Microlattice Electrodes for Li-O_2 Batteries*. In preparation

In the previous chapter we demonstrated that a Au microlattice may act as an "air electrode" in a Li-O_2 cell. Large capacity was achieved per ECSA, and the open structure facilitated the post-test characterization of the reaction products. The well defined and periodic structure exhibits good electrical connectivity, and maintains its structural integrity throughout the duration of testing. The large pore size allowed for free transportation of Li^+ and dissolved O_2^- to the surface of the electrode, with no danger of "pore clogging" from discharge products, and as a result allowed for an even distribution of discharge products throughout the entire electrode. Our first investigation focused primarily on Au electrodes, and our results do not give us a compelling reason to continue using Au. Despite the promising results of Peng et al. in 2012,[9] recent studies have shown that Au does not offer extra stability when comparing to C, as OER/ORR values measured by DEMS gave a larger deviation from 1 in Au electrodes than in C electrodes.[22] Coupled with the high cost of Au, we have decided to move away from Au and focus on cheaper materials, with the

main objective being investigating material stability and catalytic performance. Figure 15. shows the discharge profile of microlattices with three different surface materials, Au, Ni, and Ti. The unit cell size is kept constant. Under the same discharge conditions, we see extremely low capacities for Ni and Ti compared to Au, with no discharge plateau, indication poor ORR kinetics.

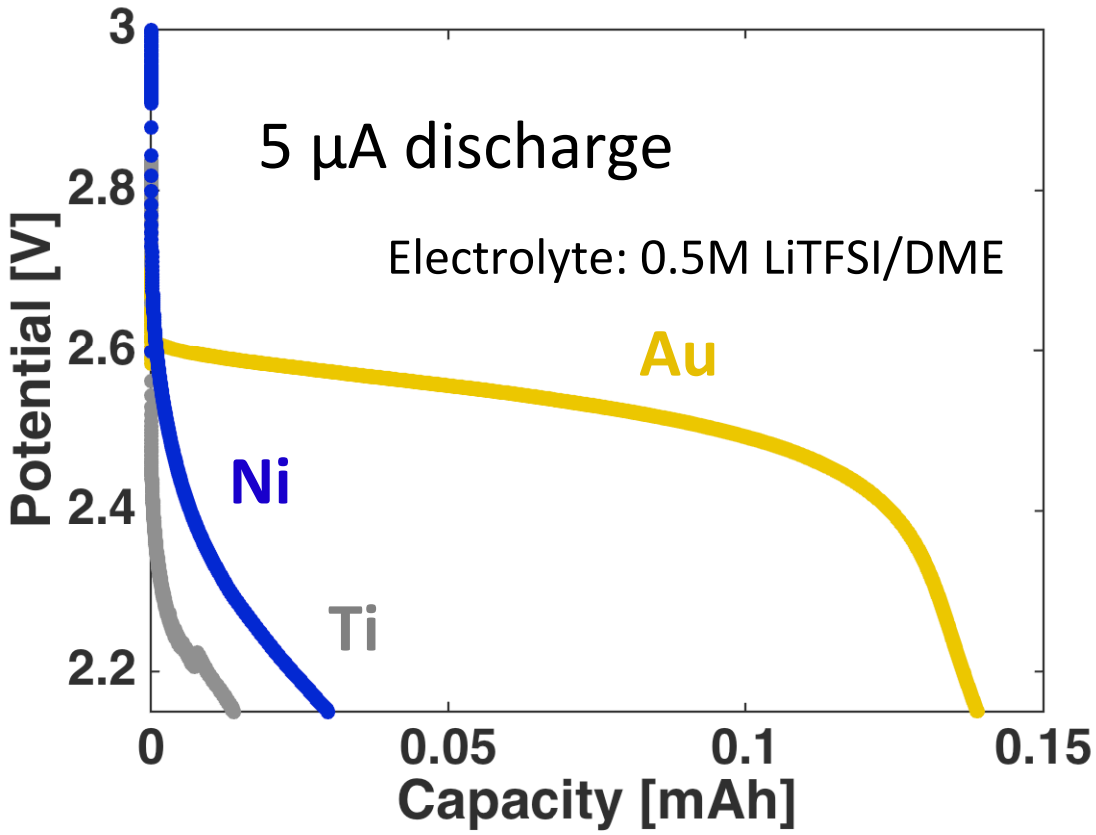

Figure 15. Discharge profile of microlattices with different surface material, at 5 µA and 0.5 M LiTFSI/DME electrolyte.

We then turned our attention to perovskites, as they have been known to have wide applications as catalysts in fuel cells and metal-air batteries, [95–98] due to their high oxygen

ion mobility and electrocatalytic property for ORR.[38,99,100] These properties are related to their high oxygen vacancy concentration.[100,101] Researchers have since then demonstrated perovskites as promising catalysts for ORR/OER. A few examples are given in Table 3.1.

TABLE 3.1

Various perovskites used as catalysts in a Li-O_2 cell. The discharge rate, and the capacity obtained, as well as the electrode configuration and specific area, are listed.

	Discharge Rate	Capacity	Electrode configuration	Specific surface area ($m^2\ g^{-1}$)
$La_{0.5}Sr_{0.5}CoO_{2.91}$[38]	50 mA g^{-1}	11059 mAh/g	Imbedded in activated carbon (AC)	96.78
$LaNiO_3$[102]	0.05 mA cm^{-2}	1.064 mAh cm^{-2}/40mAh g^{-1}	No substrate, binder	NA
$Sr_2CrMoO_{6-\delta}$[103]	75 mA g^{-1}	2306 mAh g^{-1}	SCM: Super P: PTFE 30:60:10	1.46
$La_{0.6}Sr_{0.4}Co_{0.9}Mn_{0.1}O_3$[101]	200 mA g^{-1}	3107 mAh g^{-1}	LSCM: Super P: PVDF 27:63:10 0.65 mg cm^{-2} loading	4.59
$La_{0.8}Sr_{0.2}MnO_3$[104]	0.1 mA cm^{-2}	1900 mAh g_{carbon}^{-1}	LSMO: Super P 1:1	32

Most of the above mentioned perovskites are mixed with high surface area carbon and binder, then cast onto a metallic mesh, most commonly Ni. This is standard practice in the Li-O_2 battery field, and essential when investigating perovskites, due to the low conductivity of perovskites. In this case the high surface area carbon acts as conductive

matrix that allows the perovskites access to electrons. However this calls into question what conclusions can really be made with testing of this composite electrode. Most studies using the composite electrode show enhanced capacity, better cyclability, and lowered overpotential compared to the reference pure carbon electrode. This confirms the superior catalytic properties of the perovskite, but one must caution in making claims about cyclability. The composite electrode maintains all the pitfalls of the pure carbon electrode, of which the biggest is the oxidation of C at the Li_2O_2/C interface,[40,41] leading to surface passivation and capacity fade. Furthermore, when looking at the composition of these electrodes in terms of surface area percentage, one arrives at the conclusion that the chemical composition of surface area available for ORR/OER is almost entirely carbon. Here we make a simple estimation. Many of the listed composite electrodes in Table 3.1 contain 50% or less perovskite by weight; the volumetric percentage of the perovskite is therefore expected to be much less due to the big difference in molecular weight between perovskites and C. Many of the above peroskites contain La, which has an atomic weight of 139; $LaNiO_3$ has a molecular weight of 246 compared to the 12 of C. Assuming density scales with molecular weight, a 1:1 weight ratio of $LaNiO_3$ and C would indicate a 1:20.5 volumetric ratio. We would therefore expect the surface area ratio to be similar to this value (or $\frac{2}{3}^{rd}$ power of this value, 1:13.4), although the exact value would also depend on particle size. We acknowledge that it is truly remarkable that such a small surface area percentage of perovskites may have such a profound impact in first discharge capacity, e.g. 2306 mAh g^{-1} ($Sr_2CrMoO_{6-\delta}$/Super P) versus 1434 mAh g^{-1} (just Super P) under the same discharge conditions, but the fact remains that much of the capacity and also capacity fade is due to

the carbon itself. The degradation of organic binders also play a non-negligible role in capacity fade,[105] as the decomposition product may passivate the carbon surface, or that the cathode would lose electrical connectivity.

We propose a carbon- and binder-free electrode that serves as a conductive matrix to perovskite catalysts. Following the tradition of using Ni foam as substrates for electrodes, we fabricated hollow 3D Ni microlattices as the substrate, and coated it with equal weight ratios of Ni and perovskite powder. The ORR/OER properties of Ni and the chemical stability of Ni under cell operation conditions are investigated. Three kinds of perovskites $LaCoO_3$, $LaNiO_3$ and $LaNi_{0.5}Co_{0.5}O_3$ are individually incorporated into the all Ni system, and their ORR/OER properties are compared.

3.1 Fabrication of the Perovskite/Ni Microlattice Electrode

Single phase $LaCoO_3$ (LCO) and $LaNi_{0.5}Co_{0.5}O_3$ (LNCO) were obtained by a sol-gel type reaction, following the procedure outlined in Lopez et al.[106] The synthesis procedure was done by Jingwei Shi, a Caltech Summer Undergrad Research Fellowship (SURF) student. $LaNO_3$ and $CoNO_3$ (Sigma Aldrich) were mixed in a 1:1 mole ratio in DI water for LCO; $LaNO_3$, $CoNO_3$, and $NiNO_3$ were mixed in a 2:1:1 mole ratio in DI water for LNCO. Chelating agents Ethylenediaminetetraacetic acid (EDTA) and citric acid were added to the solution, at a 1:1.5 mole ratio of total metal ions to each chelating compound. The pH of the solution was then adjusted to 10 with NH_4OH. After pH adjustment, a clear solution was obtained. The solution was placed on a hot plate with a magnetic stirrer and heated to

90°C to remove the water. Further evaporation was done by placing the solution in a drying oven at 120°C for 2 days. After evaporation, the resultant black gel was roughly powdered. Next, the black powder was placed in an alumina crucible and heated to 300°C in a tube furnace (make) to decompose the chelating agents and other organics. The LCO powder was further calcined in the same tube furnace at 700°C for 6 hours in air; the LNCO powder was calcined at 800°C for 20 hours in air. The finished perovskite powder was then crushed to a fine powder with a mortar and pestle. The purity of phase of the perovskite was confirmed via XRD. Small peaks arising from secondary phases of La_2O_3, NiO and CoO appear in Figure 16. (b,c). However the low intensities indicate relatively small amounts compared to the perovskites.

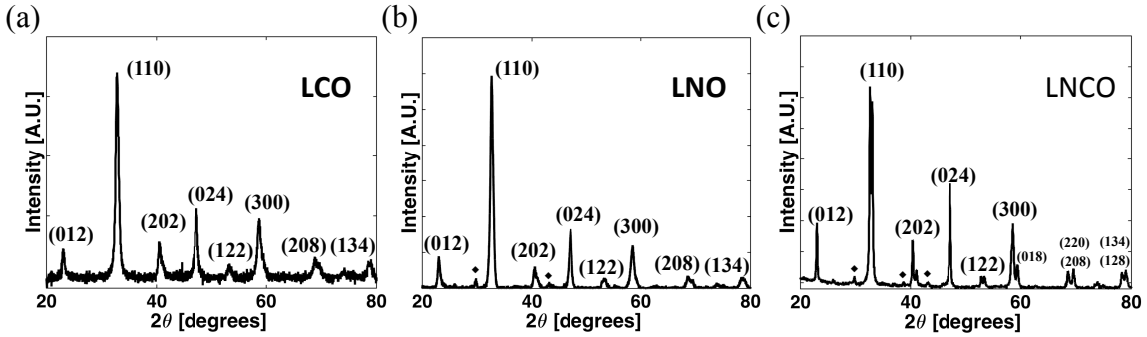

Figure 16. X-ray diffraction data of synthesized (a) LCO, (b) LNO, and (c) LNCO. The peaks indicated by ◆ in (b) at 30° and 43° correspond to La_2O_3 and NiO, respectively. The peaks indicated by ◆ in (c) at 30° correspond to La_2O_3, while those at 37°and 43° correspond to NiO and CoO.

The Ni microlattice is obtained by first sputtering a seed layer of Ti onto the sacrificial polymer obtained from HRL. The choice of Ti was due to the corrosion resistance of Ti in the electroplating solution (pH<5). The electroplating solution consists of $NiSO_4 \cdot 6H_2O$, $NiCl_2 \cdot 6H_2O$, and H_3BO_3 (Alfa Aesar) at concentrations of 224.675 g L^{-1}, 224.675 g L^{-1}, and 44.9 g L^{-1} in DI water, respectively.[107] Current was kept constant at 4.3 mA cm^{-1}. A thickness of >5 μm is achieved. Finally the sacrificial polymer is etched away using an etching solution (1.5MNaOH, in 1:1 v/v methanol and DI water). Etching was performed for 24 h at 40 °C,[108] after which the sample was thoroughly cleaned in DI water. The Ni microlattice was then immersed in a perovskite/Ni nanoparticle suspension and subsequently dried. This procedure was repeated 3 times. The suspension was prepared by mixing the perovskite powder with Ni nanoparticles (20 nm in diameter, US Research Nanomaterials, Inc) in a 1:1 mass ratio. 0.3 g of the mixed powder was then suspended in 7.5mL of tetrahydrofuran (THF) and sonicated for 1 hr. (Mass loading) Finally, the electrode was brought into and Ar glovebox and annealed on a hotplate at 390 °C for 5 hrs. This step was found to be crucial for achieving a high electrical connectivity of the nanoparticles on the surface of the electrode. Figure 17. shows the electrode at different magnifications.

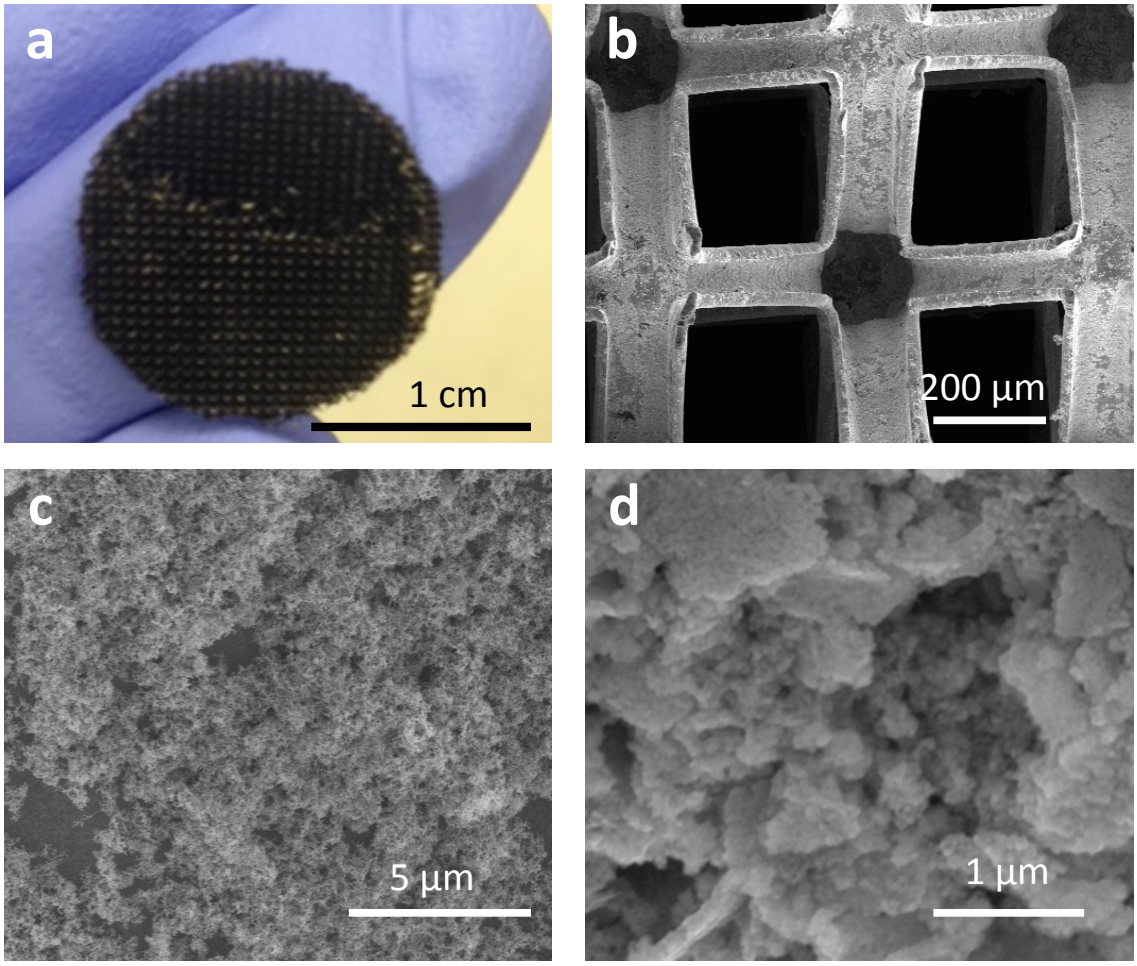

Figure 17. Hollow Ni microlattice electrodes coated with LCO/Ni nanoparticles.

3.2 Cell Assembly and Electrochemical Testing

The electrochemical cells were commercially available El-cells (EL-CELL GmbH, Germany). Assembled Li-O_2 cells comprised a Li metal anode, separator (Celgard 4560), and microlattice cathode. DMSO (anhydrous, water content 10-30 ppm, Sigma- Aldrich)

was dried for several days over freshly activated molecular sieves in the Ar glovebox. A 1.5 M $LiNO_3$ (Alfa Aesar, anhydrous, 99.999%) was added to the solvent to make the electrolyte. After assembly, the sealed cells were transferred out of the glovebox to be connected to an O_2 delivery channel (ultrapure stainless steel) and purged. Cells were then subjected to a rest step at open circuit in O_2 for 10 h to stabilize open circuit voltage (OCV) before discharge (the typical OCV was ~3.0 V vs Li). Electrochemical testing was performed using a Biologic SP-200 potentiostat. After testing, cells were opened and dissembled in an Ar glovebox, washed in DME, and vacuum-dried at room temperature for a minimum of 30 min in the antechamber of the glovebox.

3.3 Results and Discussion

Slurry-type electrodes typically require a porous mesh to offer mechanical stability. The macroporous Ni foam/mesh not only offers good mechanical stability but also good transport pathway for dissolved O_2, and as a result has been a dominant choice in the field.[43–45,101,109–115] However the stability of Ni under battery operating conditions has been called into question. Veith et al. investigated the chemical stability of plain Ni foam acting as the air-electrode in $LiPF_6$ ethylen carbonate/dimethyl carbonate (EC/DMC, 1:1 wt %) electrolyte.[47] Linear scanning voltammetry (LSV) was conducted under Ar and O_2 from 3.2 V to 4.5V. Figure 18. shows significant current above 3.8 V for both cases, indicating decomposition of electrolyte. Interestingly, larger currents are observed in the LSV curve

under Ar; at 3.8 V the measured current under Ar is more than an order of magnitude higher than that of under O_2. A similar effect is observed in Liu et al.,[48] where Ni is found to be far more stable under an O_2 environment. Figure 18.(a) shows our LSV data of Ni microlattices covered only in Ni nanoparticles, at a rate of 0.1mV/s. The measured current is normalized by the weight of the Ni nanoparticles. We see that in the $LiNO_3$/DMSO environment, Ni under Ar starts decomposing at a potential as low as 3.2 V, reaching a peak of more than 250 mA g^{-1} at 3.75 V. However we find Ni to be substantially more stable under O_2, with a current density below 1 mA g^{-1} in the potential range 3-3.8 V. Above 3.8 V, the current density gradually increases to a value of 27 mA g^{-1} at 4 V. These observations resonate with those made by Veith et al.[15] and Liu et al[48]. Liu et al. ascribed this observed stability due to the increased formation of a protective layer of NiO on the surface of the Ni. The authors supported this claim by a combination of XPS and Raman spectroscopy.

Figure 18.(b) shows LSV curves of Ni microlattice covered in Ni nanoparticles and Super P, both under O_2 environment. We see that from OCV to 3.8V, the current density is comparable between the 2 electrodes. Above 3.8V, the current density of the Ni nanoparticle electrode starts increasing dramatically, surpassing that of the carbon covered electrode. We therefore conclude that Ni is similar in stability to C below 3.8V, and may aptly assume the role of conductive host to perovskites, just as C was in literature. The cutoff potential is set to 3.8V in subsequent experiments, unless otherwise stated. Figure 18.(c,d) shows the cycling curves of the Ni and C covered electrode at the same discharge rate of 0.34 mA cm^{-2}, and charge rate of 0.17 mA cm^{-2}. We see the 1st discharge capacity of

C is ~1 order of magnitude higher than that of Ni. This is due to the superiority of the C ORR properties over Ni. The low capacity of Ni is a positive attribute if one hopes to use it as a conductive host to catalysts. In a composite electrode containing catalyst/host, a higher capacity contribution percentage from the catalyst would allow for better investigation of the catalytic properties of the catalysts, e.g. a pure Au electrode would allow for better understanding of Au as an air-electrode than a composite Au/C electrode. The charging profile of Ni is relatively consistent compared to that of C, exhibiting a slow decrease in capacity from 0.06 mAh cm^{-2} to 0.04 mAh cm^{-2}. The values for C are from 0.54 mAh cm^{-2} to 0.14 mAh cm^{-2}. The dramatic decrease in capacity for C is due to the sharp increase in charging potential: at 0.1 mAh cm^{-2} charge capacity, the charging potential rose from 3.47 V on the 1^{st} cycle, to 3.66 V on the 10^{th} cycle, and finally to 3.77 V on the 60^{th} cycle. Figure 18.(e,f) shows the capacity retention of a Ni and C electrode over 60 cycles. Capacity retention is calculated as the capacity of each cycle normalized by the largest discharge capacity obtained out of the 60 cycles. The discharge capacity of C in Figure 18.(e) sees a slight increase in capacity from the 2^{nd} to 4^{th} discharge. This is likely due to rearrangement/settling of the electrode, as reported by others.[3] The fact that we are not using binders may have caused this phenomenon. Although both electrodes exhibits pronounced capacity fade within the first 10 cycles, Ni exhibits a higher capacity retention, with a value of 0.5 on the 10^{th} cycle, compared to 0.28 for C. The capacity fade behavior of the first 10 cycles of the C electrode is similar to those reported elsewhere.[3] The average capacity retention between the 10^{th} and 60^{th} cycle is 0.4 for Ni, and 0.15 for C.

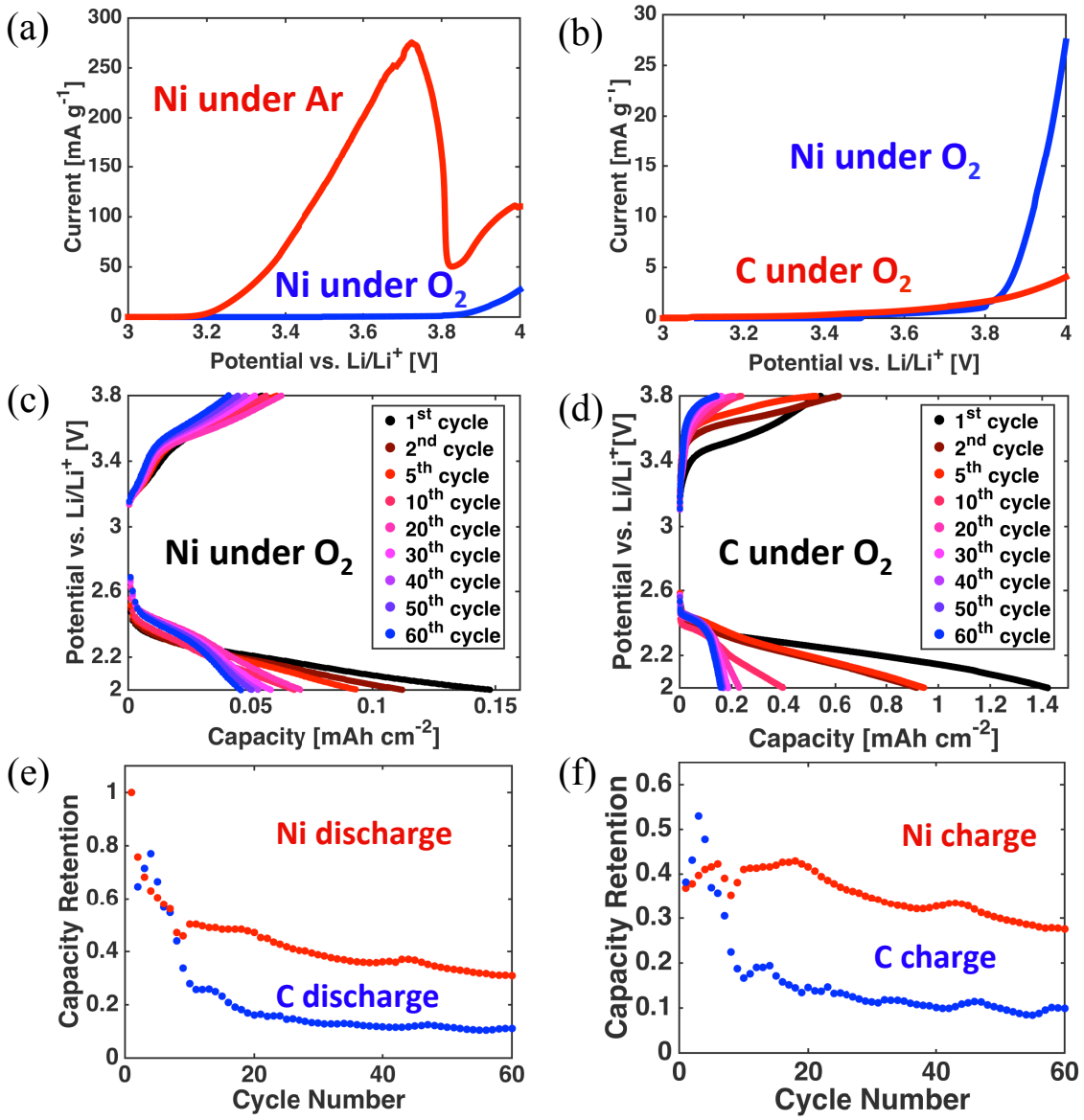

Figure 18. (a,b) LSV of Ni and C covered microlattice electrode under Ar and O_2 environments. Scan rate 0.1mV/s. (c,d) Galvanostic cycling of Ni and C covered electrode at 0.34 mA cm^{-2} discharge rate and 0.17 mA cm^{-2} charge rate. (e,f) capacity retention of Ni and C covered electrode over 60 cycles.

The better capacity retention of Ni compared to C may arise from a decreased level of carbonate formation during discharge, at the Li_2O_2/electrode interface, and the Li_2O_2/electrolyte interface. On a C cathode, Li_2CO_3 is formed during discharge at the Li_2O_2/electrode interface through the reactions:[40]

$$Li_2O_2 + C + \frac{1}{2}O_2 \rightarrow Li_2CO_3 \quad (5)$$

$$2Li_2O_2 + C \rightarrow Li_2O + Li_2CO_3 \quad (6)$$

This reaction will not happen on the Ni electrode surface. At the Li_2O_2/electrolyte interface, formation of either Li_2CO_3 or $LiRCO_3$(R=alkyl) arises from the contact of electrolyte and Li_2O_2. During charging, Li_2O_2 is oxidized first at lower potentials first (3-4V), while carbonate is mainly oxidized at >4V (evolving CO_2).[40] In our study, the much larger capacity of C means much more Li_2O_2 (higher Li_2O_2 surface area), and longer test time, which means much more total carbonate formation than Ni. The abovementioned two processes indicate that the carbonate formation on C after the very first discharge is much more than on Ni. As the first charge commences, Li_2O_2 is oxidized first, and therefore the percentage of carbonate increases, and the charging potential must also increase in order to maintain the galvanostatic charging current. At a cutoff potential of 3.8V, it is foreseeable that most carbonate are not oxidized. At this point, the total quantity of carbonate on the C electrode may be much more than that present on the surface of the Ni electrode. During the 2nd discharge, the Ni electrode suffers much less surface passivation and may therefore form a higher ratio of Li_2O_2 (compared to C) by the end of the 2nd discharge, leading to

lower 2nd charge potential. With increased cycling, the disparity in capacity retention increases, as is apparent in Figure 18.(c,d), between the two electrodes, due to different carbonate accumulation rates between the two electrodes. The different carbonate accumulation is shown in FTIR data in Figure 19., where the carbonate peaks centered at 1410 cm^{-1} and 860 cm^{-1}.

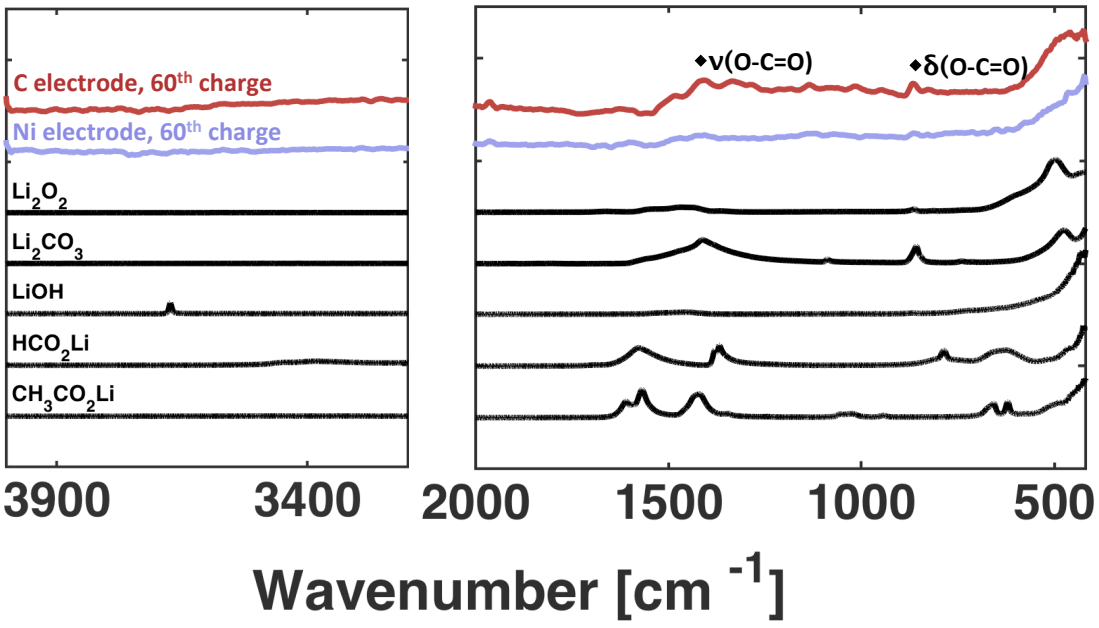

Figure 19. IR spectra of a C and Ni electrode, after the 60th charge.

We proceed to mix equal weight ratios of LCO, LNO and LNCO with Ni nanoparticles, respectively, and coat the microlattice with the particles. In Figure 20. (a-c) We show galvanostic cycling with discharge rates of 0.34 mA cm^{-2}, and charge rate 0.17 mA cm^{-2}. The LNO/Ni electrode exhibits the largest 1^{st} discharge capacity, at 0.8 mAh cm^{-2}, compared to 0.16 mAh cm^{-2} of LNO/Ni, and 0.3 mAh cm^{-2} of LNCO/Ni. The discharge capacity of the LNO/Ni electrode starts to steadily increase after the 4^{th} cycle, as did the charge capacity. The LNCO/Ni electrode exhibits a charging plateau at 3.6 V, after which the potential rises slowly, extending beyond the discharge capacity while showing no signs of dramatic increase. This is a clear sign of electrolyte decomposition. The steady increase in capacity of the LNO/Ni electrode warrants further investigation, as will be discussed shortly. Figure 20. (d-f) shows the capacity retention of all 3 electrodes. The capacity retention of the LCO/Ni electrode drops to 0.67 at the 2^{nd} discharge, reaches 0.5 at the 10^{th} cycle, then proceeds to decrease slowly to 0.33 at the 60^{th} cycle. The average discharge retention between the 10^{th} and 60^{th} discharge is 0.43. LNO/Ni shows a decrease in discharge retention in the first 3 cycles, after which it increases gradually and shows signs of plateauing after the 15^{th} cycle. The discharge retention of LNCO/Ni decreases the quickest out of the three electrodes, reaching 0.26 after only 17 cycles; the charge capacity exhibits must be manually restricted during the first 6 cycles, after which it drops to 0.28 by the 8^{th} cycle, and stays relatively constant after that.

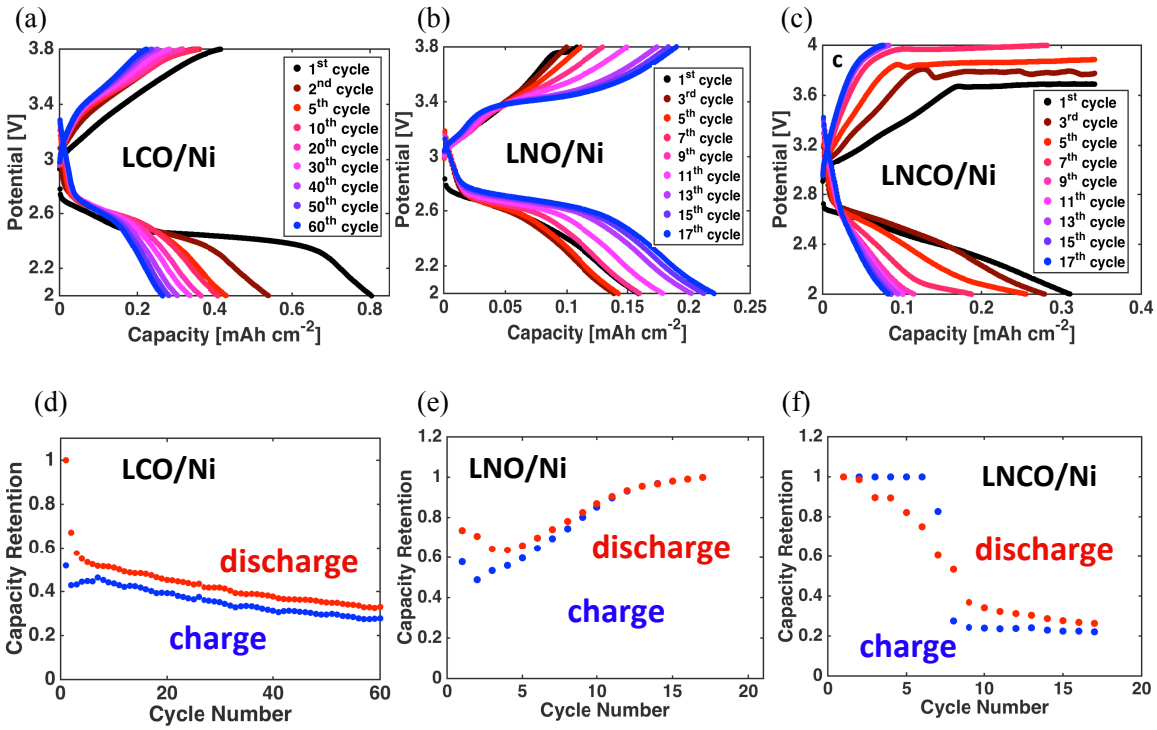

Figure 20. (a-c) Galvanostatic cycling of perovskite/Ni electrodes, with 0.34 mA cm^{-2} discharge rate and 0.17 mA cm^{-2} charge rate. (d-f) discharge and charge capacity retention of the electrodes.

We showed that out of the 3 perovskites, only LCO shows good catalytic properties and chemical stability. We proceed to investigate the morphology and chemical composition of the discharge product of the LCO/Ni electrode. Figure 21.(a) shows the surface of the electrode after a discharge at 0.056 mA cm^{-2}, with a capacity of 11.9 mAh cm^{-2}. We see large clusters of platelets arranged into toroidal shapes, with diameters in the range between 5 -10 μm. The inset shows a higher magnification of an individual structure. Energy Dispersive Spectroscopy (EDX) maps in Figure 21. (b,c) reveal that these structures

contain high concentrations of O. Figure 21. (d) shows that they do not appear to contain concentrated levels of C. The large size of the structures indicate a solvation dominated Li_2O_2 growth process. The $LiNO_3$/DMSO combination has been shown to exhibit superior discharge capacity.[116,117] It has already been established that DMSO promotes the solution-mediated process due to high DN; NO_3^- anion also has a high DN of 22.2kcal/mol, compared to 11.2 kcal/mol of $TFSI^-$, the anion of LiTFSI, a popular salt for Li-O_2 electrolyte.[116]

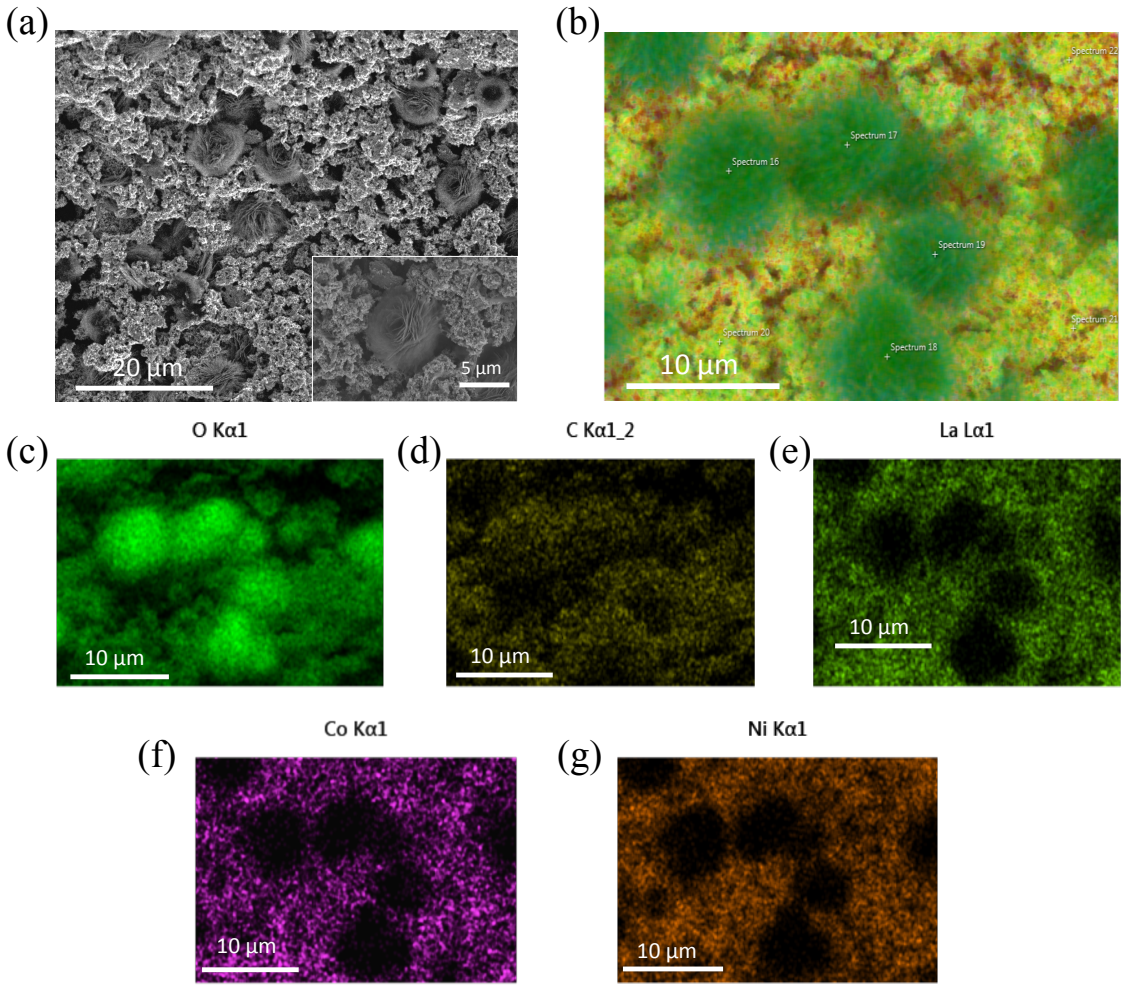

Figure 21. SEM image and EDX map of the surface of a discharged LCO/Ni electrode.

Figure 22. shows the FTIR data of the surface of the LCO/Ni electrode after various testing conditions. The references are obtained from commercial powders (Sigma Aldrich). We see that after the 1st discharge, a large broad peak is present at lower wavenumbers, whose left shoulder begins at 640 cm^{-1}. This broad peak is most likely a combination of Li_2O_2, LCO and $LiRCO_3$. The peak centered at 1410 cm^{-1} and 860 cm^{-1} are attributed to carbonate species. After the charge, we see that the intensity of both the carbonate and Li_2O_2/LCO/$LiRCO_3$ peak decrease, but does not disappear. This is expected, as the low cutoff potential of 3.8V prohibits the full oxidation of carbonate discharge products. The signal from the residual carbonate increases from the 1st charge to the 60th charge, due to the accumulation of carbonate after each cycle. We also see the presence of a small peak at 3675 cm^{-2}. This is attributed to the O-H stretch, which we also observed after cycling in our previous work.[108] While previously the electrolyte was anhydrous DME with LiTFSI, we had attributed the O-H peak to LiOH formation due to Teflon O_2 delivery line. In the current study, this was ruled out due to the delivery line upgrade ultrapure stainless steel.

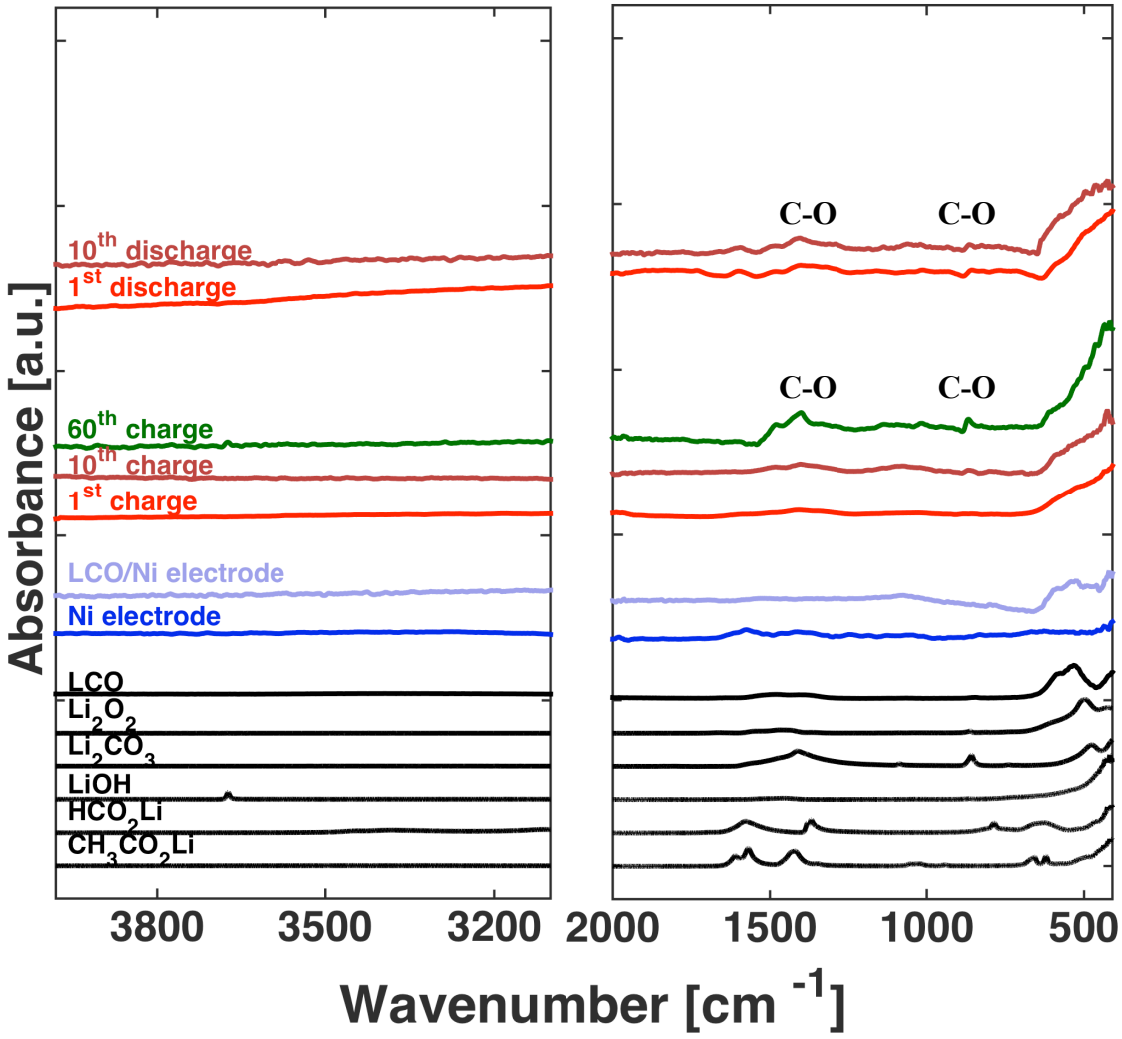

Figure 22. FTIR data of the surface of the LCO/Ni electrode after various cycles.

Figure 23. (a-b) shows the Raman spectra of the surface of a LCO/Ni electrode discharged to 21 mAh. Figure 23.(a) shows the presence of Li_2O_2 and $LiCO_3$. At higher Raman shift, a sharp peak at 3674 cm^{-1} indicates the presence of LiOH, shown in Figure 23. (b). The inset

at the upper right corner is an optical image showing the surface of the electrode. The Raman laser spot lies within the crosshair area (empty space at the center of the screen), with a diameter of ~10 μm. The inset shows that the Raman laser is aimed at a cluster of white aggregates, from which the Raman spectra shown in Figure 23 (a,b) is generated. Focusing the laser in darker regions does not generate a pronounced LiOH peak. We therefore conclude that this cluster is the observed discharge product shown in Figure 21. Figure 23. (c) show the FTIR spectra of the $LiNO_3$/DMSO electrolyte that has undergone various numbers of cycles. Comparing to the pristine electrolyte, we see a clear trend of increasing peak intensity at wavenumbers 1141 cm^{-1}, 765 cm^{-1}, 498 cm^{-1} and 463 cm^{-1}. All four peaks are associated with SO_2 vibration modes.[24,118,119] The reaction of DMSO with O_2^- to form $DMSO_2$ and OH^- has been observed by other groups.[24,118] The increased intensity of SO_2 bands arises not from the increase of cycle number but from the testing time. After the 1st discharge (~2.5 hrs), there is no discernable signal from $DMSO_2$, indicating that most of the discharge product is Li_2O_2. At the end of the 10th cycle (~33 hrs), we observe a small peak at 1141 cm^{-1}. At the end of the 60th cycle (~197 hrs), the peak at 1141 cm^{-1} is substantially increased, while 3 more peaks at 765 cm^{-1}, 498 cm^{-1} and 463 cm^{-1} appeared.

3.5 Chemical stabilities in the LNO/Ni system

We show the IR spectra of both the surface of the LNO/Ni cathode and the electrolyte after 17 cycles, in Figure 23. and 24., respectively. We see a presence of carbonate on the surface of the cathode, but no hydroxide. We therefore rule out the cause of the capacity increase show in Figure 20.(c) to be moisture contamination. Figure 24. shows that we do have $DMSO_2$ formation, however that does not necessarily lead to capacity increase, as we

observe $DMSO_2$ peaks in the LCO/Ni system too with no capacity increase. However, a broad and strong hydroxyl peak centered at around 3400 cm^{-1} indicates a decomposition pathway not found in the LCO/Ni system.

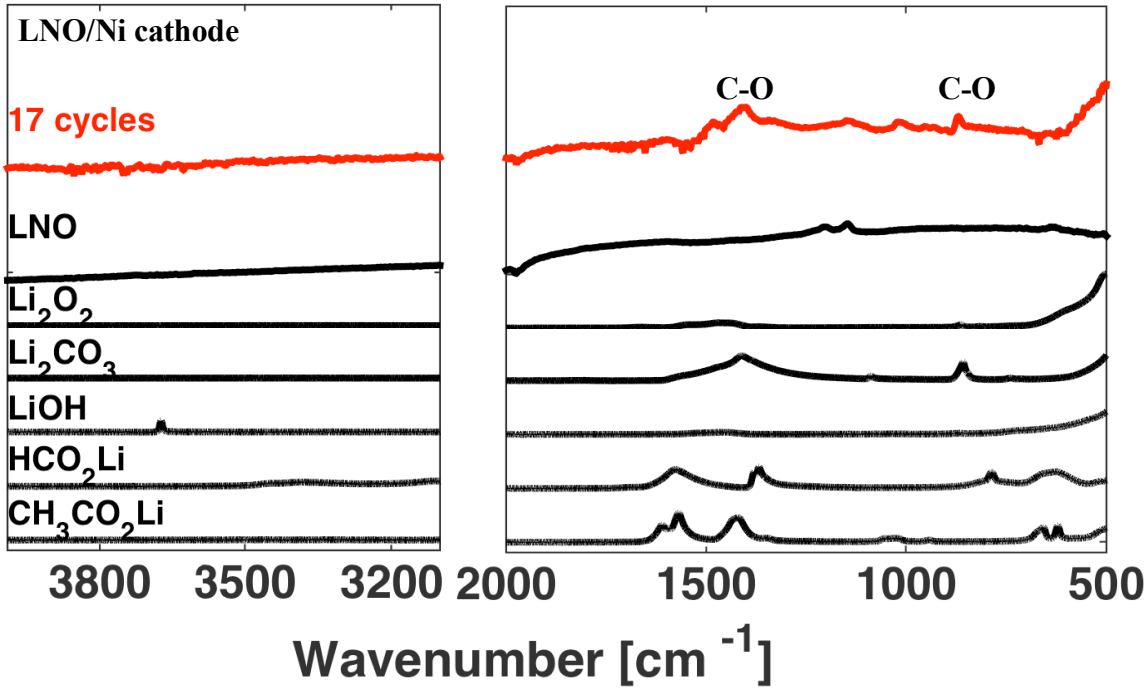

Figure 23. IR spectra of the surface of an LNO/Ni cathode after 17 cycles.

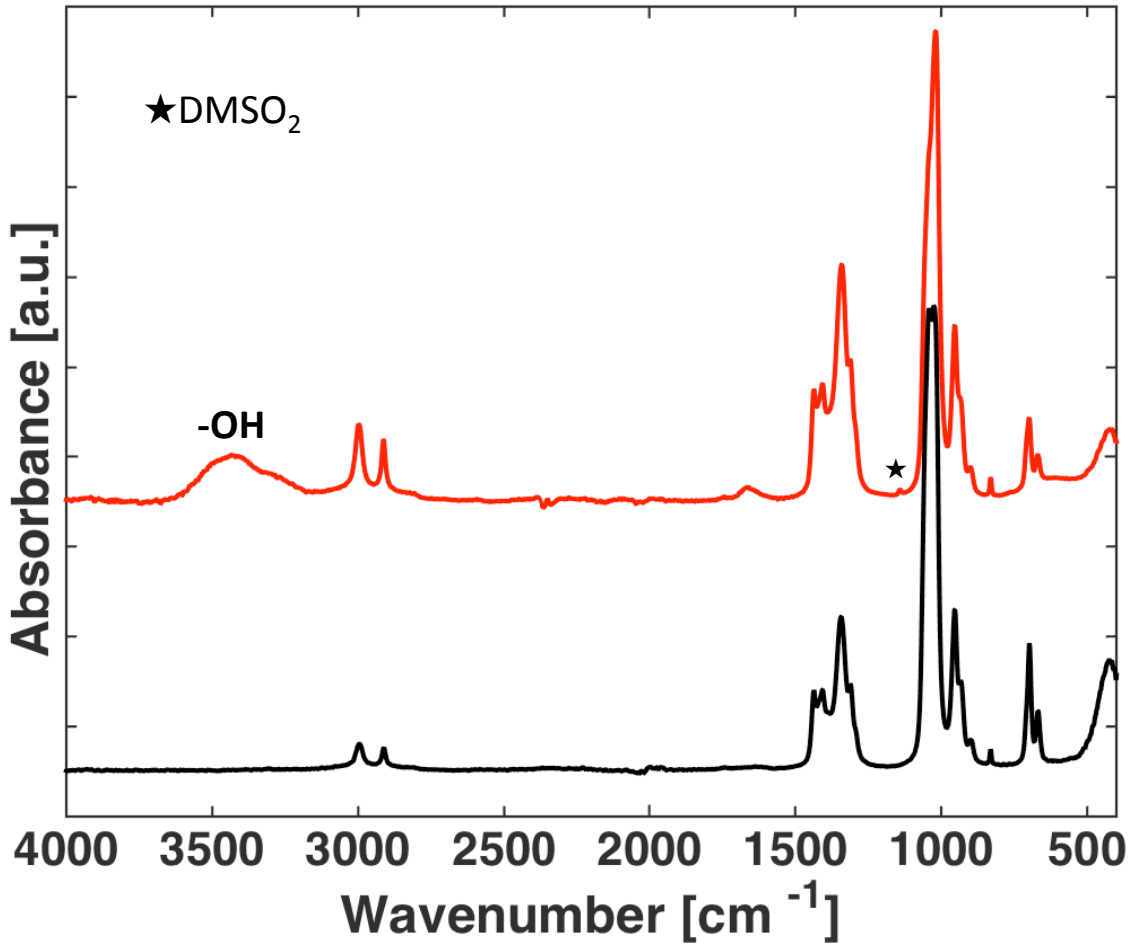

Figure 24. IR spectra of the electrolyte of a LNO/Ni cell after 17 cycles.

3.6 Conclusions

In this study, we have demonstrated a carbon and binder free microlattice matrix that can be used to investigate the ORR/OER properties of catalysis. Under appropriate operation conditions, Ni shows comparable stability to C in terms of decomposing electrolyte, while showing superior cyclability. This is partially due to the weak ORR properties of Ni, and

therefor the lack of side reaction product buildup. Three different perovskites, LCO, LNO, and LNCO, are mixed with Ni nanoparticles and cast onto a Ni microlattice. The electrolyte used is 1.5 M $LiNO_3$/DMSO electrolyte. LCO was found to exhibit the best ORR property while inducing the minimum amount of electrolyte decomposition. LNO performed less well in terms of ORR, and induced electrolyte decomposition. LNCO was found to severely decompose the electrolyte above a potential of 3.6V. Further investigation revealed inherent instabilities between DMSO and the intermediate superoxide species of the discharge product, which lead to the formation of $DMSO_2$ and LiOH, supporting the claims of other studies.[23,24] SEM images of the discharge product reveal morphologies indicative of toroid-to-platelet transition.

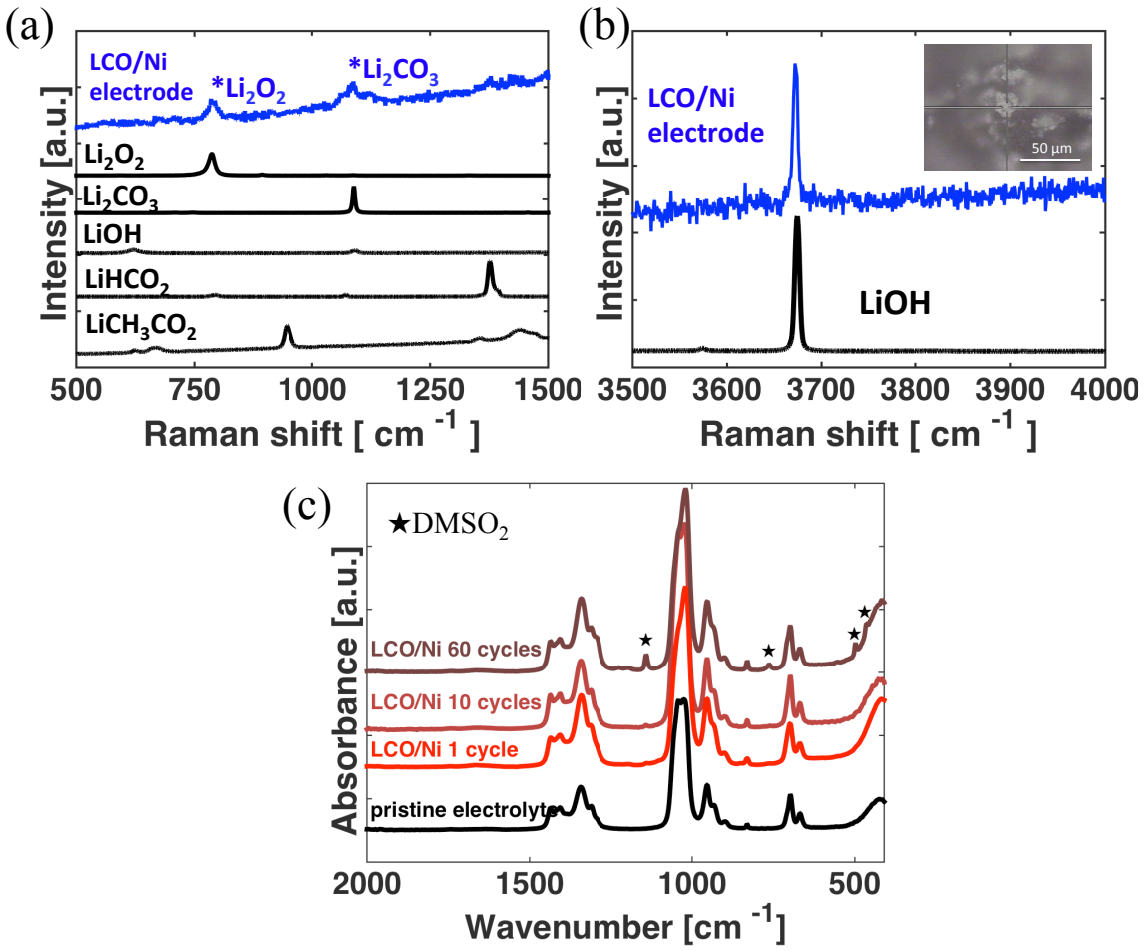

Figure 25. (a,b) Raman spectra of the surface of a electrode discharged to 22 mAh. (c) FTIR spectra of the electrolyte after various cycles.

Chapter 4

Enhanced Strength and Temperature Dependence of Mechanical Properties of Li at Small Length Scales and its Implications for Li Metal Anodes

Adapted from:

Xu, C.; Ahmad, Z.; Aryafar, A.; Viswanathan, V.; Greer, J. R. The *Enhanced Strength and Temperature Dependence of Li at Small Length Scales and its Implications for Li Metal Anodes.* (Submitted, arXiv ID:1606.05826)

The previous two chapters focused on the cathode of Li-O_2 batteries, a battery based on a novel chemistry that has the potential to increase the energy density of current secondary batteries by a factor of five. One underlying assumption of such a claim is that a Li metal anode is used. As shown in Figure 1., the energy density of Li metal is 3860 mAh g^{-1}, much higher than the <1000 mAh g^{-1} energy density of other anode materials. The incorporation of a Li metal anode, coupled with an advanced cathode, into a Li-ion cell could lead to a specific energy of 400 Wh/kg at the cell level, which represents 200% improvement over current state of the art.[3] Despite over 40 years of research, overcoming the uncontrollable dendrite growth during cycling has remained an insurmountable obstacle for Li-based

components.[7] Among multiple attempted approaches to eliminate or even reduce the dendrite growth, mechanical suppression has emerged as one of the most promising routes. The pioneering theoretical work by Monroe et al. showed that SPEs whose shear modulus is roughly twice that of Li could suppress dendritic growth through compressive forces.[120] This led to enormous interest in demonstrating cells with polymer electrolytes, inorganic solid state Li-ion conductors, and ceramic thin films.[7] Ferresse et al. further demonstrated that the elastic modulus of the separator also affects dendrite growth because it causes the stress in the separator to build up to beyond the yield strength of Li, which causes the anode to plastically deform and flatten out.[121] Applying external pressure higher than the yield strength of bulk polycrystalline Li in a direction perpendicular to the cell stack has also been shown to limit dendrite growth and prolong cycle life.[122–124]

These approaches have had limited success, and many unsolved questions regarding mechanical suppression remain. For example, dendrites form and grow through the grain structure of Li garnet solid electrolytes even though their shear modulus is >50GPa, a value predicted to be sufficiently high to suppress dendrite growth.[125] Applying an external pressure above what is believed to be the yield strength of Li also does not fully eradicate dendrites most likely because of the dearth of high-fidelity mechanical properties data for Li. Elastic modulus of polycrystalline Li has been reported to range from 1.9 GPa to 7.9 GPa,[126–129] and its yield strength – from 0.41 MPa to 0.89 MPa.[128,129] Such a significant variation in both has been attributed to the differences in sample preparation methods, i.e. melting and annealing conditions, reactivity with atmosphere, and experimental error. A key reason for the lack of solutions to overcome the Li dendrite growth challenge may be that the mechanical properties of Li at small scales are expected to drastically differ from

those in its bulk form; most single crystalline metals at the micron- and sub-micron scales have been shown to be up to an order of magnitude stronger compared with their bulk form.[130] During charging, crystalline Li whiskers with diameters on the order of a few hundred nanometers have been observed to nucleate on the anode surfaces,[131] growing into dendrites up to several millimeters long. The size-*independent* properties, such as the elastic and shear moduli, are generally functions of crystallographic orientation, and are particularly sensitive to it in Li, whose anisotropy factor is 8.52 at room temperature.[132] The mechanical properties of Li at high temperatures are also largely unknown. Current SPEs require an operating temperature of 333 K to 363 K (60 °C to 90 °C) to achieve the desired ionic conductivity (10^{-3} S/cm) and strong adhesion to the electrodes. Li's low melting temperature of 453 K (180 °C) suggests that even a modest temperature elevation will likely have a dramatic effect on its mechanical properties.

4.1 Fabrication of Mechanical Testing Samples

Li granules (Sigma Aldrich) were melted on a hotplate in an Argon glovebox at 180 °C, then cooled down to room temperature over 4 hours. The sample was then cut with a surgical blade to reveal a shiny metallic surface, from which we fabricated the nano- and micro-compression samples. This parent Li sample was placed into an airtight transfer module called Vachushut (Agar Scientific), shown in Figure 24., and carried from the glovebox to the SEM without exposure to the atmosphere. Ar was used to vent the SEM. Once inside the SEM chamber, the lid of the Vacushut self-opened as the chamber was pumped down to vacuum. We fabricated cylindrical pillars with diameters ranging from

980 nm to 9.45 μm in a Focused Ion Beam (FIB) (Versa DualBeam, FEI); the aspect ratio (height/diameter) was maintained between 3:1 and 5:1. The tops of the pillars were polished in the FIB to minimize surface roughness.

Figure 26. Image of the Vacushut (Agar Scientific) device. Obtained from https://www.int.kit.edu/downloads/INT_Research/Flyervacushut.pdf.[133]

4.2 Mechanical Testing

After fabrication, the sample was carried in the Vacushut from the FIB to the *in-situ* nanomechanical instrument, SEMentor (InSEM, Nanomechanics, Inc and FEI), shown in Figure 25. SEMentor allows us to simultaneously capture the real-time deformation video and to collect mechanical data during the experiments. Samples were compressed using a

custom-made diamond flat punch tip with a diameter of ~12 μm, and all experiments were conducted under a constant nominal strain rate of 5×10^{-3} s^{-1}. Engineering stresses and strains were calculated by dividing the applied force and displacement by the initial cross-sectional area and pillar height, respectively. The initial cross-sectional area was calculated based on the SEM images, using the pillar diameter measured at halfway along the pillar height. We accounted for the compliance of the substrate using Sneddon's correction.[134] SEMentor is equipped with a heating module located directly underneath the sample mount, which allows us to heat the sample up to 200 °C. We used a thermocouple located within the sample mount and connected to a PID temperature controller (Lake Shore Cryotronics, Inc) to carefully maintain the sample at the set temperature. We found that the sample stabilized at 363 K (90 °C) after 3 hours. To avoid significant thermal drift, i.e. recorded displacement caused by thermal expansion of the tip/sample and possible temperature fluctuations during compression, the tip was placed in contact with the lithium substrate for at least 3 hours to equilibrate the temperature before each test. We recorded typical thermal drift after each test to be <5 nm/s, which we used to correct the stress-strain data. After compression, we transferred the Li sample to another SEM (Zeiss 1550VP FESEM) to determine the crystallographic orientations of each pillar using Electron Backscatter Diffraction (EBSD). This was done post-compression because the Vacushut is not compatible with the Zeiss SEM, and therefore the sample must be removed from the Vacushut and temporarily exposed to air before doing EBSD. This proves to greatly affect the mechanical properties of Li, as will be

discussed in the next section. Therefore it is essential that we employ a new piece of Li every time the above-mentioned sequence of experiments was conducted.

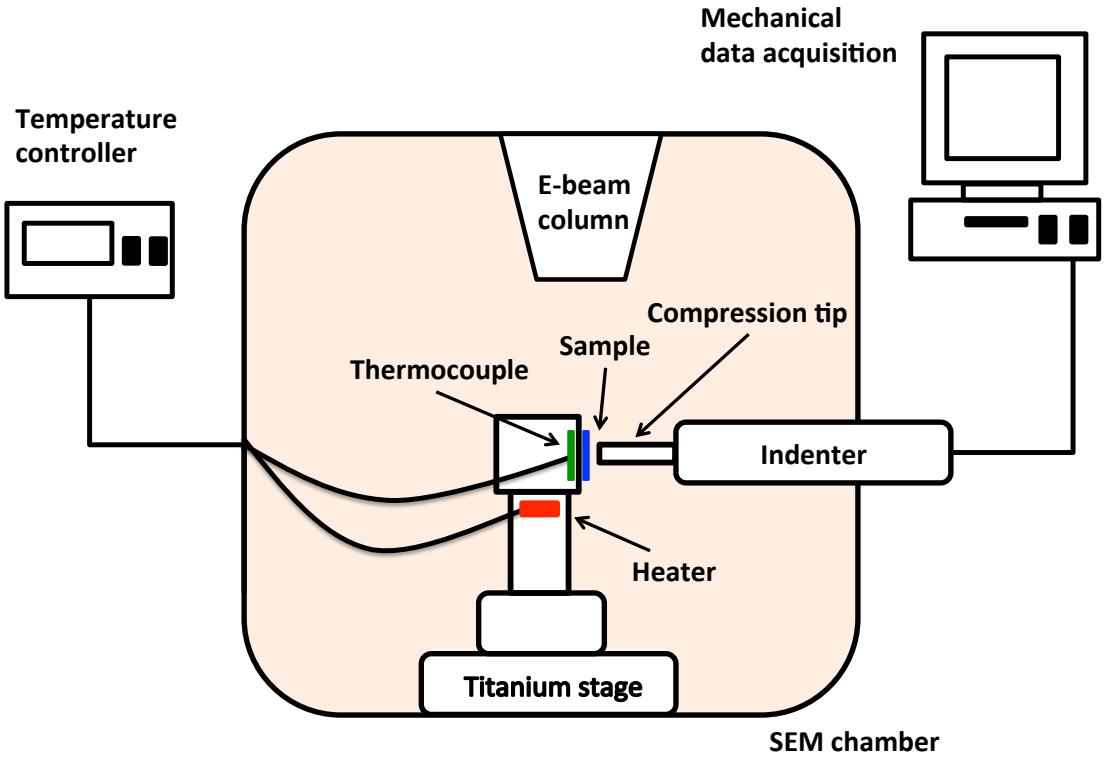

Figure 27. Schematic of SEMentor. Based on Lee et al.[135] Modifications were made to his original system to achieve above room temperature testing.

4.3 The Effect of Atmospheric Contamination

In the course of this work, we learned that even a 30 second exposure to the atmosphere causes severe oxidation in Li, which manifests itself in a dramatically different mechanical response. Figure 26.(a) representative stress vs. strain curve of a 4.80 μm-

diameter pillar that has been exposed to air for 10 seconds and then compressed. The plot shows the yield strength to be ~200 MPa, after which the sample catastrophically failed, which is ~4 times higher than the ~50 MPa yield strength of a typical un-oxidized sample. This is likely due to the immediate formation of LiOH, Li_2O, and Li_3N, which would have greater strength compared with Li. The post compression image shown in Figure 4.3(b) clearly reveals charging of the pillar, consistent with the formation of insulating oxides through a significant portion of the pillar. Currently we cannot fully rule out the possibility of Li reacting with residual gases in the SEM chamber when it is fully pumped down. We use high purity Ar to vent the SEM chamber during transfer, and we modified the venting conditions so that Ar is constantly purging the chamber (blowing out) as we mount the sample. However, even under these conditions it is likely that some O_2, N_2, and moisture have been introduced into the chamber. When the SEM chamber is fully pumped down, the residual gas that contain some percentage of O_2, N_2, and moisture may react with the surface of the Li over time, creating a coating of oxide and nitride. Therefore the mechanical properties we observe may contain contributions from the coating as well. While we cannot currently determine the thickness of this coating, our experimental data indicates that the coating was not enough to significantly alter the Young's modulus of our samples. The unloading section of our stress – strain data gives the Young's modulus of the corresponding pillar with a certain crystal orientation. Theoretical calculation gives a range of 3.00 GPa to 21.2 GPa (detailed description given in later section). In our tests, out of the 21 room temperature samples, none exhibited a Young's modulus greater than 21.2 GPa, and the majority of the values fall below 10

GPa, with a mean value of 4.76 GPa. Had the compression pillars contained a high percentage of Li oxide/nitride, we would expect the measured Young's modulus to be much higher, given that oxides and nitrides usually have a Young's modulus higher than 70 GPa.[136–138] We would also like to point out that a composite Li pillar, one that is covered by a Li containing chemical compound, may be closer to what is formed in a real electrochemical environment, as an SEI is expected to form as soon as the Li surface comes in contact with the electrolyte.

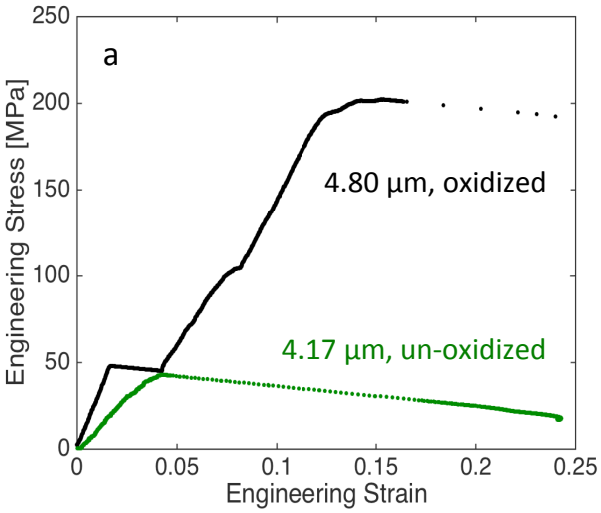

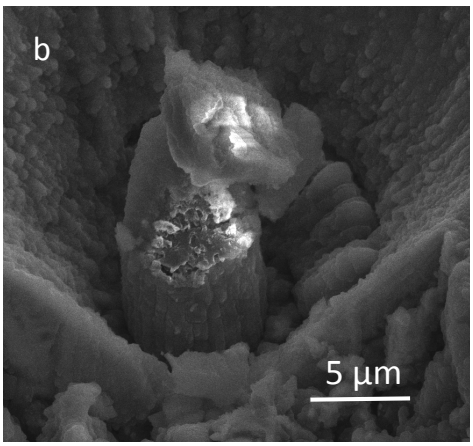

Figure 28. Compression results of oxidized and un-oxidized pillar. (a) Engineering stress vs. engineering strain data of the compression of a 4.8 μm oxidized pillar, compared with the data of a 4.17 μm un-oxidized pillar. The 1st strain burst during loading is due to cracks formed via oxidation. (b) Post-compression image of the oxidized pillar. White parts due to the charging effective of non-conductive material.

4.4 The Effect of Ga^+ on the Mechanical Properties of Li

Indentations are performed on FIB'd and as-cut Li surfaces. Ion beam with a 30nA current was used to polish the surface of as-cut Li at a grazing angle. We performed nanoindentations to a depth of up to 3 μm to match the deforming indentation volume to that of the pillars. The load vs. displacement data is for the FIB-polished and as-cleaved Li surfaces is shown in Figure 27. and reveals that these surface treatments lead to statistically indistinguishable mechanical properties. These results are consistent with multiple previous reports, which demonstrated that FIB-irradiation did not significantly affect the strength and deformation of metallic micro- and nano-pillars.[134,139]

Figure 28.Load controlled indentation of Li metal with a cleaved surface (red) and FIB polished surface (blue). The conditions for the FIB are 30keV acceleration voltage and 30nA current.

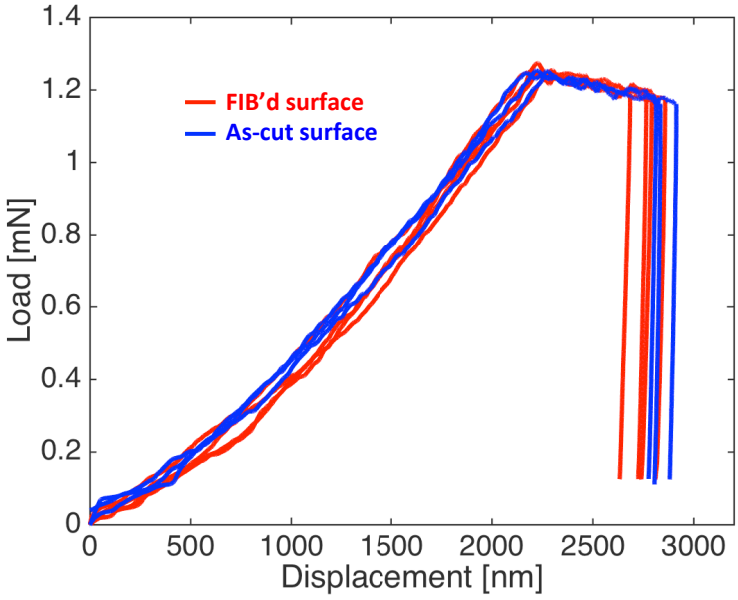

4.5 Identifying the Crystal Orientation of Pillars

We show the grain structure of melted and then subsequently cooled down Li metal in Figure 28.(a,b). EBSD was conducted on a blade-cut surface showing a mirror finish. Chemical polishing has been unsuccessful in further smoothing the surface. Nash *et al.*[140] found that methanol was the best etchant for Li metal, and that repeated actions of etching in methanol for a few seconds and then rinsing in xylene would allow for visual observation of grain boundaries. However this process must be done in the open air. If the same procedure was followed in an Ar atmosphere, a white crust forms on the surface of Li as soon it is removed from methanol. This is exactly what we have found in our studies. Ethanol and isopropanol was also used, to no avail. Preparation of Li metal outside the glovebox, though it may allow for visual observation of grain boundaries, introduces an oxide layer that makes it impossible to characterize the underlying Li using EBSD. It will also jeopardize the chemical integrity of any subsequently FIB'd pillars,

and dramatically change the mechanical properties as described in section 4.3. We have thus identified the best way to characterize the crystal orientation of pillars is to do EBSD after compression has been done, with no additional polishing. This still leaves the issue of a brief period (~5s) of exposure to air during the transfer of the Li into the SEM chamber, as the Vacushut does not fit into the ZEISS SEM. This exposure is enough to lower the EBSD indexing rate, as shown in Figure 28. (a,b). Regardless, the indexed points are sufficient in indicating the average grain size of our lithium sample, around 250±86 μm. The fact that our pillars, with diameters less than 10 μm, are much smaller than the average grain size leads us to conclude that our pillars are single crystalline. This assumption is often used in the nanomechanical community when studying polycrystalline material.[141] An instance of this is shown in Figure 28.(c). In some instances however it is difficult to identify which particular grain the pillars belong to, as shown in Figure 28. (d). In these cases, in order to obtain the crystal orientation of pillars to calculate the Schmidt factor, we utilized the relation between the elastic modulus of a particular grain and its miller indices as given below:[142]

$$\frac{1}{E_{hkl}} = s_{11} - 2(s_{11} - s_{12} - \frac{1}{2}s_{44}) \cdot \frac{h^2k^2 + h^2l^2 + k^2l^2}{(h^2 + k^2 + l^2)^2} \tag{4.1}$$

where h, k, and l are the miller indices of the respective grain, S_{11}, S_{12} and S_{44} are the elements of the compliance matrix, and E_{hkl} is the orientation-dependent elastic modulus. E_{hkl} is obtained from the uniaxial compliance measured from unloading. Elements of the compliance matrix are calculated from the elastic constants.[140,143,144] The symmetry of

Equation (1) prevents us from uniquely identifying the exact sequence and sign of the h, k and l values. However the maximum Schmidt factor is the same for every permutation.

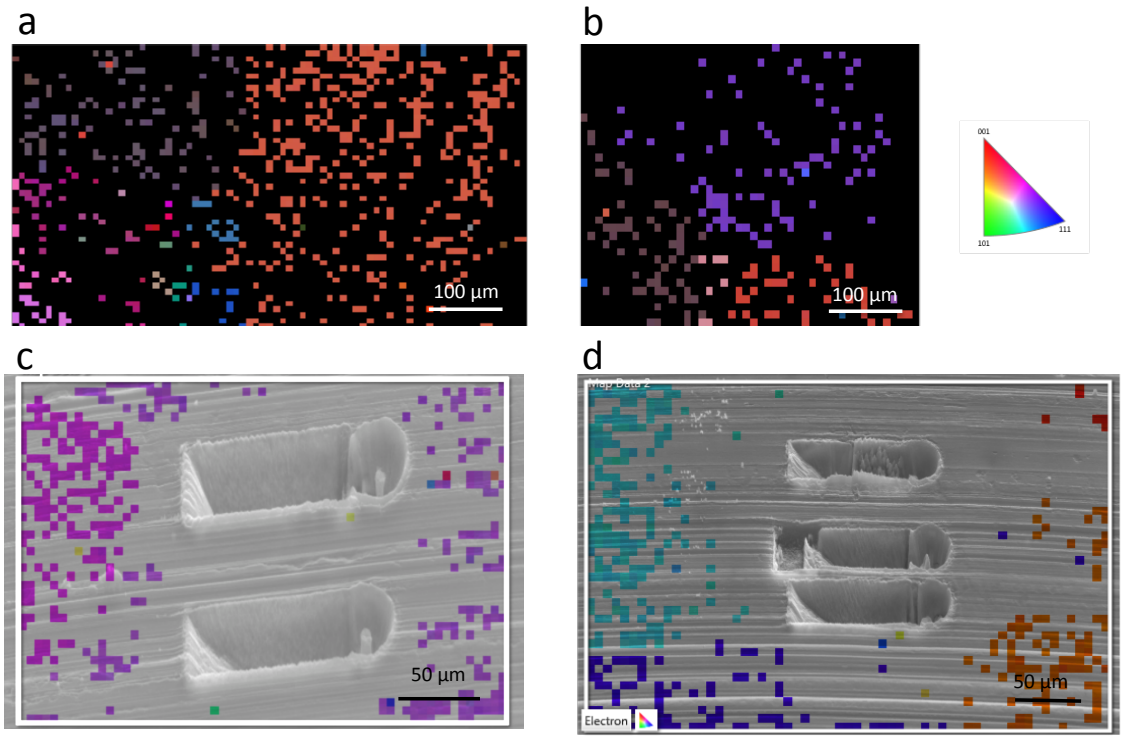

Figure 29. Crystal grain map of Li substrate with pillars post compression. (a,b) Orientation Imaging Microscopy map generated by EBSD showing the annealed and as-cut surface of the Li sample, with grain size 250±86 µm (c,d) SEM image of pillars post-compression overlaid with orientation mapping.

4.5 Results and Discussions

Figure 29. (a) shows representative engineering stress vs. engineering strain data for room temperature compression of Li micropillars with different diameters. All curves exhibit an initial elastic loading segment followed by plastic flow, ending in catastrophic failure at a strain of 2 -3 %. The initial loading slope corresponds to the stiffness of each sample; the differences in these slopes are caused by the different crystallographic orientations of the samples, as well as possible effects of slight initial misalignment during the experiments.[145] We observed a pronounced increase in the yield and flow stresses as the pillar diameter was decreased. The yield strength, defined as the stress at which the first significant strain burst occurs, increases from 15 MPa to 105 MPa as the pillar diameter decreases from 9.45 μm to 1.39 μm. Figure 29. (b, c) shows snapshots of a 1 μm pillar during compression, where the pillar sheared off via a single slip offset. Figure 29. (d, e) shows SEM images of some representative Li pillars deformed at room temperature, with characteristic sharp and localized slip traces.

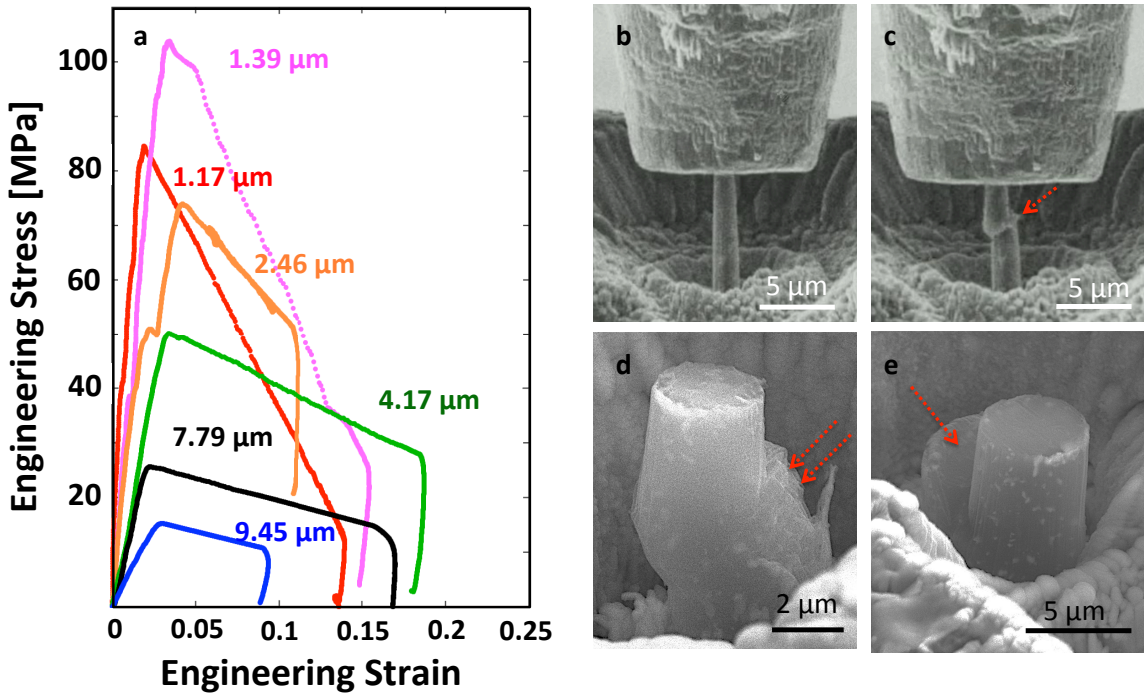

Figure 30. Room-temperature uniaxial compression experiments. (a) Engineering stress-strain data for Li pillars with different diameters. (b-c) Snapshots of *in-situ* compression of a representative 1 µm-diameter Li pillar. (d,e) Compressed 4 µm–diameter Li pillars. Arrows point to slip offsets, likely along a <111> direction.

We performed another series of micro-compression experiments at 363K. Figure 30.(a, b) shows the mechanical response of Li pillars at 363 K compared with room temperature experiments. These plots reveal that the yield strength of ~1μm-diameter samples at 363 K is around 35 MPa, compared to ~95 MPa at 298 K, and for 8.5 μm diameters, the yield strength is 5 MPa at 363 K compared to 16 MPa at 298 K. A modest decrease in yield strength during higher-temperature deformation has been reported for other bcc metals;[135,146,147] a factor of 3 decrease in yield strength of Li at only 65 K higher temperature discovered in this work has not been observed before. Tariq et al. reported the ultimate tensile strength of bulk polycrystalline Li deformed at a strain rate 2×10^{-3} s^{-1} at room temperature to be 0.89 MPa, and 0.46 MPa at 75 °C.[129] Figure 30.(c,d) shows SEM images taken during *in-situ* compression of an 8.5μm-diameter pillar and reveals that, unlike in room temperature experiments, this sample experiences barreling with no visible crystallographic slip offsets.

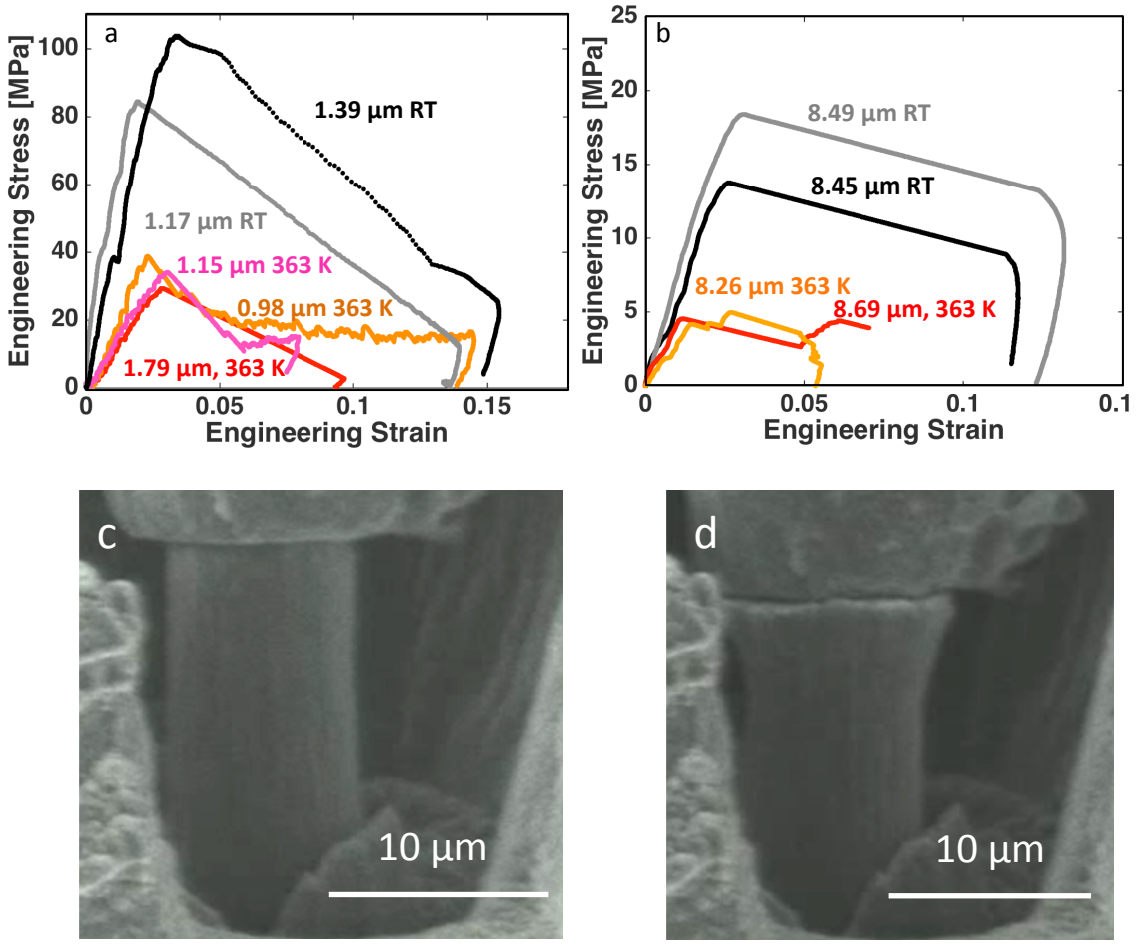

Figure 31. Uniaxial compression at 363 K. Engineering stress vs. engineering strain for compression of Li pillars with diameters of (a) ~1 um and (b) ~8 um at room temperature (RT) and 363 K. (c, d) snapshots of *in-situ* compression of a 9 µm diameter Li pillar at 363 K, which shows barreling and no crystallographic offsets.

The post-mortem localized deformation via crystallographic slip exhibited by Li at room temperature (Figure 29. (b,e)) is similar to those reported for Nb[148,149] and V[145] nanopillars

deformed at room temperature; the deformation of Mo and W nanopillars is characterized by uniform deformation with wavy slip traces[147,149,150]. A common trait shared by Nb and V is a low critical temperature (T_c), defined as the temperature at which screw and edge dislocations have similar mobility, and the effects of intrinsic lattice resistance become negligible[148,149]. A lack of closest-packed planes in bcc metals and the non-planarity of screw dislocation cores leads to their motion via cross-slip rather than glide-only and to their experiencing a higher effective Peierls' barrier compared with that of the edge dislocations. At higher temperatures, the thermally activated screw dislocations are able to move more easily through the potential energy landscape until T_c, when their mobility becomes virtually equivalent to that of edge dislocations. At that point, it becomes possible to initiate an avalanche of dislocations gliding on a single slip-plane, resulting in localized slip offsets, a common characteristic of deformation in fcc pillars[130]. T_c for Nb is 350K and that for V is 380 K, which are low enough that compression at room temperature produces fcc-like deformation[151], while Mo and W have T_c values of 480 K and 800 K, which leads to the waviness in the slip patterns during room-temperature deformation[149]. It is not surprising that Li would exhibit similar fcc-like deformation behavior as Nb and V, because while no report exists on the T_c of Li, it is likely to be lower than its melting temperature of 453 K. In our experiments at 363 K, the post-mortem images show a transition from localized to homogeneous deformation, which is likely related to the low melting point of Li and the high homologous temperature of the experiments, $T_{test}/T_{melting}$, which is 0.65 at 298 K, and 0.8 at 363 K. At high homologous temperatures the dislocation movement is no longer confined to slip

planes with the largest resolved shear stress because thermally activated processes like cross-slip and dislocation climb become possible[152]. This also explains the observed decrease in yield strength (Figure 29. (a,b)) compared with room-temperature deformation.

Figure 31. (a) shows the plot of Critical Resolved Shear Stress (CRSS) at 2% strain as a function of pillar diameter on a log-log scale. We chose the most common slip system in bcc metals - {100}<111>[153] to calculate CRSS for all experiments by multiplying the axial flow stress at 2% strain by the maximum Schmidt factor allowed for the slip system. The crystallographic orientation of each pillar was estimated either directly from EBSD map or from the unloading data when EBSD mapping was unavailable. We found the power law slope for size-dependent strengthening of Li at room temperature to be -0.68 and -1.00 at 363 K. Figure 31. (b) shows the CRSS normalized by the shear modulus, G[120], as a function of the pillar diameter, D, normalized by the Burgers vector, b[154], for Li and several other BCC metals deformed at room temperature. It shows that at room temperature, Li has the highest relative strength among all metals in this size range. Additionally, the size effect slope for Li deformed at 363 K is higher than virtually all other size effect slopes reported for single crystalline BCC metals.[130]

The large size-effect at room temperature may be explained by one of two mechanisms: a) dislocation multiplication-driven plasticity[155,156], where the entanglement of the dislocation segments contribute to increased flow stress in a manner similar to forest-hardening in bulk crystals; or b) dislocation-nucleation governed plasticity, commonly

observed in the deformation of small-scale single crystalline metals, which is accommodated by dislocation nucleation – most likely at the existing single-arm sources and/or at the surfaces – which occurs at ever higher flow stresses[151]. At 363 K, the enhancement in size effect might be caused by the increased mobility of the screw dislocations, which causes the rate of dislocation annihilation to increase and to transition overall deformation to nucleation-driven plasticity sooner. This is consistent with the size effect plot in Figure 31. (b), which shows that at room temperature, the power law slope of -0.68 for Li is close to those of V (-0.79) and Nb (-0.93)[145], the two bcc metals exhibiting fcc-like deformation and size-effect exponent. This plot also reveals that relative to the shear modulus, Li is the strongest of all reported bcc metals within the studied size range; for example at a pillar diameter of 1 μm (D/b=3300), the relative strength of Li is a factor of 1.7 higher than V and Nb, and a factor of 2.3 higher than W. At 363 K, the size-effect slope becomes -1.00, while the normalized strength decreases by a factor of ~3.5 compared to room temperature over the entire size range.

This size-effect has important implications for dendrite formation and growth that may explain why applying an external pressure higher than what is believed to be the bulk yield strength of Li at room temperature, 0.41 – 0.89 MPa[121,128], on a cell stack has not fully prevented dendrite formation[122–124]**.** Our findings demonstrate that during the initial stages of dendrite nucleation and growth, the yield strength of nanoscale dendrites exceeds that of the externally applied pressure, which is what allows them to grow. As the dendrites expand, their yield strength decreases to the point where it is balanced by the applied pressure, which drives them to deform plastically and promotes the in-plane

growth of Li[122,124], leading to a smoother surface at the top of the deposit. The high yield strength also causes an appreciable change in the kinetics of dendrite growth through the pressure term in the modified Butler-Volmer equation[120,121]. At higher temperatures, the dramatic decrease in yield strength may explain why dendrite suppression is more easily achieved[157].

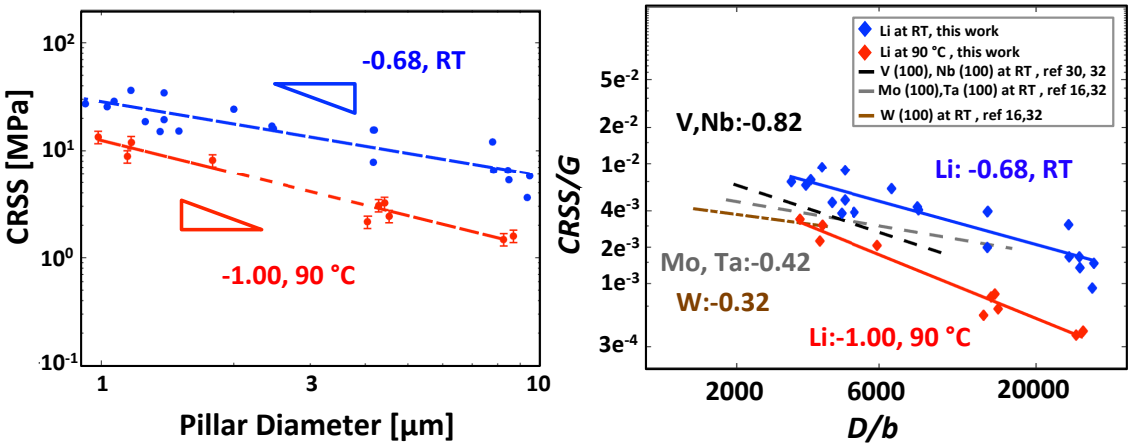

Figure 32. Size effect in Li at RT and 363K compared with other BCC metals. (a) CRSS vs. pillar diameter for room temperature (RT) and 363 K experiments. Error bars are plotted for those data points where pillars bent after catastrophic failure, causing the unloading data to no longer reflect the stiffness. In those cases, the Schmidt factor may range from 0.500 to 0.272, and the error bars represent one standard deviation. (b) CRSS normalized by the bulk shear modulus vs. pillar diameter normalized by the Burgers vector for different single crystalline bcc metals. The values for the slopes are of the CRSS vs. D, not the normalized values.

In addition to strength, the elastic properties of Li, such as the moduli, which are size-*independent,* are also expected to affect Li dendrite growth.[120] In a single crystal, the elastic properties such as the shear modulus, G, elastic modulus, E, and Poisson's ratio, ν, vary with crystallographic orientation. Li has a very high anisotropy factor of 8.52, defined as $A = \frac{2C_{44}}{C_{11} - C_{12}}$, where C_{11}, C_{21} and C_{44} are elastic constants.[143,144] For an isotropic material, A equals 1. Single crystal W is considered to be isotropic, with A_W= 1.01.[132] However most metals are anisotropic, with A values ranging between 0.5 and 4.[132] The anisotropy factor values for bcc metals Mo, Nb, Ta, and V are 0.91, 0.49, 1.56, and 0.78, respectively.[132] The high anisotropy facto of Li implies that the mechanical properties of each Li grain vary significantly with orientation, which leads to a broad range in shear and elastic moduli and different propensity for dendrite formation and growth. Experimental values of elastic constants as a function of temperature exist only in the range of 78 – 300 K.[143,144] Our collaborators used DFT to calculate the elastic constants of Li between 78 K and 440 K, using quasiharmonic approximations. Figure 33.(a) shows C_{11}, C_{12}, and C_{44}, plotted as a function of temperature along with the experimental data from Slotwinski et al. (78 – 300 K).[143] The DFT predicted trend where the elastic constants decrease linearly, reaching a finite value close to the melting point, is in agreement with experimental studies done on a variety of material such as Au, Cu, and NaCl.[158–160] The Born criterion for melting,[161] where the shear modulus C_{44} and $C_{11} - C_{12}$ vanish at melting point, is only valid for an infinite crystal under zero external stress.[162] Figure 33.(a) reveals that the predicted values agree with the experimental data in the 78 – 300 K range within ~5-10%. It is encouraging that although DFT calculations have sometimes been found to poorly predict C_{44},[163] our

DFT prediction of C_{44} for room temperature value agrees well with experimental data (1.14% difference). Using both sets of elastic constants as input, we calculated $E(hkl)$, $G(hkl)$, and the bulk modulus B, and plotted them as a function of temperature in Figure 33. (b,d). E is calculated using Eq. (4.1), and B is obtained using the relation $B = \frac{C_{11}+2C_{12}}{3}$. The calculation of $G(hkl)$ is a little more complex, and we have based ours on the work by Turley and Sines.[164] The authors gave the general expression for the shear modulus of a single crystal

$$G = \frac{1}{s_{44} + 4(s_{11} - s_{12} - \frac{1}{2}s_{44})\Omega} \tag{4.2}$$

where s_{11}, s_{12}, and s_{44} are elements of the compliance matrix, and Ω is the angle dependence as defined below

$$\Omega = a + b\sin 2\theta + c\cos 2\theta \tag{4.3}$$

where a, b and c are linear combinations of the directional cosines of (hkl). A schematic is given in Figure 32. θ is indicated in Figure 32. For a single anisotropic crystal, it is intuitive that the shear modulus $G(hkl)$ would also be dependent on the direction of the shear, as indicated by $(h'k'l')$. For our study, it is beneficial to average this angle dependent G over 360°, as the compressive forces applied by the separator would be coming form all directions. It is clear that when Eq. (4.3) is averaged over 2π with respect to θ, the sinusoidal terms disappear. The expression for a is given as

$$a = A^2B^2 + C^2D^2 \tag{4.4}$$

where

$$\begin{aligned} A &= \cos\alpha\cos\beta \\ B &= \sin\alpha\cos\beta \\ C &= \sin\beta \\ D &= \cos\beta \end{aligned} \tag{4.5}$$

and

$$\begin{aligned} \sin\alpha &= \frac{k}{(h^2+k^2)^{1/2}}; \quad \sin\beta = \frac{l}{(h^2+k^2+l^2)^{1/2}} \\ \cos\alpha &= \frac{h}{(h^2+k^2)^{1/2}}; \quad \cos\beta = \left(\frac{h^2+k^2}{h^2+k^2+l^2}\right)^{1/2} \end{aligned} \tag{4.6}$$

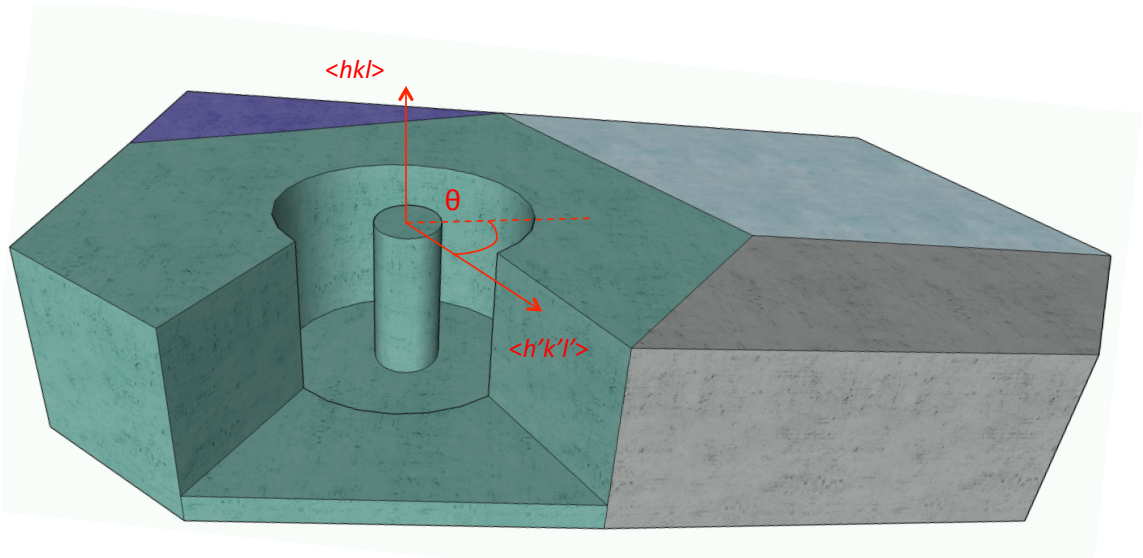

Figure 33. A single crystalline pillar situated within a crystal grain with normal in the direction of <*hkl*>. The different colored regions indicate different crystal grains imbedded in a polycrystalline Li metal foil. <*h'k'l'*> is a transverse direction in the (*hkl*) plane. Θ is the angle between <*h'k'l'*> and the Meridional tangent (indicated by the dashed line). For the definition please refer to Turley et al.[164]

The plot in Figure. 33. (b) shows an excellent agreement in *B* between DFT and those calculated using experimental elastic constants, with an average variance of 2.51% within the entire temperature range. Figure 33. (c) depicts the temperature dependence of $E_{<111>}$ (stiffest orientation) and $E_{<100>}$ (most compliant orientation) and shows that at 300 K, DFT predicts $E_{<111>}$ to be 21.1 GPa and $E_{<100>}$ to be 6.09 GPa; and calculation based on experimental elastic constants[143] reveal $E_{<111>}$ to be 21.2 GPa and $E_{<100>}$ to be 3.00 GPa. Figure 33. (d) show the temperature dependence of $G_{<100>}$ and $G_{<111>}$ and reveals that at room temperature, the DFT predicts 8.68 GPa along <100> while calculations from experimental data yield 8.78 GPa; respective values for <111> are 2.28 GPa and 1.46 GPa. An interesting observation is that in shear, the stiffest orientation is <100>, and the most compliant is <111>, which is diametrically opposite to axial loading, with the stiffest orientation being <111> and most compliant <100>. At 440 K, DFT predicts a moderate decrease of 1.49% and 0.85 % for $G_{<100>}$ and $G_{<111>}$, respectively. Unlike the yield strength, the elastic properties have a weak dependence on temperature. Figure 33. (c,d) shows that the large difference between the strongest and weakest crystal orientation persists throughout the entire studied temperature range. The large difference between the elastic properties of the strongest and weakest orientation may be the reason why there exists a high level of discrepancy in the experimental of the mechanical properties of Li. Depending on the orientation distribution of the polycrystalline sample, whether it is <100> rich or <111> rich in the direction of loading, the congregate value can be any value that falls within the range predicted in this work. The anisotropy of Li can be alternatively demonstrated in the inability of the Voigt-Reuss-Hill (VRH) approximation to correctly estimate bulk properties of Li. The VRH approximation estimates bulk elastic properties of

materials using the elastic constants.[165,166] For isotropic and weakly anisotropic materials (A<3), the VRH predicted value is usually in good agreement with experimental data, with an error of less than 3%.[167,168] However VRH predicts the bulk polycrystalline Li metal to have an elastic modulus of 10.6 GPa (experimental) or 13.1 GPa (DFT) at 298 K, compared to values of 1.9 GPa, 4.9 GPa, 7.8 GPa and 7.9 GPa as reported by literature.[126–129] Predictions for the shear modulus are 3.93 GPa (experimental) and 5 GPa (DFT), compared to 3.4 GPa, 4.2 GPa.[169,170] Therefore using a single value to describe the mechanical properties of Li, in modeling work or experimental efforts of dendrite suppression, may be too simplistic. Li metal foil are polycrystalline in nature,[171] with each crystal grain having different mechanical properties depending on its orientation. Successful dendrite suppression must take this into account. For example, our results indicate that dendrites originating from the <100>-oriented grain would require a separator with a shear modulus of at least 17.5 GPa to suppress them, while a value of 2.92 GPa is sufficient for the <111> orientation, according to the linear stability analysis by Monroe and Newman.[120]

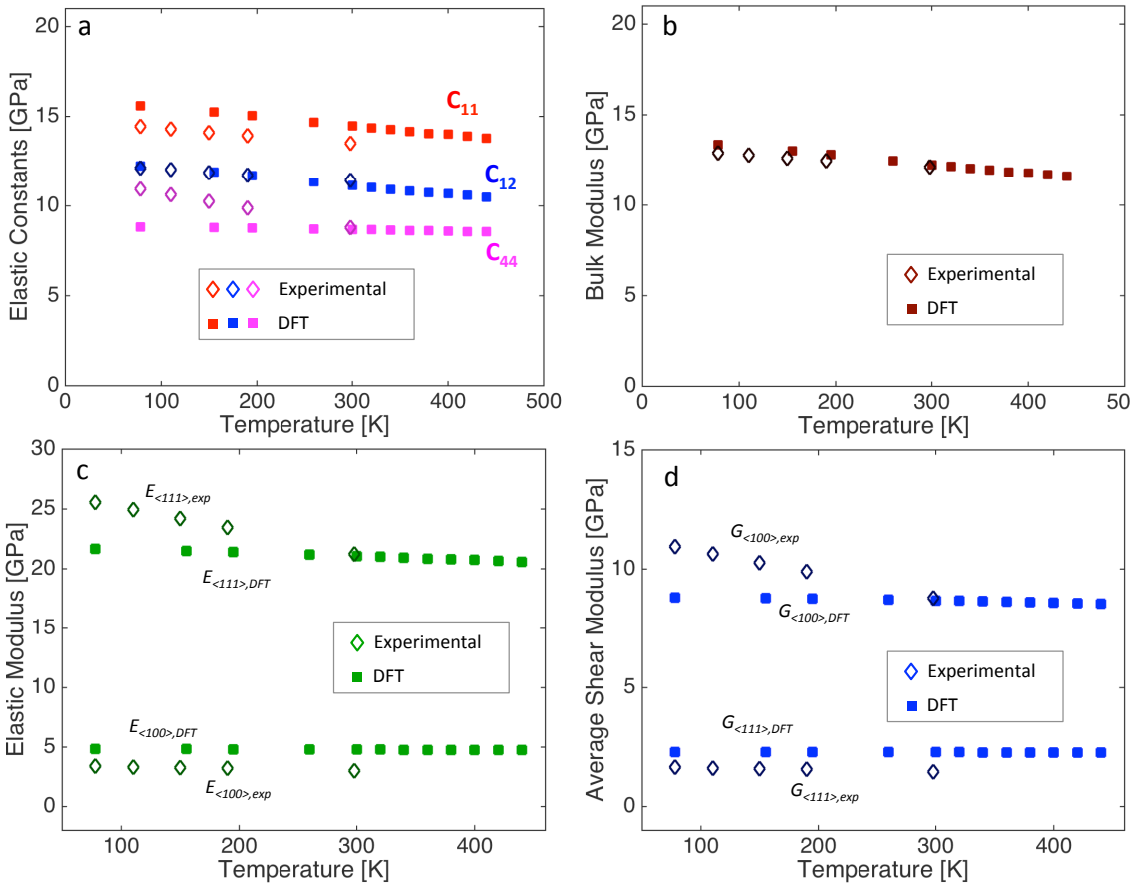

Figure 34. Elastic properties of single crystalline Li at different temperatures and in different crystallographic orientations. (a) Elastic constants C_{11}, C_{12}, C_{44} as a function of temperature. Solid squares (n) represent DFT calculations (this work), diamonds (◇) represent experimental values taken from Slotwinski et al[143]. (b) Bulk modulus versus temperature. Solid squares (n) represent DFT calculations, while diamonds (□) represent values calculated using data from Slotwinski et al.[143] (c) Maximum elastic modulus ($E_{<111>}$) and minimum elastic modulus ($E_{<100>}$) as a function of temperature as calculated by DFT and gleaned from experiments. (d) Maximum average shear modulus ($G_{<100>}$) and minimum average shear modulus ($G_{<111>}$) as a function of temperature as calculated by DFT and gleaned from experiments.

4.6 Conclusions

Our results provide insights into the mechanical properties of Li as a function of sample dimensions, temperature, and crystallographic orientation, and have significant implications for Li dendrite growth, as well as provide guidelines for their suppression. The measured yield strength of 1 micron-sized Li of 105 MPa at room temperature represents a two-orders-of-magnitude increase over what is believed to be the bulk yield strength of Li, 0.41 – 0.89 MPa[121,128]., and exposes serious shortcomings of the current mechanical methods of dendrite suppression. The observed three-fold decrease in yield strength at 363 K (operating temperature of many SPEs) is substantial compared to the marginal decrease in shear modulus, which indicates that at high temperatures, dendrite suppression via inducing plastic deformation will be much more effective than finding SPEs with higher shear moduli. The high elastic anisotropy warrants the move to beyond the simple isotropic treatment of most existing theoretical efforts. More attention needs to be paid to the variation of elastic and shear moduli in the polycrystalline anode when designing SPEs with high shear modulus or when fabricating Li anodes rich in compliant orientations. Based on our experimental data and theoretical analysis, we propose that a combination of higher temperature operation together with a Li anode whose interfacial orientation has a low shear modulus, for example <111>, in contact with a solid electrolyte with high elastic modulus will prove to be an effective route to suppress dendrite formation. The rational design principles and the high-fidelity data provided will rapidly accelerate the development of a reversible Li metal anode, paving the way for higher energy density Li-ion batteries or “beyond Li-ion” chemistries such as Li-S or Li-O_2.

Chapter 5

Summary and Outlook

In this thesis, we investigated the catalytic properties of Au, Ni, Ti, LCO, LNO, and LNCO using microlattice electrodes. When using a Au cathode and 0.5M LiTFSI/DME as the electrolyte, the discharge product after the first takes a toroidal morphology and is found to be mainly Li_2O_2, with trace amounts of carbonate and carboxylate. The discharge products are fully oxidized after the first charge. As cycling continues, the discharge product transitions to large clusters of platelets, with diameters in to 5 -10 μm range. We see increased carbonate in these structures, with an emergence of LiOH. We then set forth to investigate the catalytic properties of Ni, Ti, LCO, LNO, and LNCO using the same microlattice system. Ni and Ti are found to be poor catalysts for ORR. However Ni is shown to be an appropriate C substitute under certain operation conditions (potential < 3.8 V vs. Li in DMSO). LCO, LNO and LNCO were investigated by preparing a perovskite/Ni nanoparticle slurry, which we then cast onto a Ni microlattice. We found LCO to be the best catalyst in terms of ORR and OER, as well as the best chemical stability. LNO and LNCO induces electrolyte degradation to different extents, where cells incorporating LNO electrodes show steadily increasing discharge and charge capacity, and cells incorporating LNCO electrodes show a charge plateau at above 3.6V, and dramatic capacity fade thereafter. The reaction between discharge products and DMSO is observed, where we detect large clusters of Li_2O_2/carbonate/LiOH on the surface of a slow-discharged

electrode, as well as $DMSO_2$ in the electrolyte. At higher rate cycling, an accumulation of carbonate and carboxylate species is observed with increases cycle number.

We then investigated the nano-mechanical properties of Li metal at room and elevated temperature (90°C), across compression pillars of different diameter sizes (1-9 μm). A size effect exponent of -0.68 is observed at room temperature, and -1.00 is observed at 90°C. A transition from localized slip to homogenous barreling is observed as temperature is increased, as well as a decrease in yield strength of a factor of ~3. DFT results point to extremely large elastic anisotropy from 78 K to 440 K (T_m=453 K), where the elastic and shear modulus of the strongest and weakest orientation differ by a factor of ~4. We discussed our findings in the context of mechanical Li dendrite inhibition.

The transition away from carbon and binder based electrodes is needed to further the advancement of Li-air batteries. Recent work, along with our own studies, indicates that electron conductive nanoparticles with good oxidation resistance can act as either the cathode material itself or hosts to nonconductive catalysts. The lack of stable electrolyte solvent remains one of the major hurdles. 3D architected metamaterials, with tunable pore size and surface material, show great promise in serving as a high functioning electrode as well as a test bed for fundamental studies. On the anode side Li metal remains an elusive goal, but better understanding of the small scale and anisotropic properties of Li should pave a more directed pathway to designing solid electrolytes that effectively suppress dendrites. It also urges the modeling community to treat Li as more than just a “black box” with homogenous bulk scale mechanical properties. Additionally, fabricating Li anodes

with compliant orientations may be an alternative approach that, together with mechanically robust electrolyte or separators, enhances the cyclability of the battery cell.

Bibliography

(1) U.S. Greenhouse Gas Inventory Report: 1990-2014.

(2) Bhatt, M. D.; Geaney, H.; Nolan, M.; O'Dwyer, C. Key Scientific Challenges in Current Rechargeable Non-Aqueous Li-O2 Batteries: Experiment and Theory. *Phys. Chem. Chem. Phys.* **2014**, *16*, 12093–12130.

(3) Christensen, J.; Albertus, P.; Sanchez-Carrera, R. S.; Lohmann, T.; Kozinsky, B.; Liedtke, R.; Ahmed, J.; Kojic, A. A Critical Review of Li/Air Batteries. *J. Electrochem. Soc.* **2012**, *159*, R1.

(4) Bruce, P. G.; Freunberger, S. A. Li-O2 and Li-S Batteries with High Energy Storage. *Nat. Mater.* **2012**, *11*, 19–30.

(5) Tesla Model S https://en.wikipedia.org/wiki/Tesla_Model_S.

(6) Tarascon, J. M.; Armand, M. Issues and Challenges Facing Rechargeable Lithium Batteries. *Nature* **2001**, *414*, 359–367.

(7) Xu, W.; Wang, J.; Ding, F.; Chen, X.; Nasybulin, E.; Zhang, Y.; Zhang, J.-G. Lithium Metal Anodes for Rechargeable Batteries. *Energy Environ. Sci.* **2014**, *7*, 513–537.

(8) Abraham, K. M.; Jiang, Z. A Polymer Electrolyte-Based Rechargeable Lithium/Oxygen Battery. *J. Electrochem. Soc.* **1996**, *143*, 1.

(9) Peng, Z.; Freunberger, S.; Chen, Y.; Bruce, P. A Reversible and Higher-Rate Li-O2 Battery. *Science (80-.).* **2012**, *337*, 563–566.

(10) Ottakam Thotiyl, M. M.; Freunberger, S. a; Peng, Z.; Chen, Y.; Liu, Z.; Bruce, P. G. A Stable Cathode for the Aprotic Li-O2 Battery. *Nat. Mater.* **2013**, *12*, 1050–1056.

(11) Johnson, L.; Li, C.; Liu, Z.; Chen, Y.; Freunberger, S. A.; Ashok, P. C.; Praveen, B. B.; Dholakia, K.; Tarascon, J.-M.; Bruce, P. G. The Role of LiO2 Solubility in O2 Reduction in Aprotic Solvents and Its Consequences for Li-O2 Batteries. *Nat. Chem.* **2014**, *6*, 1091–1099.

(12) Aetukuri, N. B.; McCloskey, B. D.; García, J. M.; Krupp, L. E.; Viswanathan, V.; Luntz, A. C. Solvating Additives Drive Solution-Mediated Electrochemistry and Enhance Toroid Growth in Non-Aqueous Li–O2 Batteries. *Nat. Chem.* **2014**, *7*, 50–56.

(13) Giordani, V.; Tozier, D.; Tan, H.; Burke, C. M.; Gallant, B. M.; Uddin, J.; Greer, J. R.; McCloskey, B. D.; Chase, G. V.; Addison, D. A Molten Salt Lithium–Oxygen Battery. **2016**.

(14) MIZUNO, F.; NAKANISHI, S.; KOTANI, Y.; YOKOISHI, S.; IBA, H. Rechargeable Li-Air Batteries with Carbonate-Based Liquid Electrolytes. *Electrochemistry* **2010**, *78*, 403–405.

(15) Veith, G. M.; Dudney, N. J.; Howe, J.; Nanda, J. Spectroscopic Characterization of Solid Discharge Products in Li–Air Cells with Aprotic Carbonate Electrolytes. **2011**.

(16) Bryantsev, V. S.; Giordani, V.; Walker, W.; Blanco, M.; Zecevic, S.; Sasaki, K.; Uddin, J.; Addison, D.; Chase, G. V. Predicting Solvent Stability in Aprotic

Electrolyte Li–Air Batteries: Nucleophilic Substitution by the Superoxide Anion Radical (O2•–). **2011**.

(17) Freunberger, S.; Chen, Y.; Peng, Z.; Griffin, J. M.; Hardwick, L. J.; Bardé, F.; Novák, P.; Bruce, P. G. Reactions in the Rechargeable lithium–O2 Battery with Alkyl Carbonate Electrolytes. *J. Am. Chem. Soc.* **2011**, *133*, 8040–8047.

(18) McCloskey, B. D.; Bethune, D. S.; Shelby, R. M.; Girishkumar, G.; Luntz, A. C. Solvents' Critical Role in Nonaqueous Lithium–Oxygen Battery Electrochemistry. *J. Phys. Chem. Lett.* **2011**, *2*, 1161–1166.

(19) Freunberger, S. a; Chen, Y.; Drewett, N. E.; Hardwick, L. J.; Bardé, F.; Bruce, P. G. The Lithium-Oxygen Battery with Ether-Based Electrolytes. *Angew. Chem. Int. Ed. Engl.* **2011**, *50*, 8609–8613.

(20) Meini, S.; Tsiouvaras, N.; Schwenke, K. U.; Piana, M.; Beyer, H.; Lange, L.; Gasteiger, H. A. Rechargeability of Li-Air Cathodes Pre-Filled with Discharge Products Using an Ether-Based Electrolyte Solution: Implications for Cycle-Life of Li-Air Cells. *Phys. Chem. Chem. Phys.* **2013**, *15*, 11478–11493.

(21) Gallant, B.; Mitchell, R. Chemical and Morphological Changes of Li–O2 Battery Electrodes upon Cycling. *J. …* **2012**, *116*, 20800–20805.

(22) McCloskey, B. D.; Valery, A.; Luntz, A. C.; Gowda, S. R.; Wallraff, G. M.; Garcia, J. M.; Mori, T.; Krupp, L. E. Combining Accurate O2 and Li2O2 Assays to Separate Discharge and Charge Stability Limitations in Nonaqueous Li–O2 Batteries. *J. Phys. Chem. Lett.* **2013**, *4*, 2989–2993.

(23) Sharon, D.; Afri, M.; Noked, M.; Garsuch, A.; Frimer, A. A.; Aurbach, D. Oxidation of Dimethyl Sulfoxide Solutions by Electrochemical Reduction of Oxygen. *J. Phys. Chem. Lett.* **2013**, *4*, 3115–3119.

(24) Kwabi, D. G.; Batcho, T. P.; Amanchukwu, C. V.; Ortiz-Vitoriano, N.; Hammond, P.; Thompson, C. V.; Shao-Horn, Y. Chemical Instability of Dimethyl Sulfoxide in Lithium–Air Batteries. *J. Phys. Chem. Lett.* **2014**, *5*, 2850–2856.

(25) Laoire, C. O.; Mukerjee, S.; Abraham, K. M.; Plichta, E. J.; Hendrickson, M. A. Elucidating the Mechanism of Oxygen Reduction for Lithium-Air Battery Applications. **2009**.

(26) Bryantsev, V. S.; Uddin, J.; Giordani, V.; Walker, W.; Addison, D.; Chase, G. V. The Identification of Stable Solvents for Nonaqueous Rechargeable Li-Air Batteries. *J. Electrochem. Soc.* **2012**, *160*, A160–A171.

(27) Walker, W.; Giordani, V.; Uddin, J.; Bryantsev, V. S.; Chase, G. V.; Addison, D. A Rechargeable Li–O2 Battery Using a Lithium Nitrate/N,N-Dimethylacetamide Electrolyte. **2013**.

(28) Bryantsev, V. S.; Faglioni, F. Predicting Autoxidation Stability of Ether- and Amide-Based Electrolyte Solvents for Li-Air Batteries. *J. Phys. Chem. A* **2012**, *116*, 7128–7138.

(29) Herranz, J.; Garsuch, A.; Gasteiger, H. A. Using Rotating Ring Disc Electrode Voltammetry to Quantify the Superoxide Radical Stability of Aprotic Li–Air Battery Electrolytes. **2012**.

(30) MIZUNO, F.; NAKANISHI, S.; SHIRASAWA, A.; TAKECHI, K.; SHIGA, T.; NISHIKOORI, H.; IBA, H. Design of Non-Aqueous Liquid Electrolytes for Rechargeable Li-O2 Batteries. *Electrochemistry* **2011**, *79*, 876–881.

(31) Xu, J.-J.; Wang, Z.-L.; Xu, D.; Zhang, L.-L.; Zhang, X.-B. Tailoring Deposition and Morphology of Discharge Products towards High-Rate and Long-Life Lithium-Oxygen Batteries. *Nat. Commun.* **2013**, *4*, 2438.

(32) Lu, Y.; Kwabi, D.; Yao, K.; Harding, J. R.; Zhou, J.; Zuin, L.; Shao-Horn, Y. The Discharge Rate Capability of Rechargeable Li–O 2 Batteries. *Energy Environ. Sci.* **2011**, *4*, 2999–3007.

(33) Xiao, J.; Mei, D.; Li, X.; Xu, W.; Wang, D.; Graff, G. L.; Bennett, W. D.; Nie, Z.; Saraf, L. V; Aksay, I. A.; *et al.* Hierarchically Porous Graphene as a Lithium-Air Battery Electrode. *Nano Lett.* **2011**, *11*, 5071–5078.

(34) Martinez Crespiera, S.; Amantia, D.; Knipping, E.; Aucher, C.; Aubouy, L.; Amici, J.; Zeng, J.; Francia, C.; Bodoardo, S. Electrospun Pd-Doped Mesoporous Carbon Nano Fibres as Catalysts for Rechargeable Li–O 2 Batteries. *RSC Adv.* **2016**, *6*, 57335–57345.

(35) Lu, Y.-C.; Gasteiger, H. A.; Shao-Horn, Y. Catalytic Activity Trends of Oxygen Reduction Reaction for. *Electrochem. Solid-State Lett.* **2011**, *14*, 19048–19051.

(36) Harding, J. R.; Lu, Y.-C.; Tsukada, Y.; Shao-Horn, Y.; Lu, Y. C.; Gasteiger, H. A.; Parent, M. C.; Chiloyan, V.; Shao-Horn, Y.; Abraham, K. M.; *et al.* Evidence of Catalyzed Oxidation of Li2O2 for Rechargeable Li–air Battery Applications. *Phys. Chem. Chem. Phys.* **2012**, *14*, 10540.

(37) Oh, D.; Qi, J.; Han, B.; Zhang, G.; Carney, T. J.; Ohmura, J.; Zhang, Y.; Shao-Horn, Y.; Belcher, A. M. M13 Virus-Directed Synthesis of Nanostructured Metal Oxides for Lithium-Oxygen Batteries. *Nano Lett.* **2014**.

(38) Zhao, Y.; Xu, L.; Mai, L.; Han, C.; An, Q.; Xu, X.; Liu, X.; Zhang, Q. Hierarchical Mesoporous Perovskite La0.5Sr0.5CoO2.91 Nanowires with Ultrahigh Capacity for Li-Air Batteries. *Proc. Natl. Acad. Sci. U. S. A.* **2012**, *109*, 19569–19574.

(39) Liu, W.-M.; Gao, T.-T.; Yang, Y.; Sun, Q.; Fu, Z.-W. A Hierarchical Three-Dimensional NiCo2O4 Nanowire Array/carbon Cloth as an Air Electrode for Nonaqueous Li-Air Batteries. *Phys. Chem. Chem. Phys.* **2013**, *15*, 15806–15810.

(40) McCloskey, B. D.; Speidel, A.; Scheffler, R.; Miller, D. C.; Viswanathan, V.; Hummelshøj, J. S.; Nørskov, J. K.; Luntz, A. C. Twin Problems of Interfacial Carbonate Formation in Nonaqueous Li–O 2 Batteries. *J. Phys. Chem. Lett.* **2012**, *3*, 997–1001.

(41) Gallant, B. M.; Mitchell, R. R.; Kwabi, D. G.; Zhou, J.; Zuin, L.; Thompson, C. V.; Shao-Horn, Y. Chemical and Morphological Changes of Li–O 2 Battery Electrodes upon Cycling. *J. Phys. Chem. C* **2012**, *116*, 20800–20805.

(42) Ottakam Thotiyl, M. M.; Freunberger, S. a; Peng, Z.; Bruce, P. G. The Carbon Electrode in Nonaqueous Li-O2 Cells. *J. Am. Chem. Soc.* **2013**, *135*, 494–500.

(43) Riaz, A.; Jung, K.-N.; Chang, W.; Lee, S.-B.; Lim, T.-H.; Park, S.-J.; Song, R.-H.; Yoon, S.; Shin, K.-H.; Lee, J.-W. Carbon-Free Cobalt Oxide Cathodes with Tunable Nanoarchitectures for Rechargeable Lithium-Oxygen Batteries. *Chem. Commun. (Camb)*. **2013**, *49*, 5984–5986.

(44) Liao, K.; Zhang, T.; Wang, Y.; Li, F.; Jian, Z.; Yu, H.; Zhou, H. Nanoporous Ru as a Carbon- and Binder-Free Cathode for Li-O2 Batteries. *ChemSusChem* **2015**, *8*, 1429–1434.

(45) Lin, X.; Su, J.; Li, L.; Yu, A. Hierarchical Porous NiCo2O4@Ni as Carbon-Free Electrodes for Lithium–oxygen Batteries. *Electrochim. Acta* **2015**, *168*, 292–299.

(46) Kim, S. T.; Choi, N.-S.; Park, S.; Cho, J. Optimization of Carbon- and Binder-Free Au Nanoparticle-Coated Ni Nanowire Electrodes for Lithium-Oxygen Batteries. *Adv. Energy Mater.* **2014**, *5*, n/a – n/a.

(47) Veith, G. M.; Dudney, N. J. Current Collectors for Rechargeable Li-Air Batteries. *J. Electrochem. Soc.* **2011**, *158*, A658.

(48) Liu, X.; Wang, D.; Shi, S. Exploration on the Possibility of Ni Foam as Current

Collector in Rechargeable Lithium-Air Batteries. *Electrochim. Acta* **2013**, *87*, 865–871.

(49) Meini, S.; Piana, M.; Tsiouvaras, N.; Garsuch, A.; Gasteiger, H. A. The Effect of Water on the Discharge Capacity of a Non-Catalyzed Carbon Cathode for Li-O2 Batteries. *Electrochem. Solid-State Lett.* **2012**, *15*, A45.

(50) Cho, M. H.; Trottie, J.; Gagnon, C.; Hovington, P.; Clément, D.; Vijh, A.; Kim, C.-S.; Guerfi, A.; Black, R.; Nazar, L.; *et al.* The Effects of Moisture Contamination in the Li-O2 Battery. *J. Power Sources* **2014**.

(51) Mitchell, R. R.; Gallant, B. M.; Thompson, C. V.; Shao-Horn, Y.; Abraham, K. M.; Jiang, Z.; Lu, Y. C.; Xu, Z. C.; Gasteiger, H. A.; Chen, S.; *et al.* All-Carbon-Nanofiber Electrodes for High-Energy Rechargeable Li–O2 Batteries. *Energy Environ. Sci.* **2011**, *4*, 2952.

(52) Adams, B. D.; Radtke, C.; Black, R.; Trudeau, M. L.; Zaghib, K.; Nazar, L. F. Current Density Dependence of Peroxide Formation in the Li–O2 Battery and Its Effect on Charge. *Energy Environ. Sci.* **2013**, *6*, 1772.

(53) Mitchell, R.; Gallant, B.; Shao-horn, Y.; Thompson, C. V. Mechanisms of Morphological Evolution of Li2O2 Particles during Electrochemical Growth. *J. Phys. Chem. Lett.* **2013**, *4*, 1060–1064.

(54) Horstmann, B.; Gallant, B.; Mitchell, R.; Bessler, W. G.; Shao-Horn, Y.; Bazant, M. Z. Rate-Dependent Morphology of Li 2 O 2 Growth in Li–O 2 Batteries. *J. Phys. Chem. Lett.* **2013**, *4*, 4217–4222.

(55) Lu, J.; Cheng, L.; Lau, K. C.; Tyo, E.; Luo, X.; Wen, J.; Miller, D.; Assary, R. S.; Wang, H.-H.; Redfern, P.; *et al.* Effect of the Size-Selective Silver Clusters on Lithium Peroxide Morphology in Lithium-Oxygen Batteries. *Nat. Commun.* **2014**, *5*, 4895.

(56) Xiao, J.; Mei, D.; Li, X.; Xu, W.; Wang, D.; Graff, G. L.; Bennett, W. D.; Nie, Z.; Saraf, L. V.; Aksay, I. A.; *et al.* Hierarchically Porous Graphene as a Lithium–Air Battery Electrode. **2011**.

(57) Zakharchenko, T. K.; Kozmenkova, A. Y.; Itkis, D. M.; Goodilin, E. A. Lithium Peroxide Crystal Clusters as a Natural Growth Feature of Discharge Products in Li-O2 Cells. *Beilstein J. Nanotechnol.* **2013**, *4*, 758–762.

(58) Li, Y.; Wang, J.; Li, X.; Geng, D.; Banis, M. N.; Tang, Y.; Wang, D.; Li, R.; Sham, T.-K.; Sun, X.; *et al.* Discharge Product Morphology and Increased Charge Performance of Lithium–oxygen Batteries with Graphene Nanosheet Electrodes: The Effect of Sulphur Doping. *J. Mater. Chem.* **2012**, *22*, 20170.

(59) Viswanathan, V.; Thygesen, K. S.; Hummelshøj, J. S.; Nørskov, J. K.; Girishkumar, G.; McCloskey, B. D.; Luntz, a C. Electrical Conductivity in Li2O2 and Its Role in Determining Capacity Limitations in Non-Aqueous Li-O2 Batteries. *J. Chem. Phys.* **2011**, *135*, 214704.

(60) Westermarck, S. USE OF MERCURY POROSIMETRY AND NITROGEN ADSORPTION IN CHARACTERISATION OF THE PORE STRUCTURE OF MANNITOL AND MICROCRYSTALLINE CELLULOSE POWDERS , GRANULES, University of Helsinki, 2000.

(61) Capillary action https://en.wikipedia.org/wiki/Capillary_action.

(62) Surface-tension values https://en.wikipedia.org/wiki/Surface-tension_values.

(63) Zhao, G.; Bi, S.; Li, X.; Wu, J. Surface Tension of Diethyl Carbonate, 1,2-Dimethoxyethane and Diethyl Adipate. *Fluid Phase Equilib.* **2010**, *295*, 46–49.

(64) No Title.

(65) Nelson Weker, J.; Li, Y.; Shanmugam, R.; Lai, W.; Chueh, W. C. Tracking Non-

Uniform Mesoscale Transport in $LiFePO_4$ Agglomerates During Electrochemical Cycling. *ChemElectroChem* **2015**, *2*, 1576–1581.

(66) Li, Y.; Weker, J. N.; Gent, W. E.; Mueller, D. N.; Lim, J.; Cogswell, D. A.; Tyliszczak, T.; Chueh, W. C. Dichotomy in the Lithiation Pathway of Ellipsoidal and Platelet $LiFePO_4$ Particles Revealed through Nanoscale Operando State-of-Charge Imaging. *Adv. Funct. Mater.* **2015**, *25*, 3677–3687.

(67) Li, Y.; El Gabaly, F.; Ferguson, T. R.; Smith, R. B.; Bartelt, N. C.; Sugar, J. D.; Fenton, K. R.; Cogswell, D. A.; Kilcoyne, A. L. D.; Tyliszczak, T.; *et al.* Current-Induced Transition from Particle-by-Particle to Concurrent Intercalation in Phase-Separating Battery Electrodes. *Nat. Mater.* **2014**, *13*, 1149–1156.

(68) Chueh, W. C.; Gabaly, F. El; Sugar, J. D.; Bartelt, N. C.; McDaniel, A. H.; Fenton, K. R.; Zavadil, K. R.; Tyliszczak, T.; Lai, W.; McCarty, K. F. Intercalation Pathway in Many-Particle LiFePO4 Electrode Revealed by Nanoscale State-of-Charge Mapping. **2013**.

(69) Padhi, A. K.; Nanjundaswamy, K. S.; Goodenough, J. B. Phospho-Olivines as Positive-Electrode Materials for Rechargeable Lithium Batteries. *J. Electrochem. Soc.* **1997**, *144*, 1188–1194.

(70) Delmas, C.; Maccario, M.; Croguennec, L.; Le Cras, F.; Weill, F. Lithium Deintercalation in LiFePO4 Nanoparticles via a Domino-Cascade Model. *Nat. Mater.* **2008**, *7*, 665–671.

(71) Xiao, J.; Wang, D.; Xu, W.; Wang, D.; Williford, R. E.; Liu, J.; Zhang, J.-G. Optimization of Air Electrode for Li/Air Batteries. *J. Electrochem. Soc.* **2010**, *157*, A487.

(72) Montemayor, L. C.; Meza, L. R.; Greer, J. R. Design and Fabrication of Hollow Rigid Nanolattices via Two-Photon Lithography. *Adv. Eng. Mater.* **2014**, *16*, 184–

189.

(73) Meza, L. R.; Das, S.; Greer, J. R. Strong, Lightweight, and Recoverable Three-Dimensional Ceramic Nanolattices. *Science (80-.).* **2014**, *345*, 1322–1326.

(74) Wendy Gu, X.; Greer, J. R. Ultra-Strong Architected Cu Meso-Lattices. *Extrem. Mech. Lett.* **2015**, *2*, 7–14.

(75) Schaedler, T. A.; Jacobsen, A. J.; Torrents, A.; Sorensen, A. E.; Lian, J.; Greer, J. R.; Valdevit, L.; Carter, W. B. Ultralight Metallic Microlattices. *Science* **2011**, *334*, 962–965.

(76) Rys, J.; Valdevit, L.; Schaedler, T. a.; Jacobsen, A. J.; Carter, W. B.; Greer, J. R. Fabrication and Deformation of Metallic Glass Micro-Lattices. *Adv. Eng. Mater.* **2014**, *16*, 889–896.

(77) Maloney, K. J.; Roper, C. S.; Jacobsen, A. J.; Carter, W. B.; Valdevit, L.; Schaedler, T. A. Microlattices as Architected Thin Films: Analysis of Mechanical Properties and High Strain Elastic Recovery. *APL Mater.* **2013**, *1*, 022106.

(78) Sarapuu, A.; Nurmik, M.; Mändar, H.; Rosental, A.; Laaksonen, T.; Kontturi, K.; Schiffrin, D. J.; Tammeveski, K. Electrochemical Reduction of Oxygen on Nanostructured Gold Electrodes. *J. Electroanal. Chem.* **2008**, *612*, 78–86.

(79) Burckel, D. B.; Washburn, C. M.; Raub, A. K.; Brueck, S. R. J.; Wheeler, D. R.; Brozik, S. M.; Polsky, R. Lithographically Defined Porous Carbon Electrodes. *Small* **2009**, *5*, 2792–2796.

(80) Gallant, B. M.; Mitchell, R. R.; Kwabi, D. G.; Zhou, J.; Zuin, L.; Thompson, C. V.; Shao-Horn, Y. Chemical and Morphological Changes of Li–O2 Battery Electrodes upon Cycling. **2012**.

(81) Gallant, B. M.; Kwabi, D. G.; Mitchell, R. R.; Zhou, J.; Thompson, C. V.; Shao-

Horn, Y. Influence of Li2O2 Morphology on Oxygen Reduction and Evolution Kinetics in Li–O2 Batteries. *Energy Environ. Sci.* **2013**, *6*, 2518.

(82) Meini, S.; Piana, M.; Beyer, H.; Schwammlein, J.; Gasteiger, H. A. Effect of Carbon Surface Area on First Discharge Capacity of Li-O2 Cathodes and Cycle-Life Behavior in Ether-Based Electrolytes. *J. Electrochem. Soc.* **2012**, *159*, A2135–A2142.

(83) Schwenke, K. U.; Meini, S.; Wu, X.; Gasteiger, H. A.; Piana, M. Stability of Superoxide Radicals in Glyme Solvents for Non-Aqueous Li-O2 Battery Electrolytes. *Phys. Chem. Chem. Phys.* **2013**, *15*, 11830–11839.

(84) Nakamoto, K. *Infrared and Raman Spectra of Inorganic and Coordination Compounds: Part B: Applications in Coordination, Organometallic, and Bioinorganic Chemistry*; 2008.

(85) Siebert, F.; Hildebrandt, P. *Vibrational Spectroscopy in Life Science*; Wiley-VCH Verlag GmbH & Co. KGaA: Weinheim, 2008.

(86) Thapa, A. K.; Shin, T. H.; Ida, S.; Sumanasekera, G. U.; Sunkara, M. K.; Ishihara, T. Gold–Palladium Nanoparticles Supported by Mesoporous β-MnO2 Air Electrode for Rechargeable Li-Air Battery. *J. Power Sources* **2012**, *220*, 211–216.

(87) Lu, Y.-C.; Gallant, B. M.; Kwabi, D. G.; Harding, J. R.; Mitchell, R. R.; Whittingham, M. S.; Shao-Horn, Y. Lithium–oxygen Batteries: Bridging Mechanistic Understanding and Battery Performance. *Energy Environ. Sci.* **2013**, *6*, 750.

(88) Peng, Z.; Freunberger, S. A.; Hardwick, L. J.; Chen, Y.; Giordani, V.; Bardé, F.; Novák, P.; Graham, D.; Tarascon, J.-M.; Bruce, P. G. Oxygen Reactions in a Non-Aqueous Li+ Electrolyte. *Angew. Chem. Int. Ed. Engl.* **2011**, *50*, 6351–6355.

(89) Veith, G. M.; Nanda, J.; Delmau, L. H.; Dudney, N. J. Influence of Lithium Salts on the Discharge Chemistry of Li–Air Cells. *J. Phys. Chem. Lett.* **2012**, *3*, 1242–1247.

(90) Xie, J.; Yao, X.; Madden, I. P.; Jiang, D.-E.; Chou, L.-Y.; Tsung, C.-K.; Wang, D. Selective Deposition of Ru Nanoparticles on TiSi2 Nanonet and Its Utilization for Li2O2 Formation and Decomposition. *J. Am. Chem. Soc.* **2014**, *136*, 8903–8906.

(91) Zhai, D.; Wang, H.-H.; Yang, J.; Lau, K. C.; Li, K.; Amine, K.; Curtiss, L. a. Disproportionation in Li-O2 Batteries Based on a Large Surface Area Carbon Cathode. *J. Am. Chem. Soc.* **2013**, *135*, 15364–15372.

(92) Eysel, H. H.; Thym, S. RAMAN Spectra of Peroxides. *Zeitschrift fur Anorg. und Allg. Chemie* **1975**, *411*, 97–102.

(93) Song, K.; Jung, J.; Heo, Y.-U.; Lee, Y. C.; Cho, K.; Kang, Y.-M. α-MnO2 Nanowire Catalysts with Ultra-High Capacity and Extremely Low Overpotential in Lithium-Air Batteries through Tailored Surface Arrangement. *Phys. Chem. Chem. Phys.* **2013**, *15*, 20075–20079.

(94) Liu, W.-M.; Gao, T.-T.; Yang, Y.; Sun, Q.; Fu, Z.-W.; Lu, Y. C.; Gallant, B. M.; Kwabi, D. G.; Harding, J. R.; Mitchell, R. R.; *et al.* A Hierarchical Three-Dimensional NiCo2O4 Nanowire Array/carbon Cloth as an Air Electrode for Nonaqueous Li–air Batteries. *Phys. Chem. Chem. Phys.* **2013**, *15*, 15806.

(95) Zhou, W.; Sunarso, J. Enhancing Bi-Functional Electrocatalytic Activity of Perovskite by Temperature Shock: A Case Study of LaNiO3-Sigma. *J. Phys. Chem. Lett.* **2013**, *4*, 2982–2988.

(96) Mahato, N.; Banerjee, A.; Gupta, A.; Omar, S.; Balani, K. Progress in Material Selection for Solid Oxide Fuel Cell Technology: A Review. *Progress in Materials Science*, 2015, *72*, 141–337.

(97) Jiang, S.; Zhou, W.; Niu, Y.; Zhu, Z.; Shao, Z. Phase Transition of a Cobalt-Free Perovskite as a High-Performance Cathode for Intermediate-Temperature Solid Oxide Fuel Cells. *ChemSusChem* **2012**, *5*, 2023–2031.

(98) Zhou, W.; Sunarso, J.; Motuzas, J.; Liang, F.; Chen, Z.; Ge, L.; Liu, S.; Julbe, A.; Zhu, Z. Deactivation and Regeneration of Oxygen Reduction Reactivity on Double Perovskite Ba2Bi0.1Sc0.2Co1.7O6−x Cathode for Intermediate-Temperature Solid Oxide Fuel Cells. **2011**.

(99) Ju, Y.-W.; Yoo, S.; Guo, L.; Kim, C.; Inoishi, A.; Jeong, H.; Shin, J.; Ishihara, T.; Yim, S.-D.; Kim, G. Honeycomb-Like Perovskite Oxide Electrocatalyst for a Hybrid Li-Air Battery. *J. Electrochem. Soc.* **2015**, *162*, A2651–A2655.

(100) Suntivich, J.; May, K. J.; Gasteiger, H. A.; Goodenough, J. B.; Shao-Horn, Y.; Gray, H. B.; Lewis, N. S.; Nocera, D. G.; Kanan, M. W.; Nocera, D. G.; *et al.* A Perovskite Oxide Optimized for Oxygen Evolution Catalysis from Molecular Orbital Principles. *Science* **2011**, *334*, 1383–1385.

(101) Sun, N.; Liu, H.; Yu, Z.; Zheng, Z.; Shao, C. Mn-Doped La0.6Sr0.4CoO3 Perovskite Catalysts with Enhanced Performances for Non-Aqueous Electrolyte Li-O2 Batteries. *RSC Adv.* **2016**, *6*, 13522–13530.

(102) Wei, Z.; Zhao, T.; Zhu, X.; An, L.; Tan, P. Integrated Porous Cathode Made of Pure Perovskite Lanthanum Nickel Oxide for Nonaqueous Lithium-Oxygen Batteries. *Energy Technol.* **2015**, *3*, 1093–1100.

(103) Ma, Z.; Yuan, X.; Li, L.; Ma, Z.-F. Double Perovskite Oxide Sr2CrMoO6-δ as an Efficient Electrocatalyst for Rechargeable Lithium Air Batteries. *Chem. Commun.* **2014**, *00*, 1–3.

(104) Fu, Z.; Lin, X.; Huang, T.; Yu, A. Nano-Sized La 0.8Sr 0.2MnO 3 as Oxygen Reduction Catalyst in Nonaqueous Li/O 2 Batteries. *J. Solid State Electrochem.*

2012, *16*, 1447–1452.

(105) Geaney, H.; O'Dwyer, C. Examining the Role of Electrolyte and Binders in Determining Discharge Product Morphology and Cycling Performance of Carbon Cathodes in Li-O 2 Batteries. *J. Electrochem. Soc.* **2015**, *163*, A43–A49.

(106) Lopez, K.; Park, G.; Sun, H.-J.; An, J.-C.; Eom, S.; Shim, J. Electrochemical Characterizations of LaMO3 (M = Co, Mn, Fe, and Ni) and Partially Substituted LaNi X M1−x O3 (X = 0.25 or 0.5) for Oxygen Reduction and Evolution in Alkaline Solution. *J. Appl. Electrochem.* **2015**, *45*, 313–323.

(107) Nickel Electroplating.

(108) Xu, C.; Gallant, B. M.; Wunderlich, P. U.; Lohmann, T.; Greer, J. R. Three-Dimensional Au Microlattices as Positive Electrodes for Li-O<inf>2</inf> Batteries. *ACS Nano* **2015**, *9*, 5876–5883.

(109) Le, H. T. T.; Ngo, D. T.; Ho, V.-C.; Cao, G.; Park, C.-J. Insights into Degradation of Metallic Lithium Electrode Protected by Bilayer Solid Electrolyte Based on Aluminium Substituted Lithium Lanthanum Titanate in Lithium-Air Batteries. *J. Mater. Chem. A* **2016**.

(110) Han, X.; Hu, Y.; Yang, J.; Cheng, F.; Chen, J. Porous Perovskite CaMnO3 as an Electrocatalyst for Rechargeable Li-O2 Batteries. *Chem. Commun. (Camb).* **2014**, *50*, 1497–1479.

(111) Riaz, A.; Jung, K.-N.; Chang, W.; Shin, K.-H.; Lee, J.-W. Carbon-, Binder-, and Precious Metal-Free Cathodes for Non-Aqueous Lithium-Oxygen Batteries: Nanoflake-Decorated Nanoneedle Oxide Arrays. *ACS Appl. Mater. Interfaces* **2014**, *6*, 17815–17822.

(112) Cui, Y.; Wen, Z.; Liu, Y. A Free-Standing-Type Design for Cathodes of

Rechargeable Li–O2 Batteries. *Energy Environ. Sci.* **2011**, *4*, 4727.

(113) Wang, Z.-L.; Xu, D.; Xu, J.-J.; Zhang, L.-L.; Zhang, X.-B. Graphene Oxide Gel-Derived, Free-Standing, Hierarchically Porous Carbon for High-Capacity and High-Rate Rechargeable Li-O2 Batteries. *Adv. Funct. Mater.* **2012**, *22*, 3699–3705.

(114) Koo, B. S.; Lee, J. K.; Yoon, W. Y. Improved Electrochemical Performances of Lithium–oxygen Batteries with Tungsten Carbide-Coated Cathode. *Jpn. J. Appl. Phys.* **2015**, *54*, 047101.

(115) Wang, G.; Huang, L.; Huang, W.; Xie, J.; Du, G.; Zhang, S.; Zhu, P.; Cao, G.; Zhao, X. Nanostructured Porous RuO2/MnO2 as a Highly Efficient Catalyst for High-Rate Li-O2 Batteries. *Nanoscale* **2015**, *7*, 20614–20624.

(116) Burke, C. M.; Pande, V.; Khetan, A.; Viswanathan, V.; McCloskey, B. D. Enhancing Electrochemical Intermediate Solvation through Electrolyte Anion Selection to Increase Nonaqueous Li-O2 Battery Capacity. *Proc. Natl. Acad. Sci. U. S. A.* **2015**, *112*, 9293–9298.

(117) Sharon, D.; Hirsberg, D.; Afri, M.; Chesneau, F.; Lavi, R.; Frimer, A. A.; Sun, Y.-K.; Aurbach, D. Catalytic Behavior of Lithium Nitrate in Li-O 2 Cells. *ACS Appl. Mater. Interfaces* **2015**, *7*, 16590–16600.

(118) Mozhzhukhina, N.; Méndez De Leo, L. P.; Calvo, E. J. Infrared Spectroscopy Studies on Stability of Dimethyl Sulfoxide for Application in a Li–Air Battery. *J. Phys. Chem. C* **2013**, *117*, 18375–18380.

(119) Givan, A.; Grothe, H.; Loewenschuss, A.; Nielsen, C. J. Infrared Spectra and Ab Initio Calculations of Matrix Isolated Dimethyl Sulfone and Its Water Complex. *Phys. Chem. Chem. Phys.* **2002**, *4*, 255–263.

(120) Monroe, C.; Newman, J. The Impact of Elastic Deformation on Deposition Kinetics

at Lithium/Polymer Interfaces. *J. Electrochem. Soc.* **2005**, *152*, A396.

(121) Ferrese, A.; Newman, J. Mechanical Deformation of a Lithium-Metal Anode Due to a Very Stiff Separator. *J. Electrochem. Soc.* **2014**, *161*, A1350–A1359.

(122) Wilkinson, D. P.; Blom, H.; Brandt, K.; Wainwright, D. Effects of Physical Constraints on Li Cyclability. *J. Power Sources* **1991**, *36*, 517–527.

(123) Hirai, T. Influence of Electrolyte on Lithium Cycling Efficiency with Pressurized Electrode Stack. *J. Electrochem. Soc.* **1994**, *141*, 611.

(124) Gireaud, L.; Grugeon, S.; Laruelle, S.; Yrieix, B.; Tarascon, J.-M. Lithium Metal Stripping/plating Mechanisms Studies: A Metallurgical Approach. *Electrochem. commun.* **2006**, *8*, 1639–1649.

(125) Ren, Y.; Shen, Y.; Lin, Y.; Nan, C.-W. Direct Observation of Lithium Dendrites inside Garnet-Type Lithium-Ion Solid Electrolyte. *Electrochem. commun.* **2015**, *57*, 27–30.

(126) Bridgman, P. . W. . The Effect of Tension on the Electrical Resistance of Certain Abnormal Metals. *Proc. Am. Acad. Arts Sci.* **1922**, *57*, 41–66.

(127) Robertson, W.; Montgomery, D. Elastic Modulus of Isotopically-Concentrated Lithium. *Phys. Rev.* **1960**, *117*, 440–442.

(128) Schultz, R. P. *Lithium: Measurement of Young's Modulus and Yield Strength*; 2002.

(129) Tariq, S.; Ammigan, K.; Hurh, P.; Schultz, R.; Liu, P.; Shang, J. Li Material Testing- Fermilab Antiproton Source Litihum Collection Lens. In *Proceedings of the 2003 Bipolar/BiCMOS Circuits and Technology Meeting (IEEE Cat. No.03CH37440)*; IEEE, 2003; Vol. 3, pp. 1452–1454.

(130) Greer, J. R.; De Hosson, J. T. M. Plasticity in Small-Sized Metallic Systems:

Intrinsic versus Extrinsic Size Effect. *Prog. Mater. Sci.* **2011**, *56*, 654–724.

(131) Liu, X. H.; Zhong, L.; Zhang, L. Q.; Kushima, A.; Mao, S. X.; Li, J.; Ye, Z. Z.; Sullivan, J. P.; Huang, J. Y. Lithium Fiber Growth on the Anode in a Nanowire Lithium Ion Battery during Charging. *Appl. Phys. Lett.* **2011**, *98*, 183107.

(132) Simmons, G.; Wang, H. *Single Crystal Elastic Constants and Calculated Aggregate Properties a Handbook*; The MIT Press, 1971.

(133) Vacushut.

(134) Greer, J. R.; Oliver, W. C.; Nix, W. D. Size Dependence of Mechanical Properties of Gold at the Micron Scale in the Absence of Strain Gradients. *Acta Mater.* **2005**, *53*, 1821–1830.

(135) Lee, S.-W.; Cheng, Y.; Ryu, I.; Greer, J. R. Cold-Temperature Deformation of Nano-Sized Tungsten and Niobium as Revealed by in-Situ Nano-Mechanical Experiments. *Sci. China Technol. Sci.* **2014**, *57*, 652–662.

(136) Inaba, S.; Fujino, S.; Morinaga, K. Young's Modulus and Compositional Parameters of Oxide Glasses. *J. Am. Ceram. Soc.* **1999**, *82*, 3501–3507.

(137) Khan, A.; Philip, J.; Hess, P. Young's Modulus of Silicon Nitride Used in Scanning Force Microscope Cantilevers. *J. Appl. Phys.* **2004**, *95*, 1667–1672.

(138) Chen, H. Y.; Tsai, C. J.; Lu, F. H. The Young's Modulus of Chromium Nitride Films. *Surf. Coatings Technol.* **2004**, *184*, 69–73.

(139) Greer, J. R.; Nix, W. D. Nanoscale Gold Pillars Strengthened through Dislocation Starvation. *Phys. Rev. B* **2006**, *73*, 245410.

(140) C. Nash, H.; Smith, C. S. Single-Crystal Elastic Constants of Lithium. *J. Phys. Chem. Solids* **1959**, *9*, 113–118.

(141) Aitken, Z. H.; Fan, H.; El-Awady, J. A.; Greer, J. R. The Effect of Size, Orientation and Alloying on the Deformation of AZ31 Nanopillars. *J. Mech. Phys. Solids* **2015**, *76*, 208–223.

(142) Bower, A. F. *Applied Mechanics of Solids*; CRC Press, 2009.

(143) Slotwinski, T.; Trivisonno, J. Temperature Dependence of the Elastic Constants of Single Crystal Lithium. *J. Phys. Chem. Solids* **1969**, *30*, 1276–1278.

(144) Trivisonno, J.; Smith, C. S. Elastic Constants of Lithium-Magnesium Alloys. *Acta Metall.* **1961**, *9*, 1064–1071.

(145) Han, S. M.; Bozorg-Grayeli, T.; Groves, J. R.; Nix, W. D. Size Effects on Strength and Plasticity of Vanadium Nanopillars. *Scr. Mater.* **2010**, *63*, 1153–1156.

(146) Schneider, A. S.; Frick, C. P.; Arzt, E.; Clegg, W. J.; Korte, S. Influence of Test Temperature on the Size Effect in Molybdenum Small-Scale Compression Pillars. *Philos. Mag. Lett.* **2013**, *93*, 331–338.

(147) Torrents Abad, O.; Wheeler, J. M.; Michler, J.; Schneider, A. S.; Arzt, E. Temperature-Dependent Size Effects on the Strength of Ta and W Micropillars. *Acta Mater.* **2016**, *103*, 483–494.

(148) Kim, J.-Y.; Jang, D.; Greer, J. R. Tensile and Compressive Behavior of Tungsten, Molybdenum, Tantalum and Niobium at the Nanoscale. *Acta Mater.* **2010**, *58*, 2355–2363.

(149) Schneider, A. S.; Kaufmann, D.; Clark, B. G.; Frick, C. P.; Gruber, P. A.; Mönig, R.; Kraft, O.; Arzt, E. Correlation between Critical Temperature and Strength of Small-Scale Bcc Pillars. *Phys. Rev. Lett.* **2009**, *103*, 105501.

(150) Kim, J.-Y.; Jang, D.; Greer, J. R. Crystallographic Orientation and Size Dependence of Tension–compression Asymmetry in Molybdenum Nano-Pillars. *Int. J. Plast.*

2012, *28*, 46–52.

(151) Min Han, S.; Feng, G.; Young Jung, J.; Joon Jung, H.; Groves, J. R.; Nix, W. D.; Cui, Y. Critical-temperature/Peierls-Stress Dependent Size Effects in Body Centered Cubic Nanopillars. *Appl. Phys. Lett.* **2013**, *102*, 041910.

(152) Lee, G.; Kim, J.-Y.; Burek, M. J.; Greer, J. R.; Tsui, T. Y. Plastic Deformation of Indium Nanostructures. *Mater. Sci. Eng. A* **2011**, *528*, 6112–6120.

(153) Weinberger, C. R.; Boyce, B. L.; Battaile, C. C. Slip Planes in Bcc Transition Metals. *Int. Mater. Rev.* **2013**, *58*, 296–314.

(154) Kellington, S. H.; Loveridge, D.; Titman, J. M.; L, H. F. H. and A. B.; A, K. G. and M.; K, N. S.; H, T. J. M. and K. S.; H, V. The Lattice Parameters of Some Alloys of Lithium. *J. Phys. D. Appl. Phys.* **1969**, *2*, 415.

(155) Greer, J. R.; Weinberger, C. R.; Cai, W. Comparing the Strength of F.c.c. and B.c.c. Sub-Micrometer Pillars: Compression Experiments and Dislocation Dynamics Simulations. *Mater. Sci. Eng. A* **2008**, *493*, 21–25.

(156) Weinberger, C. R.; Cai, W. Surface-Controlled Dislocation Multiplication in Metal Micropillars. *Proc. Natl. Acad. Sci. U. S. A.* **2008**, *105*, 14304–14307.

(157) Khurana, R.; Schaefer, J. L.; Archer, L. A.; Coates, G. W. Suppression of Lithium Dendrite Growth Using Cross-Linked Polyethylene/poly(ethylene Oxide) Electrolytes: A New Approach for Practical Lithium-Metal Polymer Batteries. *J. Am. Chem. Soc.* **2014**, *136*, 7395–7402.

(158) Collard, S. M.; McLellan, R. B. High-Temperature Elastic Constants of Gold Single-Crystals. *Acta Metall. Mater.* **1991**, *39*, 3143–3151.

(159) Larose, A.; Brockhouse, B. N. Lattice Vibrations in Copper at Elevated Temperatures Studied by Neutron Scattering. *Can. J. Phys.* **1976**, *54*, 1990–2009.

(160) Hunter, L.; Siegel, S. The Variation with Temperature of the Principal Elastic Moduli of NaCl near the Melting Point. *Phys. Rev.* **1942**, *61*, 84–90.

(161) Born, M. Thermodynamics of Crystals and Melting. *J. Chem. Phys.* **1939**, *7*, 591.

(162) Wang, J.; Li, J.; Yip, S.; Wolf, D.; Phillpot, S. Unifying Two Criteria of Born: Elastic Instability and Melting of Homogeneous Crystals. *Phys. A Stat. Mech. its Appl.* **1997**, *240*, 396–403.

(163) Weinberger, C. R.; Tucker, G. J.; Foiles, S. M. Peierls Potential of Screw Dislocations in Bcc Transition Metals: Predictions from Density Functional Theory. *Phys. Rev. B* **2013**, *87*, 054114.

(164) Turley, J.; Sines, G. The Anisotropy of Young's Modulus, Shear Modulus and Poisson's Ratio in Cubic Materials. *J. Phys. D. Appl. Phys.* **1971**, *4*, 264.

(165) Hill, R. The Elastic Behaviour of a Crystalline Aggregate. *Proc. Phys. Soc. Sect. A* **1952**, *65*, 349–354.

(166) Hearmon, R. F. S. The Elastic Constants of Anisotropic Materials. *Rev. Mod. Phys.* **1946**, *18*, 409–440.

(167) Chung, D. H. The Voigt-Reuss-Hill Approximation and Elastic Moduli of Polycrystalline MgO, CaF2, β-ZnS, ZnSe, and CdTe. *J. Appl. Phys.* **1967**, *38*, 2535.

(168) Uesugi, T.; Takigawa, Y.; Higashi, K. Elastic Constants of AlLi from First Principles. *Mater. Trans.* **2005**, *46*, 1117–1121.

(169) G.Samsonov. *Handbook of the Physicochemical Properties of the Elements*; Samsonov, G. V., Ed.; Springer US: Boston, MA, 1968.

(170) ElementData—Wolfram http://reference.wolfram.com/language/ref/ElementData.html.

(171) MTI. http://www.mtixtl.com/Li-Foil-30000mmL-35mmW-0.17mmTh.aspx.